Modulation of Contact Resonance Frequency in Friction Force Microscopy on the Atomic Scale

Inauguraldissertation

zur
Erlangung der Würde eines Doktors der Philosophie
vorgelegt der
Philosophisch-Naturwissenschaftlichen Fakultät
der Universität Basel

von

Pascal Steiner

aus Schötz, LU

Basel, 2011

Genehmigt von der Philosophisch-Naturwissenschaftlichen Fakultät

auf Antrag von:

Prof. Dr. Ernst Meyer, Prof. Dr. Stefan Goedecker

Basel, den 14. Dezember 2010

Prof. Dr. Martin Spiess
Dekan

creative commons

Namensnennung-Keine kommerzielle Nutzung-Keine Bearbeitung 2.5 Schweiz

---

Sie dürfen:

das Werk vervielfältigen, verbreiten und öffentlich zugänglich machen

Zu den folgenden Bedingungen:

Namensnennung. Sie müssen den Namen des Autors/Rechteinhabers in der von ihm festgelegten Weise nennen (wodurch aber nicht der Eindruck entstehen darf, Sie oder die Nutzung des Werkes durch Sie würden entlohnt).

Keine kommerzielle Nutzung. Dieses Werk darf nicht für kommerzielle Zwecke verwendet werden.

Keine Bearbeitung. Dieses Werk darf nicht bearbeitet oder in anderer Weise verändert werden.

- Im Falle einer Verbreitung müssen Sie anderen die Lizenzbedingungen, unter welche dieses Werk fällt, mitteilen. Am Einfachsten ist es, einen Link auf diese Seite einzubinden.

- Jede der vorgenannten Bedingungen kann aufgehoben werden, sofern Sie die Einwilligung des Rechteinhabers dazu erhalten.
- Diese Lizenz lässt die Urheberpersönlichkeitsrechte unberührt.

Die gesetzlichen Schranken des Urheberrechts bleiben hiervon unberührt.

Die Commons Deed ist eine Zusammenfassung des Lizenzvertrags in allgemeinverständlicher Sprache: http://creativecommons.org/licenses/by-nc-nd/2.5/ch/legalcode.de

Haftungsausschluss:
Die Commons Deed ist kein Lizenzvertrag. Sie ist lediglich ein Referenztext, der den zugrundeliegenden Lizenzvertrag übersichtlich und in allgemeinverständlicher Sprache wiedergibt. Die Deed selbst entfaltet keine juristische Wirkung und erscheint im eigentlichen Lizenzvertrag nicht. Creative Commons ist keine Rechtsanwaltsgesellschaft und leistet keine Rechtsberatung. Die Weitergabe und Verlinkung des Commons Deeds führt zu keinem Mandatsverhältnis.

Quelle: http://creativecommons.org/licenses/by-nc-nd/2.5/ch/ Datum: 3.4.2009

Dedicated to my mother, Esther

Contents

List of Figures

List of Abbreviations

AFM	Atomic Force Microscopy
AES	Auger Electron Spectroscopy
A.U.	Arbitrary Units
CR-AFM	Contact Resonance Atomic Force Microscopy
Cu	Copper
Eq.	Equation
FFM	Friction Force Microscopy
Fig.	Figure
HOPG	Higly Oriented Pyrolytic Graphite
KBr	Potassium Bromide
LFM	Lateral Force Microscopy
LM	Light Microscopy
LEED	Low-Energy Electron Diffraction
MEMS	Micro-Electro-Mechanical System
ML	Monolayer
NaCl	Sodium Chloride
NC-AFM	Non-Contact Atomic Force Microscopy
NEMS	Nano-Eletro-Mechanical System

PLL	Phase Locked Loop
SEM	Scanning Electron Microscopy
SPM	Scanning Probe Microscopy
STM	Scanning Tunneling Microscopy
UHV	Ultra High Vacuum
XPS	X-ray Photoelectron Spectroscopy

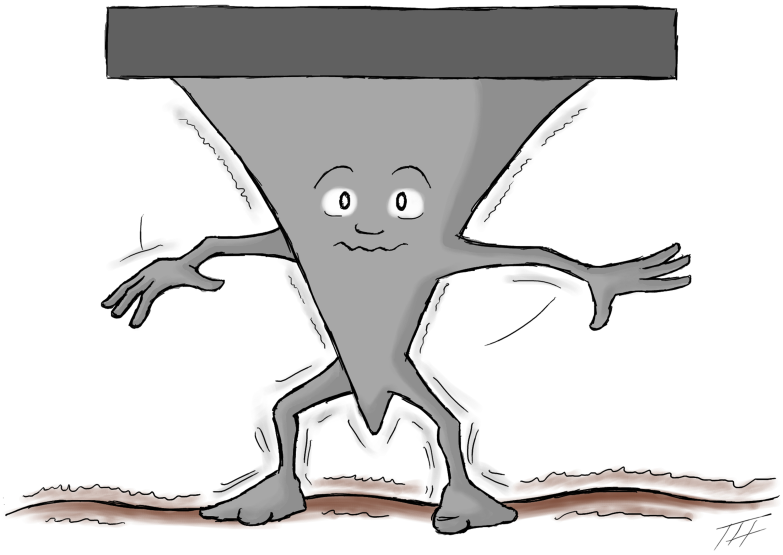

Abstract

Friction is one of the physical phenomena, which maybe is one of the greatest challenges to the scientific and industrial communities and has a direct linkage to energy efficiency and environmental cleanliness of all moving mechanical systems. In everyday life, one rarely thinks about friction or appreciates its importance, but there is no doubt that it is a major cause of energy loss. Hence, the prospect of further understanding and reducing friction in engineering systems has real-life and economic implications for not only preserving our limited energy resources, but also in saving our planet from hazardous emissions for generations to come.

On the macroscopic scale, the da Vinci-Amonton laws are common knowledge (1. friction is independent of the apparent contact area, 2. friction is proportional to the normal load and 3. friction is independent of velocity). With the invention of the Atomic Force Microscope in 1986, a modern field of tribology developed which made it possible to investigate friction on the microscopic scale. Experiments with small contacts have shown that the abovementioned empirical laws are not always correct. Reasons may be related to a larger surface-to-volume ratio and the greater importance of adhesion, surface chemistry and surface structure. By these means, a better understanding of the phenomenon of friction is required, to learn how to quantify and eventually how to control friction.

The central topic of this thesis concerns friction on the atomic scale. With the Friction Force Microscope, that is operated in ultra high vacuum and at room temperature, the friction of a single asperity contact between a sharp probing tip and a flat surface has been investigated. This is in contrast to the friction between two bodies on the macroscopic scale, where the contact is formed by a multitude of asperities. This single asperity is dragged over the surface by a support. While the support is moving with constant velocity, the tip apex itself typically exhibits a stick-slip motion, where the tip periodically sticks in a potential well, until the pulling force is high enough to overcome the static force and to induce a slip event, where the tip jumps into an adjacent potential well. The stick-slip process has been studied and analysed profoundly by experiments and numerical calculations by means of the tip motion on the surface lattice, also with respect of the limit cases of the superlubricity regimes.

The influence of the applied load on the stick-slip motion was experimentally and numerically investigated and indicates that the friction force is decreasing when reducing the load, until the load reaches a critical threshold, below which the system enters the superlubricity regime. Numerical calculations indicate that a reduction in load enlarges the stability regions, where the tip apex position is in a potential well, and thus facilitates the tip to follow a trajectory with lower energy barriers.

The effect of mechanical actuation of the cantilever on friction has also been analysed experimentally and numerically. Numerical model calculations have been performed in two dimensions based on an integrator solving the Newton equation of motion. For the actuation in normal direction, the stability regions are shown to periodically expand and contract, and similar to a decreasing load allows the tip trajectory to explore regions on the potential energy surface with lower energy barriers. Mechanical actuation of the cantilever in normal direction was already shown experimentally by others to reduce the friction, an actuation of the torsional vibration mode is now demonstrated to also reduce the friction force.

The influence of the temperature on the stick-slip motion is investigated numerically by implementing Brownian motion of the tip apex, and indicates that the thermal noise allows the tip apex to overcome an energy barrier on the potential energy surface slightly earlier compared to the case at zero temperature and thus reduces the friction force. An increasing temperature is shown to decrease friction until a critical temperature is reached, above which the system enters the superlubricity regime, similar to the load and actuation dependence of friction.

The tip trajectory has been analysed in detail by numerical and analytical calculations with subject to the scan direction and offset, which allows to describe and quantify the angular dependence of static and kinetic friction for square and hexagonal lattice symmetries. Since the tip trajectory is not directly accessible in experiments, a method has been introduced which combines the horizontal and vertical deflections to determine the tip path also in experiments. Hence, several aspects of the stick-slip process were analysed thoroughly, which give new insight and an improved understanding of the friction on the atomic scale.

The second important topic of the thesis concerns resonance frequencies of a cantilever in contact. The contact resonance frequency depends on several parameters such as load, contact area, material properties of the tip apex and sample material, and can be measured and tracked in the experiment. The first mode of the normal and torsional contact resonance frequencies indicate a maximum when the contact is not stressed in the lateral direction. The contact resonance frequencies are decreasing shortly before a slip event, around which the contact resonances drop to its initial values, but can not be accurately followed, owing to the finite phase locked loop response time. Thus, the contact resonances may be used as an indicator of a forthcoming slip event. Such a behaviour might also be relevant for macro-slip events, such as earthquakes, where early warning systems are still missing. The contact resonance technique also appears to be sensitive to atomic defects. Atomic defects are detected for the normal and torsional modes, which are not clearly detected in the lateral force or in the vertical deflection channels. Additional excitation of the sliding system at the contact resonance reduces the friction and gives further

informations about the mechanical properties of the asperity contact and the sample material. Since the contact resonance frequency of the normal and torsional mode oscillations are tracked simultaneously to the lateral force, a contact resonance map is generated in addition to the friction force map, which is presented on the atomic scale for the first time.
In summary, several aspects of friction, especially the stick-slip process, and contact dynamics, including the contact resonance frequencies, have been thoroughly investigated on the atomic scale.

Preface

The domain of this thesis concerns the field of tribology. The name tribology arises from the greek word *tribos*, which means friction, and is the science of friction, abrasion, wear and lubrication of interacting surfaces which move relatively to each other. This field of research and application is relatively young and is based on the interdisciplinary collaboration of physicists, chemists and engineers. In the last decades, tribology has increased in prosperity. This development is a consequence of the increasing complexity and refinement of technology in several areas, for instance in transport, space travel, robotics or medical technology, and also the demands in security and reliability. The advances in tribology are facilitated by technical instruments with increasing precision for the analysis and handling of materials, for instance the Electron Microscope, Atomic Force Microscope, X-ray radiation, laser, plasma, ion and neutron irradiation.

The instrument used for the experiments in this thesis is a Friction Force Microscope, which is basically an Atomic Force Microscope capable of measuring lateral forces. The ability to measure forces on the atomic scale makes it an ideal tool to study tribology on the microscopic area. The microscope was planned and built at the university of Basel and is considered to be of very high standard. The microscope is well damped and operated in ultra high vacuum, with a pressure comparable to the pressure in aerospace, which is at the limit of what is technically feasible. Comparing to the current technical standard, the experiments performed on this microscope are of clearly improved quality. Hence, having these conditions the experimental investigations presented within this thesis could be performed with high accuracy and excellent quality.

The central part of the thesis concerns the dynamics of the tip apex, which is dragged by a cantilever over the atomically flat surface. The tip motion is investigated profoundly in the stick-slip regime, as well as in the different superlubricity regimes. The experiments are supported by numerical and analytical calculations, which assist in explaining the experimental data and offer valuable clues about the behaviour of the tip apex. Furthermore, the Friction Force Microscope is combined with the contact resonance technique, which gives additional information about contact dynamics and includes the possibility of determining mechanical properties. This Contact

Resonance Atomic Force Microscopy is in principle not new, but is for the first time applied successfully on the atomic scale.
In Chapter 1 an introduction is given to Atomic Force Microscopy, describing the Microscope from a historical point of view and the development up to the present. The specific experimental setup is then described in Chapter 2 together with the sample and cantilever preparation and the calibration. Chapter 3 concerns the atomic scale friction, in particular the phenomenon of stick-slip. The tip dynamics are analysed in the superlubricity regime and systematically investigated with numerical model calculations. The discussion about the stick-slip process is then extended to superstructures and the occurrence of multiple slips. In Chapter 4 the contact resonance technique, also known as Contact Resonance Atomic Force Microscopy, is studied for the flexural mode. This technique is adapted on the atomic scale yields in an improved understanding of the contact mechanics. Chapter 5 is focused on the contact resonance technique for the torsional vibration mode, which is also applied to the atomic scale. For both, the flexural and torsional mode, the possibility of detecting surface defects is examined. In Chapter 6 the static and kinetic friction are discussed in dependence on the scanning direction. A profound analysis using numerical and analytical calculations is performed and compared to experimental data. The code for the numerical calculations is attached in the Appendix.


KATZEN FALLEN IMMER AUF DIE BEINE, MARMELADENBROTE IMMER AUF DIE MARMELADENSEITE. WAS WÄRE ALSO INTERESSANTER, ALS EIN MARMELADENBROT AUF EINE KATZE ZU SCHNALLEN?
DAS ARME BROT.
WWW.NICHTLUSTIG.DE
NICHTLUSTIG

> *Durch unser Wissen unterscheiden wir uns nur wenig, in unserer grenzenlosen Unwissenheit aber sind wir alle gleich.*
>
> KARL RAIMUND POPPER

Chapter 1

Introduction to Atomic Force Microscopy

1.1 Historical Introduction

The magnification of the vertical surface features of an object, those features leaving the horizontal plane and extending in the vertical direction, have historically been measured by a stylus profiler, which was invented by Schmalz in 1928 [1]. This stylus profiler utilised an optical lever arm to monitor the motion of a sharp probing tip mounted at the end of a cantilever. The magnified profile of the surface was generated by recording the motion of the stylus on photographic paper. More than 50 years later, the origin of the Scanning Probe Microscope (SPM) began with the development of the Scanning Tunneling Microscope (STM) in 1982 by Binnig and Rohrer [2]. For the first time it was possible to observe single atoms on a flat metallic surface in real space. Only one year later Binnig *et al.* presented the atomic structure of the Si(111) reconstruction [3]. For their pioneering achievement, Binnig and Rohrer were awarded with the Nobel Price in 1986. During the following years many spectacular high resolution images of metallic and semi-conducting surfaces were published. However, STM is based on the measurement of the tunneling current and is thus limited to electrically conducting samples. Motivated by the atomic forces that start to act at the tunneling distance [4], Binnig initiated the development of a microscope that uses those forces as a detection signal. A functional prototype of a Atomic Force Microscope (AFM) was built together with Quate and Gerber, and presented in 1986 [5]. In contrast to STM, the AFM technique allowed also to image insulating samples. It was in 1987 when Binnig *et al.* succeeded in obtaining the lattice image of a graphite surface [6]. After that, AFM was believed to be an atomic resolution microscope even in ambient atmosphere, i.e. not only in UHV. It was also in 1987 when Mate *et al.* discovered that an AFM can be used for the detection of friction, i.e. as a Friction Force Microscope (FFM), to obtain lateral force images with lattice periodicity [7]. In 1990, Meyer and Amer managed to image the lattice of the NaCl(001)surface in UHV [8]. After that, AFM got widely accepted and believed to be a microscope with atomic resolution under certain conditions. In the following two decades, both AFM and FFM became a standard technique that is widely used in industry, and appear nowadays in many modified variations.

1.2 Atomic Force Microscopy

Using an AFM, interaction forces can be measured down to the piconewton range. The force sensor consists of a microfabricated cantilever [9] with a sharp tip attached to its end (for more details see Section 2.2). The bending and twisting of the cantilever are detected as a measure of the normal and lateral forces acting on the tip. AFM is used for all kind of surfaces, in contrast to STM which is restricted to electrically conducting samples. There are several other members in the AFM family, which measure other quantities as electric [10] and magnetic [11] properties of surfaces, friction forces [7] and contact potentials [12]. Beside imaging surfaces, AFM has the opportunity to manipulate atoms or molecules in a controlled way [13] and also to perform various types of spectroscopy [14]. The development of these new types of microscopes made it possible to study all kinds of phenomena on the nanometer scale, and a vast progress in nanoscience has been achieved.

The basic principle of not only AFM but all scanning probe microscopes (SPM) is the sharp tip, which scans the surface along a raster using a feedback controller to adjust the distance to the surface. The interaction forces are then recorded at every point of the raster and used for the feedback loop, which results in an image of the surface topography. Note, that in STM the topography of the surface is actually a map of constant density of states, whereas in AFM the situation is even more complex as the image arises from an interplay of several forces. However, the measured surface of a homogeneous surface is actually a good approximation of the real topography. Because the interaction forces between the probing tip and the surface has a near-field component, imaging the surface well beyond the resolution limit of far-field techniques as SEM or LM is feasible. Since the resolution of AFM is not restricted by the wavelength of light or electrons, the resolution is only limited by the geometry of the probing tip.

An AFM may be operated in static mode or dynamic mode, and in contact mode or non-contact mode. In the dynamic mode, the cantilever is excited by mechanical actuation at a resonance frequency, or at several resonance freuquency simultaneously, whereas in static mode, the cantilever is not excited at all. In non-contact mode, the dynamic mode is the most common, i.e. non-contact atomic force microscopy (NC-AFM), whereas in contact mode, both the static and dynamic modes are commonly used.

1.3 Friction Force Microscopy

The friction laws on the nanoscale differ drastically from those of macroscopic friction. For instance, the friction force between two macroscopically bodies in contact has been known since Coulomb to be independent of their relative velocity. In contrast, friction measurements on the nanoscale show non-trivial velocity dependence [15]. With the introduction of the first friction measurement technique on the atomic scale using AFM by Mate *et al.* in 1987, known as FFM or lateral force microscopy (LFM) based on AFM, a new branch of science known as tribology emerged. FFM provides a single asperity contact, in contrast to a multitude of microcontacts in macroscopic friction, and thereby enables fundamental understanding of tribological phenomena at nanoscales. The aim is to study tribological porperties like friction, wear, adhesion and lubrication on the nanoscale.

While the probing tip is in contact with the sample surface, FFM monitors the torsion of the cantilever as the sample is laterally displaced. Typically, the deformation of the cantilever, i.e. the vertical bending due to normal forces and the torsional bending due to lateral forces, is simultaneously recorded by a four-quadrant photodiode (see Section 2.2). The image obtained from the vertical deflection is commonly called "AFM" image, whereas the image obtained by tracking the torsional motion of the cantilever is known as "FFM" image. Naively, this dual force imaging is trivial to implement, but if the preparation is not carefully performed, great difficulties arise when analyising the data [16]. For instance, there is always a crosstalk or coupling between the normal and lateral response of the cantilever. And because the ratio between the torsional and normal spring constant is usually high, in the case of rectangular contact cantilevers in the order of ≈ 100 , resulting in a relatively small frictional force signal. Other effects like the misalignment of the system or the position of the laser spot on the cantilver have also be taken into account. Nevertheless, the force calibration using rectangular cantilevers (see Section 2.3) is nowadays widely accepted.

The lateral force measured on a well-defined surfaces can exhibit atomic-scale features. Usually, a sawtooth-like pattern is observed, with the periodicity of the surface lattice. This phenomenon is called stick-slip. While the contact is locked in a stable position, the lateral force increases until it is strong enough to initiate a slip to the next stable position on the surface. Furthermore, when the scan direction is reversed, the lateral force exhibits a hysteresis. The energy dissipated can then be directly calculated from the area enclosed by the friction force loop. Understanding the underlying mechanisms and the controlled reduction of the friction forces, and thus on the reduction of the energy dissipation is a central matter of modern tribology on the nanoscale. Several techniques can be used to achieve the friction reduction in FFM. For instance, the load is reduced or the system is actuated using electrical or mechanical actuation. The latter technique is part of this work and is used not only to enter low friction regimes, but also to allow for gentle imaging without wear (see Section 3.8) and to obtain additional information, namely the contact resonances. Actuation and tracking of these contact resonances allow the FFM to be combined with the so-called contact resonance atomic force microscopy (CR-AFM).

> *Wohin Denken ohne Experimentieren führt, hat uns das Mittelalter gezeigt; aber dieses Jahrhundert lässt uns sehen, wohin Experimentieren ohne Denken führt.*
>
> ARTHUR SCHOPENHAUER

Chapter 2

Experimental Setup

2.1 The Ultrahigh Vacuum System

The experimental results presented in this thesis were performed using the home-built AFM, that is based on a prototype built in 1993 [17]. It is located in an UHV system [18], which is devided into three different chambers, as illustrated in Fig. 2.1. The lock chamber is connected to a turbo pump which allows to pump down to a pressure of $< 8 \times 10^{-8}$ mbar. The quick release fastener flange provides a fast tip and sample introduction. The lock chamber is connected to the preparation chamber where the main turbomolecular pump is connected to. There are several devices installed to enable tip and sample preparations. A molecular evaporator is used for deposition of alkali halide films (NaCl, KBr) on copper. The evaporation rates can be calibrated using the quartz micro balance. The manipulator contains of a resistive heater and an electron-beam heater. The resistive heater is used to get rid of water molecules and dust, whereas the latter is used for the preparation of metallic samples by Ar-sputtering using the sputter gun and annealing cycles. To cleave the ionic crystals in UHV, an in-situ cleaving knife is used. In addition to the main turbo pump, the preparation chamber is evacuated by a ion getter pump and a titanium sublimation pump. If necessarey, a mass spectrometer may be installed to detect impurities or to find a leak in the UHV system.

The main part of the analysis chamber is the hombe-built AFM operated at room temperature, which will be described in the next section in more detail. Beside the AFM, the analysis chamber contains an electron gun and screen for Low-Energy Electron Diffraction (LEED) and Auger Electron Spectroscopy (AES), as well as

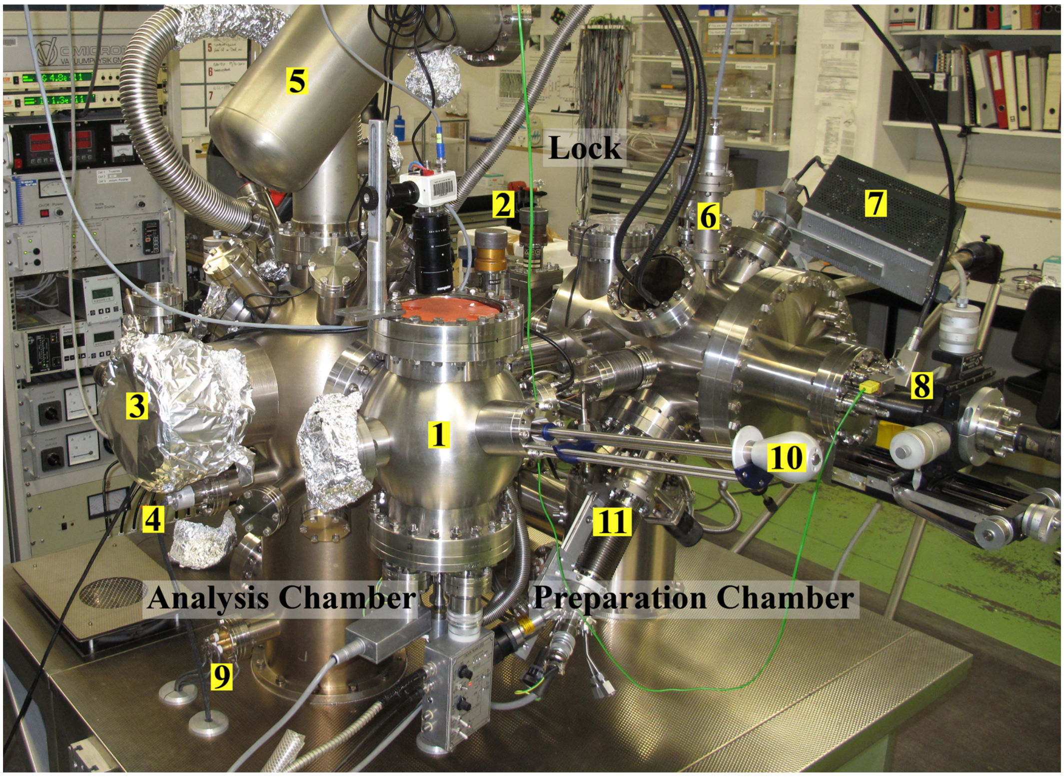

Figure 2.1: UHV system equipped with (1) AFM, (2) valves separating the three chambers, (3) LEED/AES, (4) pressure gauge, (5) XPS, (6) sputter gun, (7) mass spectrometer, (8) manipulator with heater, (9) titanium sublimation pump, (10) wobble stick and (11) a molecular evaporator with three Knudsen cells.

an X-ray Photoelectron Spectroscopy device (XPS). LEED is used to determine the crystalline structure of a surface, while AES provides information about the chemical composition of the sample. In the case of alkali halides and HOPG, the electron gun of the LEED is also used for the sample preparation. A short exposition of the NaCl(001) and HOPG surfaces to the electron beam creates straight-edged pits of one monolayer depth, as was shown earlier on KBr(001) [19–21]. These step edges are of interest for the friction measurement (see Section 3.8).
When evacuating the UHV system, first the rotary prevacuum and turbomolecular pumps are engaged. After a certain time, a pressure of 10^{-9} mbar is reached by only the turbomolecular pump. The residual gas contains mostly of water sticking to the walls of the chamber. After a bakeout of the whole system, most of the water is evaporated and pumped out. At this point, the ion getter pumps and titanium sublimation pumps are engaged to reach a base pressure in the low 10^{-10} mbar regime. During measurements the system is usually pumped by the ion getter pumps and titanium sublimation pumps, whereas the turbomolecular pumps are switched off to avoid mechanical vibrations. Inside the UHV system, the tips and samples are transferred using a system of manipulators and wobble stick.

2.2 The Atomic Force Microscope

The home-built AFM is based on a prototype built in 1993 [17] and is operated at room temperature. It is mounted on a stage which is suspended by four springs and damped by an eddy current damping system in order to decouple it from external vibrations. An image of the AFM is presented in Fig. 2.2. The deflection of the cantilever is detected by the optical beam deflection method [22], which is illustrated in Fig. 2.3 and allows to measure the normal and lateral bending of the lever simultaneously. The light of a superluminescent diode [23] is coupled into a gold coated glass fiber and introduced into UHV via a swagelock-feedthrough filled with teflon [24].

The light beam is then focussed by a lens system at controllable distance and guided over a first motorised mirror (hidden in Fig. 2.2) to the backside of the cantilever. The beam reflected at the cantilever is then guided over a second motorised mirror to the position sensitive four-quadrant diode. Both mirrors are accessible by piezo motors. The signal of the quadrant diode is directly amplified in UHV which guarantees a better signal to noise ratio with a bandwith of 3 MHz. The sample holder is mounted on a piezo tube, which performs the scan movement while the tip remains at a fixed position. The piezo tube allows a scan area of about 1 μm^2 as well as adjustment of the tip-sample distance of about 700 nm. Therefore the beam-lever system remains fixed during scanning of the sample. The piezo tube itself is attached to a sledge which can be moved in two dimensions by three piezo stacks for the coarse approach.

The cantilever is glued on the cantilever holder, that is mounted on a piezo crystal in order to excite the cantilever for non-contact and also contact-resonance measurements. In addition, the AFM may also be operated as an STM using the tunneling preamplifier with switchable resistor between $10^{-8} \rightarrow 10^{-10}$ Ohm. A bias voltage can be applied to either the tip or the sample in order to compensate the contact potential difference or for STM measurements.

2.3 Calibrations

The calibration procedure of the cantilever is one of the essential steps of FFM experiments. An accurate characterization is thus necessary for each cantilever. And the manufacturer's data are usually not accurate enough and may lead to errors of up to a factor 10 . Hence, each cantilever has to be characterised. The dimensions of the cantilever are either measured with Scanning Electron Microscopy (SEM) or Light Microscopy (LM). The relevant parameters determined this way are the length L, the width w, the position of the tip on the cantilever and the tip height h. Because the thickness t is small compared to the other dimensions and is not determined accurately enough using SEM, it is determined by the fundamental resonance frequency in the normal direction $f_1^0 = \omega_1^0/2\pi$ of the free cantilever [25]

$$t = \frac{2\sqrt{12}\pi}{1.875104^2}\sqrt{\frac{\rho}{E}} f_1^0 L^2, \tag{2.1}$$

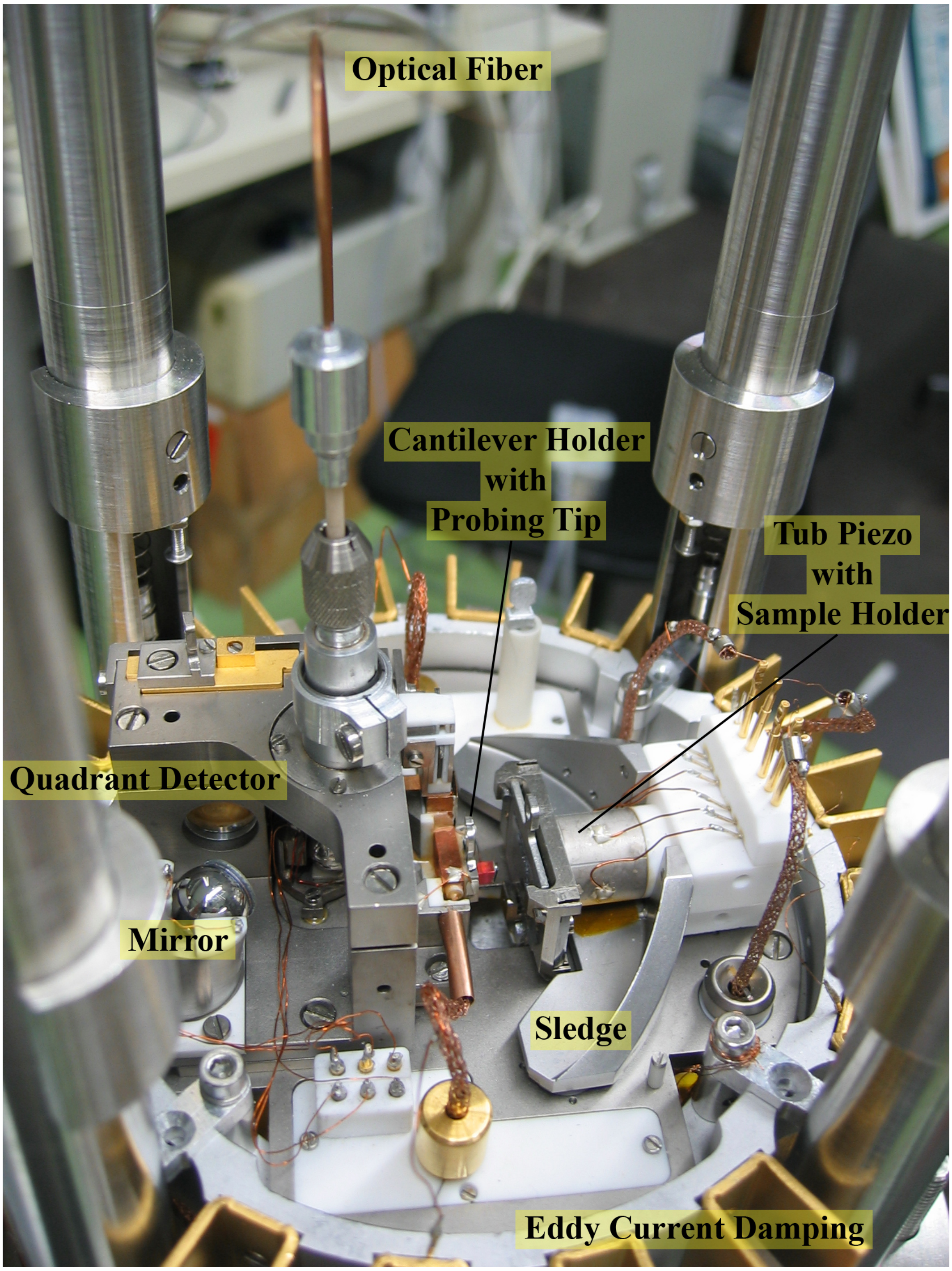

Figure 2.2: Picture of the home-built AFM during maintenance work.

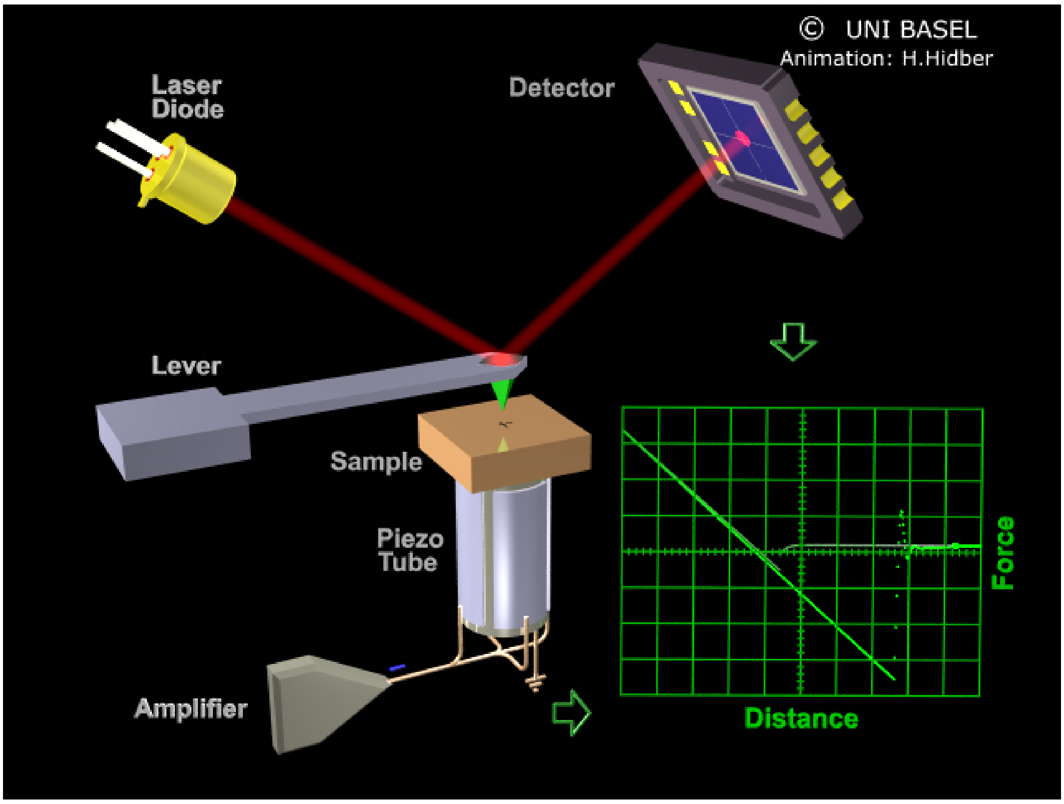

Figure 2.3: The light of a superluminescent diode is reflected at the front of the cantilever and fed into a four-quadrant diode. The sample is moved by a piezo tube, wheras the cantilever system remains fixed.

where ρ is the densitiy of the cantilever (for silicon: $\rho = 2328.3\ \mathrm{kg/m^3}$) and E the elasticity modulus (for silicon: $E = 1.69\mathrm{e}11\ \mathrm{N/m^2}$) [26]. In Eq. (2.1) the cantilever is considered as a beam only, neglecting the tip. When these parameters are known, the normal spring constant k_{norm} and the torsional spring constant k_{tors} for a rectangular cantilever are given by [27, 28]

$$k_{\mathrm{norm}} = \frac{Ewt^3}{4L^3} \quad \text{and} \quad k_{\mathrm{tors}} = \frac{Gwt^3}{3h^2L}, \tag{2.2}$$

where G is the shear modulus (for silicon: $G = 6.8\mathrm{e}10\ \mathrm{N/m}$). For the beam deflection type SPM (see Fig. 2.3), the sensitivity of the photodetector s_{z} [m/V] is determined by the z-spectroscopy, i.e. by measureing the force versus distance curve, as illustrated in Fig. 2.4. Force-distance curves should be performed before and after experiments to exclude changes of s_{z} due to variations in the intensity of the laser or the laser beam position on the cantilever. Here, the elastic deformation of the tip and the sample are assumed to be negligible compared to the bending of the cantilever.

Thus the movement of the z-piezo z_{p} is equal to the cantilever deflection z_{c}. The normal force F_{N} and lateral force F_{L} are a function of the differential signal from the photo diode in normal direction $U_{\mathrm{A-B}}$ and lateral direction $U_{\mathrm{C-D}}$, respectively, namely [28]

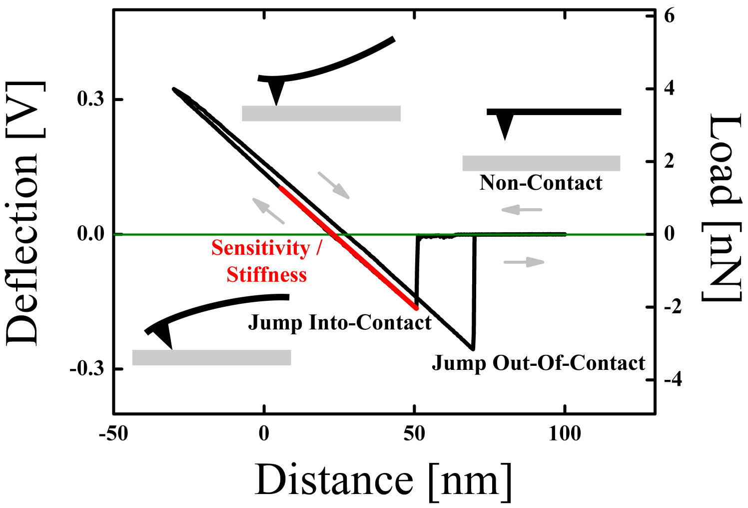

Figure 2.4: A force-distance curve, i.e. z-spectroscopy, measured on an atomically flat NaCl(001). The slope of deflection versus distance corresponds to the inverse of the sensitivity in z-direction s_z and is used to determine the normal force (load).

$$F_\mathrm{N} = k_\mathrm{norm} s_\mathrm{z} U_\mathrm{A-B} \tag{2.3}$$

$$F_\mathrm{L} = \frac{3}{2} k_\mathrm{tors} \frac{h}{L} s_\mathrm{z} U_\mathrm{C-D}. \tag{2.4}$$

In the ideal case, when the laser beam on the position-sensing four-quadrant diode is circularly shaped, s_z is identical for both the vertical and horizontal direction, as assumed in Eq. (2.4). However, as the laser beam is more elliptical, the sensitivities have to be adjusted by a factor [29]. In addition it is important to position the laser beam right above the probing tip, else the calibrations in Eq. (2.4) need to be adjusted [28] and the signal-to-noise ratio is decreased.

2.4 Properties and Preparation of the Cantilevers

The cantilevers used in the experiments are commercial, microfabricated, rectangular cantilevers [9] with integrated tips as a force sensor. Nowadays most cantilevers are produced in a microfabrication process using established methods from the semiconductor industries. The material of choice is highly n-doped silicon, which avoids charging and allows combined AFM-STM measurements. The tips are produced by etching processes and have a pyramidal shape. In order to obtain atomic resolution images, the tip apex should be as sharp as possible. The typical tip radius of the P-CONT cantilevers (see Fig. 2.5) used in this work is less than 7 nm [9], and the dimensions are given in Table 2.1.

Cantilever P-CONT		
DIMENSIONS		
Length	470 μm	± 2 μm
Length from chip to tip	445 μm	± 2 μm
Width	45 μm	± 2 μm
Thickness	1.787 μm	± 0.078 μm
SPRING CONSTANTS		
k_{norm}	0.123 N/m	± 0.015 N/m
k_{tors}	78.2 N/m	± 9.7 N/m
FREE RESONANCES		
Normal Resonance Frequency	11203 Hz	± 507 Hz
Torsional Resonance Frequency	200448 Hz	± 9125 Hz

Table 2.1: Dimensions and properties of the contact mode P-CONT cantilevers used in the experiments.

The P-CONT cantilevers have a spring constant in the order of $k_{\text{norm}} = 0.123$ N/m for the normal bending and $k_{\text{tors}} = 78.2$ N/m for the torsion. The stiffnesses slightly change from tip to tip (even from the same waver) because the thickness of the cantilevers are varying, which has a major influence on the spring constants and also on the resonance frequencies. The normal spring constant is that low, that the tip jumps into contact as soon as the attractive forces are high enough. Also cantilevers with a reflective coating (P-CONTR) [9] have been tested, which causes more light to be reflected and thus lead to an improved sum signal. However, the reflective coating have a less distinct contact resonance peak, i.e. a much lower Q-factor, and are therefore disadvantageous for the contact resonance measurements. The cantilevers are glued onto a tip holder [18] which guarantees a correct optical path in the system. After the transfer of the cantilver into the UHV, they are heated to a temperature of 120 °C for at least one hour in order to remove the water film and contaminants. However, the cantilevers are not sputtered, i.e. the native oxide layer is not removed.

2.5 Sample Preparation

Under atmospheric conditions, the sample is covered by all kinds of particles and adsorbates, which form an adlayer. Even though for the most part it is water, the chemical composition and geometrical structure of these adlayers are usually not well defined. The samples exposed to atmospheric pressure are complex and hinder a clear analysis of the underlying surface structure. Also the controlled adsorption of another material is hindered. In UHV there are several techniques for the preparation of clean and well defined surfaces. Brittle materials, such as alkali halides, are prepared by cleaving. A proper cleaving can only be achieved in certain crystallographic direction.

Most of the experiments which are presented in the following chapters are mainly

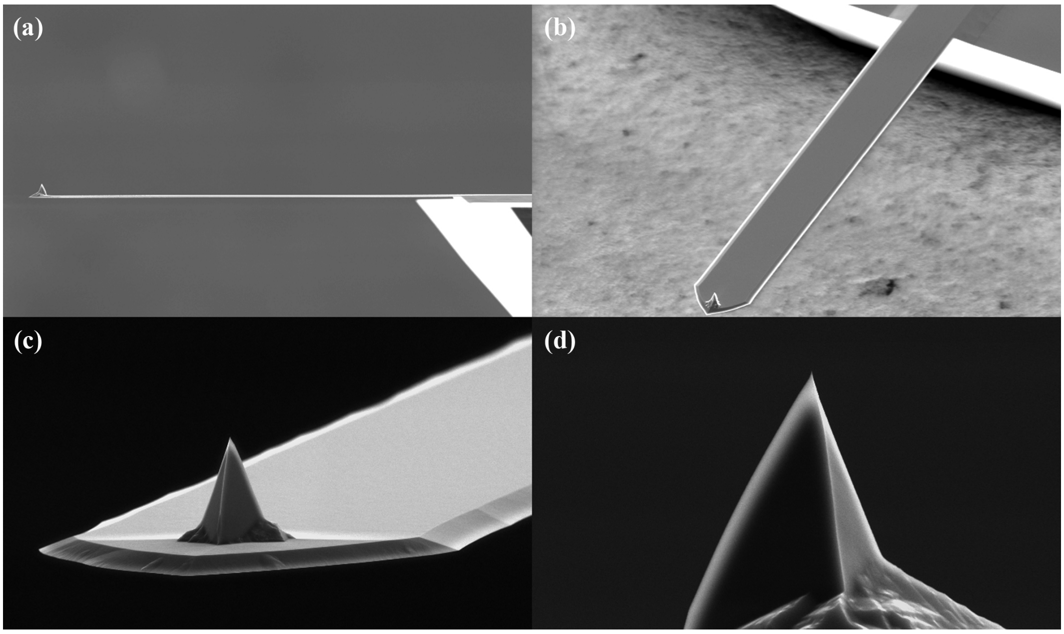

Figure 2.5: Scanning electron microscopy image of a rectangular silicon cantilever of type P-CONT with a magnification of (a) 216×, (b) 250×, (c) 2000× and (d) 5000×.

performed on alkali halides, namely on sodium chloride (NaCl), potassium bromide (KBr) and a mixed crystal ($NaCl_{90}Br_{10}$) containing 90 % chloride and 10 % bromide. The ratio is not always homogenously distributed and may exhibit more than 10 % bromide on the surface. These alkali halides are used as a model system for fundamental research in friction due to their simple structure and their reproducible preparation by cleaving. When the insulating ionic crystal is cleaved, the crystal and especially the region below the cleaved surface are plastically deformed due to the large stress of the cleaving process [30]. For this reason the crystal surface is usually charged after cleaving. These residual charges on the surface make it difficult to image the surface by SPM. One possibility is to apply a bias voltage between the tip and surface while measuring in order to reduce the electrostatic forces, but often the maximal applicable voltage of the system is not enough. The other possibility is to heat the crystal in UHV to around 120 °C, which normally reduces drastically the surface charges and still preserves the stoichiometry of the crystal. In addition, heating the crystal in UHV to even higher temperatures of around 300 °C to 400 °C results in a smoothing of the cleavage steps. Beside cleaving the crystal in UHV, it is also possible to cleave in air and immediately introduce the sample into the vacuum chamber. This resulted in less surfaces charges compared to the cleavage in UHV, but possibly to lower terrace width, which are typically between 50 nm and 150 nm.

For metal surfaces, sputtering and annealing cycles are the most common and versatile cleaning technique. By the bombardment with noble gas ions, the contaminants and also the topmost atomic layer of the crystal can be sputtered off. The subsequent annealing is necessary to remove embedded and adsorbed noble gas atoms as well as to recover the surface structure. As a side effect further impurities from the bulk segregate to the surface while annealing. Thus the sputtering-annealing cycle has to be repeated several times [31]. In the case of Cu(001), several cycles of 20 minutes argon-ion sputtering using $E = 1$ keV followed by 20 minutes annealing at 450 °C are required.

The deposition of thin films of alkali halides is performed using the Knudsen cell. For the deposition of NaCl, the Knudsen cell is heated to 320 °C and the sample, i.e. Cu(001), to around 80 °C to facilitate the formation of islands. The evaporation rate of the Knudsen cell is determined using a quartz balance, and the thickness of the deposited material, i.e. the number of monolayers, is then controlled via the evaporation time.

A further possible treatment for alkali halides and also for HOPG is the electron bombardement. In order to obtain pits in the surface with monoatomic depth, the sample is exposed for several seconds to the electron beam generated by LEED [21]. The electrons with an energy of $E = 1$ keV form excited colour centres inside the top layers of the crystal which diffuse to the surface and leave the sample, forming stoichiometric pits [19]. However, this radiation process, which is mainly performed to create step edges, is a quite intuitive process.

Der Verstand schöpft seine Gesetze nicht aus der Natur, sondern schreibt sie dieser vor.

Immanuel Kant

Chapter 3

Atomic-Scale Friction on Alkali Halides and HOPG

3.1 Introduction

Only one year after the invention of AFM by Binnig *et al.* in 1986 [5], Mate *et al.* discovered that an AFM can be used for the detection of friction, i.e. as a FFM, to obtain lateral force images [7]. The lateral force measured on a well-defined surface may exhibit atomic-scale features. Usually, a sawtooth-like pattern is observed, which shows the periodicity of the surface lattice. This phenomenon is called stick-slip. This chapter is focussing on a detailed discussion about this stick-slip phenomenon. Numerical and analytical calculations are performed and compared to experimental data [32], which give an improved understanding of the frictional behaviour on the nanoscale and the motion and dynamics of the tip apex. The tip movement is also traced back from the experiment, resulting in a tip trajectory on the calculated surface corrugation potential. Furthermore, the discussion of stick-slip is expanded to the multiple slip phenomenon, which also contain information about the damping of the lateral motion of the tip apex [33] and the limiting case, where the stick-slip goes over into a smooth sliding on the surface corrugation potential. The smooth sliding is related to the ultra low friction regime, i.e. the ”supberlubricity” state, and may be achieved by different mechanisms, which are studied in detail by experimental data as well as by numerical and analytical calculations.

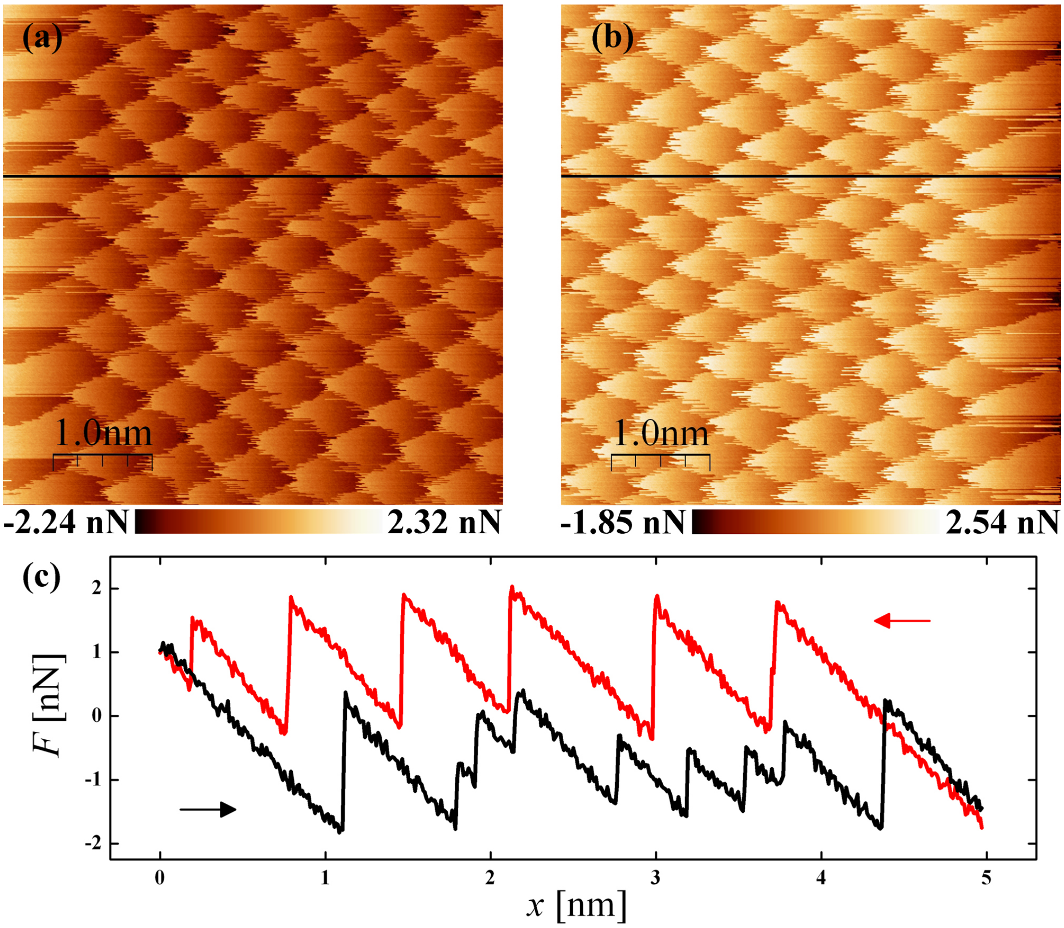

Figure 3.1: Raw data of lateral force maps for (a) the forward direction and (b) backward direction measured on KBr(001) using a load of 2.9 nN. (c) Profiles of the forward direction (black) and backward direction (red), which both point out the steep initial sticking stage before the first slip occurs. The area enclosed by the two profiles corresponds to the dissipation energy that is lost during the scan.

3.2 Atomic Scale Stick-Slip

A consequence of firstly, that the kinetic friction is decreasing with the sliding speed, and secondly that the static friction is higher than the kinetic friction, is the phenomenon of *stick-slip*. Instead of sliding at a constant speed, the sliding occurs as a sequence of sticking phases and slipping events. This stick-slip can manifest itself as an undesirable squealing noise, for example at a squeaky door hinge or the squeak of the chalk on a blackboard. In some cases, the stick-slip may also be intended, for instance when bowing the strings of a violin, which produces a musical tone. The stick-slip phenomenon not only exists on the macroscale, but also on the atomic scale. The process of stick-slip on the atomic scale can be readily observed using an AFM. Fig. 3.1(a,b) shows the lateral force maps for the forward and backward direc-

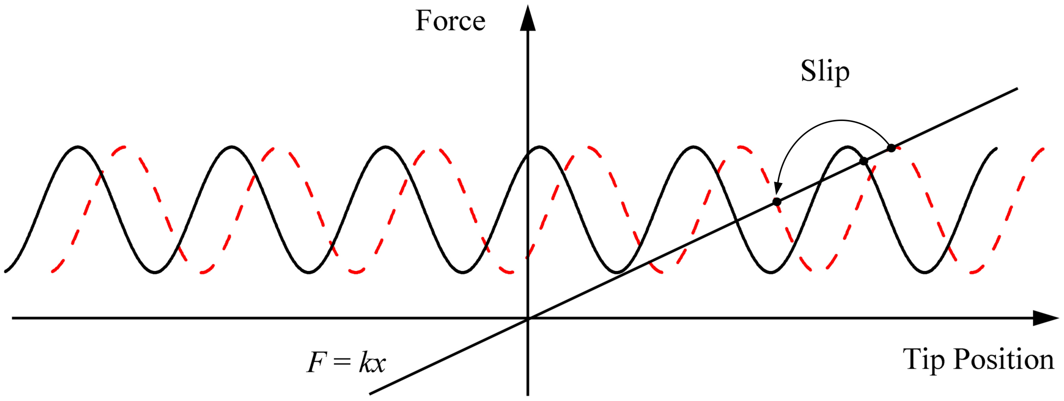

Figure 3.2: Negative force from the cantilever deflection, where k is the spring constant and x the tip displacement, and the friction force for two sample positions (black solid and red dashed lines) as the sample moves from left to right. The position of the tip on the surface is stable when the forces acting on the tip are balanced, as indicated by the intersection of the plots. When the surface is moved with respect to the tip, a slip occurs when the derivative of the frictional force at the intersection point is equal to the spring constant k.

tion. The experiment was performed on KBr(001) surface cleaved in UHV. Taking the profiles for the forward and backward direction results in a so-called friction loop, which is presented in Fig. 3.1(c). The AFM tip is sliding over the surface with a periodically stick-slip behaviour. The backward direction (red profile) exhibits stick-slip with the periodicity of the unit cell of KBr(001), whereas the lateral force profile for the forward direction (black) shows a stick-slip behaviour with more slip events. This refers to the tip jumping from one unit cell to an adjacent one by a zig-zag movement (for more details see Section 6.2). Note that the first slip event occurs when the lateral force acting on the tip exerts the static friction force, and therefore for the "initial sticking stage" is longer compared to the subsequent sticking stages. The area inclosed by the friction loop is referred to the energy dissipated during the scan.

The stick-slip process occurs when the spring constant of the cantilever along the scan direction is smaller than the spatial derivative of the friction force that the tip experiences when sliding over the surface. If the tip is sliding over a crystal surface with a periodic surface structure due to the crystal lattice, the tip experiences a lateral force with the same periodicity as the surface lattice. And when the slope of the decreasing part of the periodic force is bigger than the spring constant of the cantilever, the tip can slip to the next stable position, which is illustrated in Fig. 3.2.

Even though the lateral force map exhibit the atomic corrugation pattern, this does not imply that the tip produces lateral force maps with atomic resolution. In other words, the tip apex usually consists of several atoms or even hundreds of atoms at a blunt tip. The normal contact stiffness $k_{\mathrm{cont,norm}} = 17.65$ N/m from the experiment in Fig. 3.1 can be used to approximately estimate a small contact diameter of $k_{\mathrm{cont,norm}}/E^*_{\mathrm{eff}} = 0.7$ nm (cylinder on flat [34]), where an effective Young

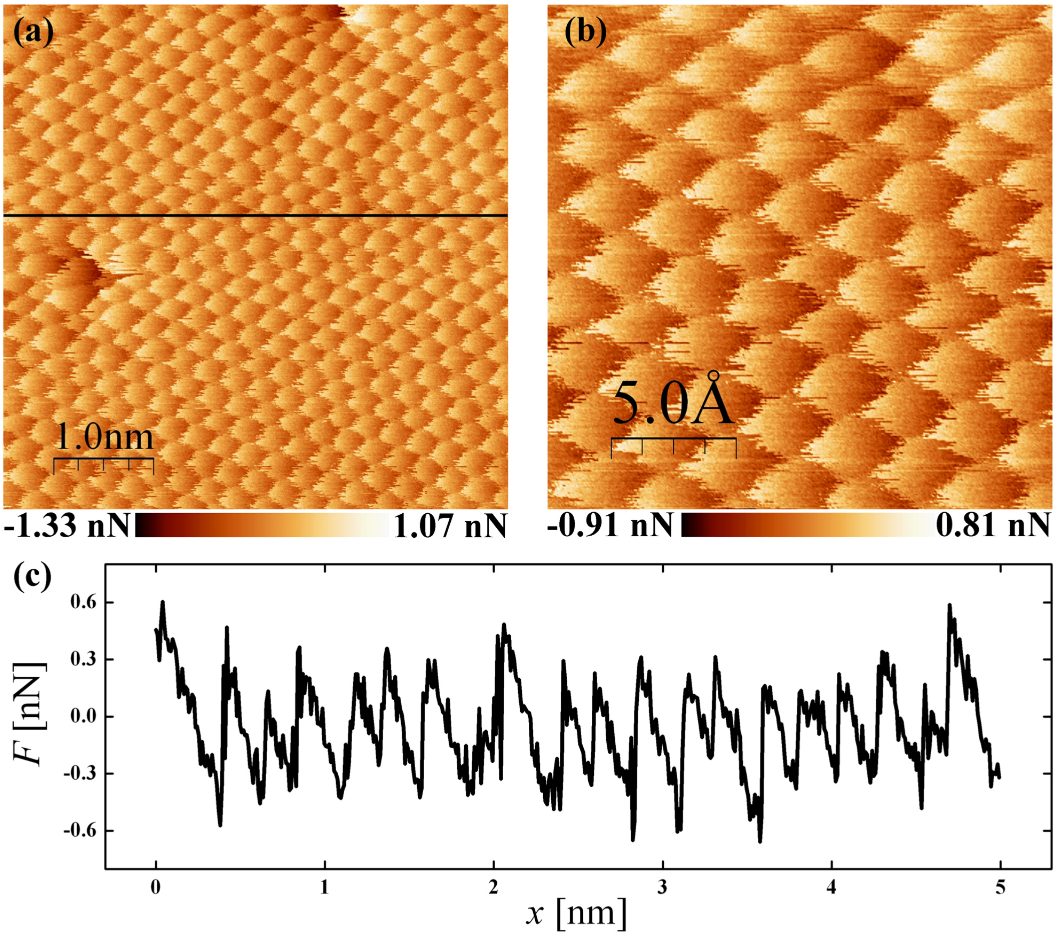

Figure 3.3: (a) Raw data of a lateral force map (5 nm × 5 nm) measured on a Cu(111) surface using a load of 1.0 nN. The irregularities in the surface lattice indicate defects in the copper. (b) The lateral force map (2 nm × 2 nm) clearly shows the atomic corrugation of the soft metal surface, which can only be measured under low load condition (zoom of (a)). (c) The profile taken from (a) exhibits the stick-slip motion with the atomic periodicity.

modulus $E^*_{\mathrm{eff}} = 24.7$ GPa was assumed (for more details see Section 4.2). The effective Young modulus is given by

$$\frac{1}{E^*_{\mathrm{eff}}} = \frac{1-\nu^2_{\mathrm{KBr}}}{E_{\mathrm{KBr}}} + \frac{1-\nu^2_{\mathrm{Si}}}{E_{\mathrm{Si}}}, \tag{3.1}$$

which takes into account the bulk Young moduli of NaCl ($E^*_{\mathrm{KBr}} = 26.87$ GPa) and Si ($E^*_{\mathrm{Si}} = 189.7$ GPa), as well as the Poisson ratios $\nu_{\mathrm{KBr}} = 0.20$ and $\nu_{\mathrm{Si}} = 0.33$. The estimated contact diameter states that the tip apex would consist of only oxidised silicon, the pattern of the lateral force map would hardly show the surface lattice of KBr(001). More likely, the tip apex consists of a flake of KBr that was picked up during scanning. By this means, the structure of the tip apex is commensurate with the structure of the surface lattice, and enables imaging the atomic corrugation

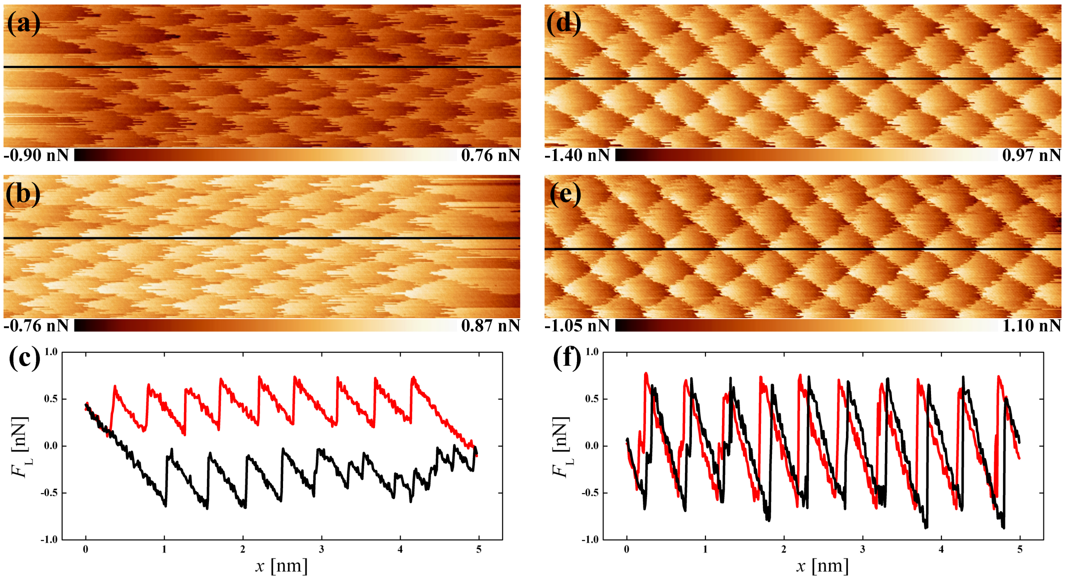

Figure 3.4: Raw data of lateral force maps (5 nm × 1.5 nm) measured on NaCl(001). (a,b) Forward and backward scans using a load of 4.9 nN. (d,e) Forward and backward scans using a load of 0.3 nN using the same cantilever. (c) Profiles taken along the scan line from (a) and (b). The average friction force is $\langle F_{\mathrm{L}} \rangle = 250$ pN and the profiles clearly exhibit a friction loop. (f) Profiles taken along the scan line from (d) and (e). The average friction force of $\langle F_{\mathrm{L}} \rangle = 54$ pN is much smaller, which implies that the friction loop is vanishing and the system is in the superlubricity regime.

pattern of the surface even without atomic resolution [7, 35–37]. Note that in the case of KBr, only one sort of atom is observed in the experiment, depending on the ionic kind of the furthermost atom of the tip apex [38].

Stick-slip and lateral force maps on soft metals like copper on the atomic scale are difficult to produce. The strong adhesion, chemical reactions and the soft contact make it complicate to properly image these surfaces. On copper, only the Cu(111) could be imaged [39], whereas other orientations of Cu were problematic. In Fig. 3.3 a lateral force measurement on Cu(111) is shown with enhanced resolution. The copper surface exhibits defects or impurities, which are only measured using a sharp tip and low load condition. The load of 1.0 nN allows to scan in the ultra low friction regime, in which wear and tip changes are reduced or even suppressed. A typical feature of scanning in the ultra low friction regime is that the initial sticking stage and the average lateral force of 32 pN are very small. Here, the lateral force indicates that the tip sticks behind the moving cantilever until the lateral force is high enough to induce a slip event, after which the tip is again preceeding the cantilever position. For more details of the ultra low friction regime see Chapter 4.

3.3 Transition from Stick-Slip to Superlubricity

An ultra low friction regime has been predicted by Sokoloff in 1984 for incommensurate sliding systems [40]. This phenomenon of ultra low friction has been named *superlubricity* by Hirano *et al.* [41], who first observed reduced friction as the sliding surfaces become incommensurate. The term superlubricity is something of a misnomer, because the resistance to motion is never completely absent in experiments, as it is for other "super" effects in physics, for instance in superconductivitiy or superfluidity. In other words, the lateral force $F_\mathrm{L} \neq$ is not zero but the mean friction $\langle F_\mathrm{L} \rangle$ vanishes. Sometimes, the superlubricity state due to the incommensurability is stated as structural superlubricity. However, since the tip sizes are considerably small and the fact that often a commensurate flake is picked up during scanning, the so-called "structural superlubricity" is not discussed within this thesis.

Beside the structural superlubricity, there are various ultra low friction regimes that have different origins (see also Section 3.4). In 2004 Socoliuc *et al.* demonstrated that the tip motion can enter in a superlubricity regime if the applied load is below a critical threshold [42]. Above the critical threshold the dependence of the friction force is nearly linear to the applied load on the contact. However, recent measurements on NaCl(001) indicate, that this dependence is not linear at all loads, but is also influenced when multiple slips start to initiate, which is in contradiction to literature. In Fig. 3.4(a,b) the friction measured on NaCl(001) is shown for a load of 4.9 nN, which is clearly above the critical threshold. The common stick-slip behaviour with a distinct frictionloop is observed, as indicated in the profile Fig. 3.4(c). Using the same cantilever, the load is then reduced to 0.2 nN in Fig. 3.4(d,e), where the friction loop is vanishing (Fig. 3.4(f)) and the average friction force is slightly above the detection limit ($\langle F_\mathrm{L} \rangle = 54$ pN). This superlubricity regime is also stated as the "static superlubricity" and can be applied straight-forward in the experiment, provided that the contact area is small enough, and facilitates scanning the surface without tip changes, plastic deformation or wear. For the theoretical explanation see Section 3.4.

The actuation of the contact in the normal direction, due to excitation of the first flexural contact resonance, was demonstrated by Socoliuc *et al.* to be another possibility to reduce friction and even enter a superlubricity regime [43]. Since the friction is active reduced by external mechanical excitation, where energy is dissipated, this state is also referred to "dynamic superlubricity". For the theoretical discussion see Section 3.4. Similar to the static superlubricity, the dynamic superlubricity regime is achieved, if the controlled actuation of the system exceeds a critical threshold. This result is reproduced on KBr(001) and NaCl(001) but is not shown here.

Theoretical calculations of Tshiprut *et al.* in 2007 predict indirectly, that the reduction of friction may also be achieved by the actuation of the lateral mode, i.e. the torsional vibration of the cantilever [44], which could not be demonstrated experimentally up to now. In contrast to the normal actuation, where flexural vibration of the cantilever and tip cause an oscillation of the corrugation potential energy, the torsional actuation, i.e. the lateral vibrations, acts as an (inplane) harmonic force along the scan direction. In Fig. 3.5 the dependence of the friction force on the torsional actuation is shown for a measurement on NaCl(001) using a load of

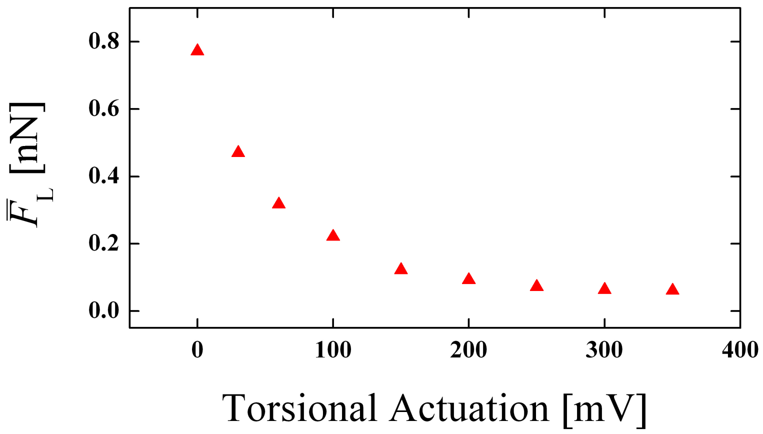

Figure 3.5: The average friction force is measured on a flat terrace of NaCl(001) using a load of 0.3 nN. The lateral force is averaged over the scan range without taking into account the initial steep sticking stage. The torsional contact resonance is tracked by a PLL using constant excitation. The curve clearly demonstrates that the torsional actuation reduces the friction while scanning.

0.3 nN and a constant excitation of the torsional contact resonance tracked by the PLL. The data points clearly show that the average friction force $\langle F_\mathrm{L} \rangle$ is reduced when the cantilever is excited torsionally. Similar to the normal actuation, the system enters the ultra low friction regime, which may be referred again to dynamic superlubricity, even though the experimentally determined average friction force is not equal to zero, but is below the detection limit. Hence, the normal and torsional actuation can both be used to reduce friction and wear on the nanoscale.

3.4 2D Simulations based on the Prandtl-Tomlinson Model

Macroscopic friction between solids is well known to be both of high practical importance and of notorious difficulty regarding its theoretical understanding. Technical solutions, such as bearings or liquid lubricants can reduce friction at macroscopic dimensions. But in the microscopic range, for instance in micro- or nanoelectromechanical systems (MEMS/NEMS) other approaches and ideas are required. The study of friction reduction of a single contact has gained relevance in the field of nano-technology. Friction at the atomic range is ideally explored by friction force microscopy (FFM), in which a tip apex consisting of only a few atoms is dragged across a solid surface [7, 17, 45–47]. Theoretically, atomic scale friction in the absence of wear, plastic deformation and impurities, can be interpreted using simple ball-and-spring models as the Prandtl-Tomlinson model [48, 49]. An overview of the field of computer simulations and theoretical modelling of friction, lubrication and wear has been recently given by Szlufarska *et al.* [50]. There are several ways to reduce friction. First, when the normal load acting on the tip decreases below a critical threshold, the characteristic stick-slip motion is suppressed and sliding occurs

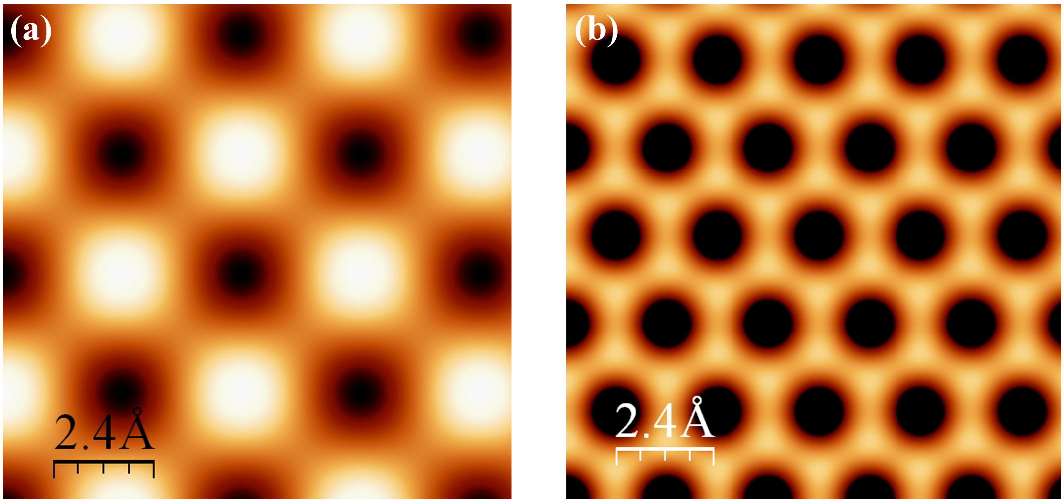

Figure 3.6: Potential energy surface of (a) NaCl and (b) HOPG with a sidelength of 1.2 nm. The unit cell parameter is 0.564 nm for NaCl and 0.246 nm × 0.426 nm for HOPG. In NaCl only one sort of atom is visible, depending on the tip apex. HOPG has a trigonal lattice because only the potential minima are detected (in the experiment).

smoothly without abrupt jumps and dissipation while the contact is maintained. This transition was observed on ionic crystals in ultra high vacuum (UHV) [42]. Second, ultra low friction is achieved while dragging two crystal surfaces out of registry against each other [37, 51, 52], which is not discussed in this section. Third, an actuation of the system at well defined frequencies facilitates the reduction of friction as well. For instance, an excitation of the cantilever in normal direction at the contact resonance frequency leads again to a remarkable reduction in friction and dissipation, as shown on ionic crystals, mica and HOPG [43, 53]. The concept of ultra low friction is often referred to superlubricity [54]. Unfortunately, the first technique to achieve "static" superlubricity cannot easily be applied in practical situations, because it requires detecting and maintaining very small and constant loads, and in addition, a switching between the usual state and the superlubricity state is not feasible. Hence, the latter technique is more promising, because higher loads are allowed and a switching between the usual dissipative state and the "dynamic" superlubricity state is possible. In this section, an extension of the theoretical model is reported, which describes the different types of superlubricity for different substrates in two-dimensions including thermal effects.

The system is described in terms of a simple model which is essentially a two-dimensional Prandtl-Tomlinson model [48, 49] for one asperity. The surface is modelled as a rigid lattice with square periodicity in the case of NaCl and trigonal periodicity in the case of HOPG. The tip is handled as a point-mass, that is coupled to a support ("chip of the cantilever") by springs in the x- and y-directions. Via these springs, the tip is dragged over the periodic lattice. The interaction of the tip with the atomic surface of NaCl is described by an adiabatic potential $V_{\mathrm{NaCl}}(\vec{r}_{\mathrm{tip}})$ [55], which corresponds to the first term of the two-dimensional Fourier series and has the form

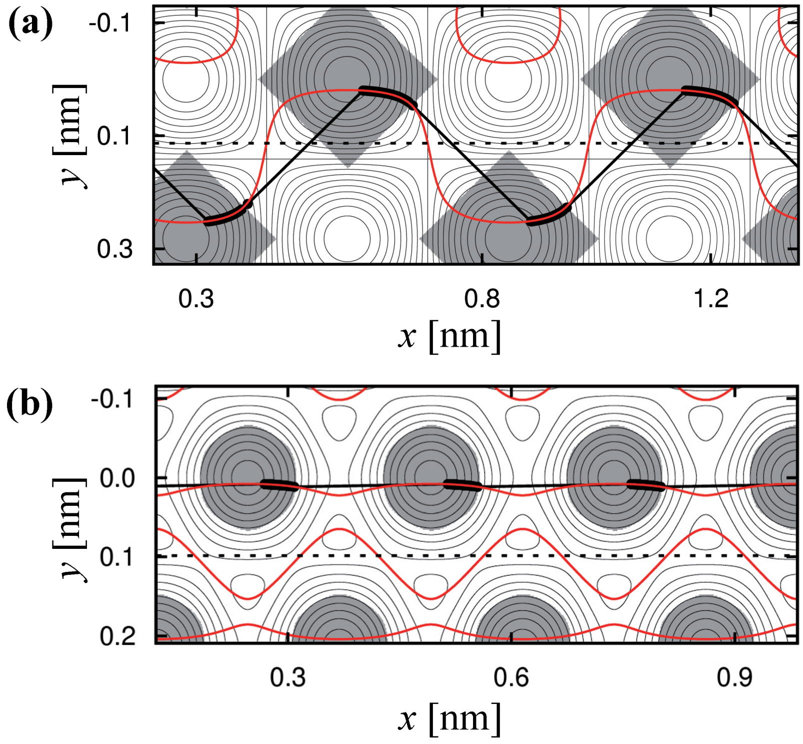

[t]

Figure 3.7: Contour plot of the potential $V_{\mathrm{NaCl,HOPG}}(x,y)$ for (a) NaCl with $E_0 = 1\,\mathrm{eV}$ and (b) HOPG with $E_0 = 0.5\,\mathrm{eV}$. The horizontal dashed line indicates the scanning line with (a) $y_{\mathrm{sup}} = 0.2\,a$ and (b) $y_{\mathrm{sup}} = 0.4\,a$. Grey regions correspond to $\lambda_{1,2}{>}0$. A superposition of the grey regions with the tip trajectory (red), where $\partial V/\partial y = 0$, leads to the analytical stick-slip motion of the tip, and is in very good agreement with the numerical solution at 0 K (black points connected by lines).

$$V_{\mathrm{NaCl}}(x,y) \quad = \quad -\frac{E_0}{2}\cos(\frac{2\pi}{a}x)\cos(\frac{2\pi}{a}y), \tag{3.2}$$

where $a = 0.564$ nm and (x, y) is the tip position. In the case of HOPG the interaction potential between tip and surface is described very similar to the potential used by Verhoeven *et al.* [51],

$$V_{\mathrm{HOPG}}(x,y) = -\frac{E_0}{4.5}[2\cos(\frac{2\pi}{a}x)\cos(\frac{2\pi}{a\sqrt{3}}y) + \cos(\frac{4\pi}{a\sqrt{3}}y)], \tag{3.3}$$

with $a = 0.246$ nm determined by the unit cell parameters of the HOPG surface. Furthermore, both lattices (see Fig. 3.6) can be rotated by a simple coordinate transformation, whereas the [100]-direction is defined as 0 degree in both NaCl and HOPG. An example of a HOPG surface rotated by $\varphi = 15°$ is shown in Fig. 3.8 (for more details of rotated systems see Chapter 6 which concerns the angular dependence of friction). It has to be mentioned that in the case of NaCl, only one sort of atom is observed in the experiment, depending on the ionic kind of the furthermost atom of the tip apex [38]. In the case of HOPG, only the "hollow" sites of the hexagonal carbon rings are imaged (which represent the potential minima), and not the profile of the maxima of the interaction potential (i.e. the positions of the carbon atoms). This leads to a three-fold symmetry with a distance of 0.246 nm between the minima [56]. Both $V_{\mathrm{NaCl}}(\vec{r}_{\mathrm{tip}})$ and $V_{\mathrm{HOPG}}(\vec{r}_{\mathrm{tip}})$ represent the shape of the periodic lattice, and have to be multiplied by a constant in order to obtain the corrugation potential amplitude E_0. The amplitude E_0 is related to the tip-sample interaction and thus to the externally applied load in the experiment, and is assumed to obey a linear dependence with respect to the load. This assumption is valid only for the repulsive regime and as long as no deformation occurs, which is usually the case for experiments in the low-nN range. The total potential energy including the elastic energy stored in the springs is given by

$$V(\vec{r}_{\mathrm{tip}}, \vec{r}_{\mathrm{sup}}) = V_{\mathrm{NaCl,HOPG}}(\vec{r}_{\mathrm{tip}}) + \frac{1}{2}k(|\vec{r}_{\mathrm{tip}} - \vec{r}_{\mathrm{sup}}|)^2, \tag{3.4}$$

where $\vec{r}_{\mathrm{tip}} = (x, y)$ is the position of the tip and $\vec{r}_{\mathrm{sup}} = (x_{\mathrm{sup}}, y_{\mathrm{sup}})$ is the position of the (microscope) support, and $k = k_{\mathrm{x-eff}} = k_{\mathrm{y-eff}} = 2$ N/m is the elastic spring constant in x- and y-direction, whereas the scanning direction is defined as the x-axis.

Two effective springs are used in the simulations, one for the x-direction and the other for the y-direction. Each of these effective springs represents the effect of several springs that are coupled in series. According to Carpick *et al.* [57] the effective spring constant is the reciprocal sum of the single spring constants,

$$k_{\mathrm{eff}} = \left(\frac{1}{k_{\mathrm{lateral}}} + \frac{1}{k_{\mathrm{contact}}}\right)^{-1}, \tag{3.5}$$

where k_{lateral} is the lateral spring constant of the cantilever, and k_{contact} is the lateral contact stiffness that describes the elastic deformation of the tip apex and the surface in contact at a given load. According to independent measurements on different systems [42, 43, 46, 58] the lateral contact stiffness k_{contact} is the softest spring and thus essential and decisive for k_{eff}. The lateral spring constant k_{lateral} is in general different for the x- and y-direction. The x-direction, which is the scan direction in the experiment, is perpendicular to the cantilever. Again, two springs contribute to the lateral spring of the cantilever: The torsion of the cantilever with its torsional spring constant k_{tors}, and the *in plane bending* of the cantilever with the bending spring constant k_{bend}. The torsional spring constant of a rectangular cantilever is [28]

$$k_{\mathrm{tors}} = \frac{Gwt^3}{3h^2 l}, \tag{3.6}$$

where G is the shear modulus, w the width, t the thickness, l the length of the cantilever and h the tip height. The bending spring constant is [59]

$$k_{\mathrm{bend}} = \frac{Etw^3}{4l^3}, \tag{3.7}$$

where E is the elasticity modulus of the cantilever. The torsional and bending spring constants are then combined to give the lateral spring constant in the x-direction [59]

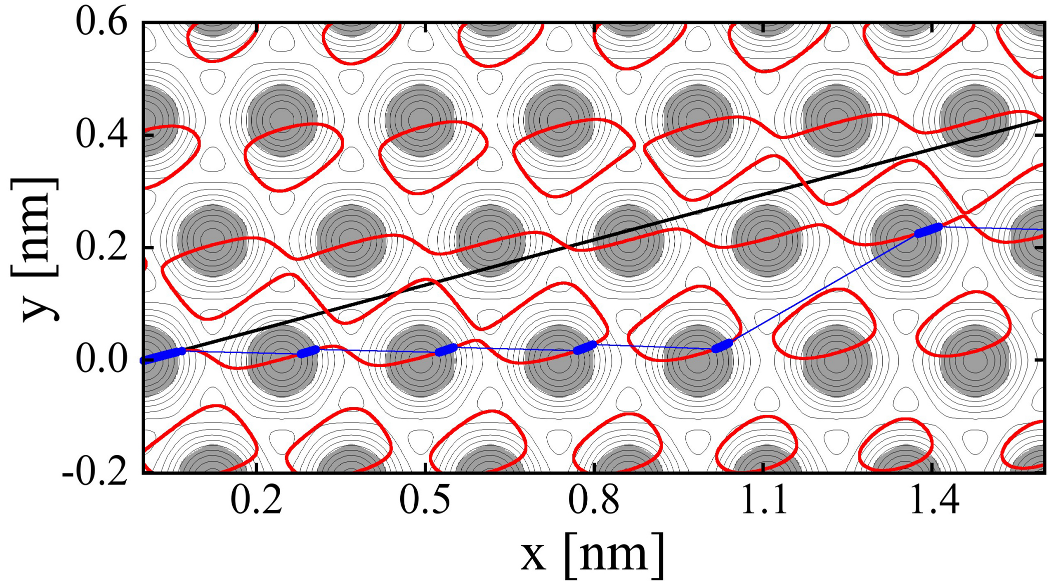

Figure 3.8: Contour plot of the rotated potential $V_{\mathrm{HOPG}}(x, y)$ for $E_0 = 1$ eV indicating that both potentials can readily be rotated to study also friction in dependence on the scan direction. The black lines indicate the scan line (support path). The shaded areas denote the stability domains of the tip motion. Inside those areas the computed tip trajectories (thick blue points) essentially coincide with the loci where forces balance in the quasistatic limit (continuous red curve) . Thin blue lines connect the initial and final tip positions in the course of slips between adjacent domains. The scan line and trajectory is shown for $\varphi = 15°$ and zero initial offset.

$$k_{\mathrm{x-lateral}} = \left(\frac{1}{k_{\mathrm{x-tors}}} + \frac{1}{k_{\mathrm{x-bend}}} \right)^{-1}. \tag{3.8}$$

With typical cantilevers used in the experiment (Nanosensors, type: PPP-CONT), a value of $k_{\mathrm{x-lateral}} \approx 25$ N/m is estimated. It is well known that the effective spring constant $k_{\mathrm{x-eff}}$ in x-direction can be extracted from the slope of the sticking part in the stick-slip curve [42]. Due to the reciprocal addition of the spring constants (see equation (3.5)), the effective spring constant k_{eff} is dominated by the weakest spring. Usually a relatively low effective spring constant is found in the experiment, of the order of $k_{\mathrm{x-eff}} \approx 2$ N/m [38], which is considerably lower than the lateral spring constant $k_{\mathrm{x-lateral}}$ itself. Hence the effective spring constant $k_{\mathrm{x-eff}}$ in x-direction is primarily determined by the lateral contact stiffness, which is $k_{\mathrm{x-contact}} \approx 2.2$ N/m for the values above. However the lateral contact stiffness depends strongly on the contact size and hence can vary significantly between tips with differing apex radii. In the simulation the spring constant for the x-direction is kept constant at $k_{\mathrm{x-eff}} = 2$ N/m.

The determination of the spring constant in y-direction is more difficult than for the x-direction. In principle, the equation (3.5) is also valid for the y-direction, but it is difficult to quantitatively analyze stick-slip motion in parallel to the cantilever in the experiment [60]. Therefore an effective spring constant $k_{\mathrm{y-eff}}$ can only be approximately estimated. The contact stiffness k_{contact} is assumed to be equal in both directions, and the lateral spring constant $k_{\mathrm{y-lateral}}$ of the cantilever is given by [59]

$$k_{\mathrm{y-lateral}} = \frac{Ewt^3}{12h^2l}. \tag{3.9}$$

Inserting the experimental values, $k_{\mathrm{y-lateral}} \approx 25$ N/m is obtained. It is remarkable that the lateral spring constant for both the x-direction and y-direction are in the same range. Because the effective spring constant $k_{\mathrm{y-eff}}$ is not known from the experiment, this parameter is varied in the simulations.

The lateral force acting on the support is simply given by the Hooke's law

$$F_{\mathrm{L}} = -k(x_{\mathrm{sup}} - x). \tag{3.10}$$

In FFM experiments, the lateral force F_{L} is measured only in the scanning direction. Therefore only the force acting on the support in x-direction is considered as the friction force. In this section, two different methods are applied to determine the tip motion and the lateral force. In the first method, the equation of motion of the tip at finite temperatures is solved, assigning a finite mass to the tip and introducing a viscous force hindering the tip motion. In the second method, analytical expressions are determined in the so-called "quasi-static" limit, where the tip motion is quite slow. The results of the numerical simulations have been analyzed and converted into images by means of the WSxM software [61].

The dynamics of the tip on the surface at finite temperatures can be described by the Langevin equation [62–64]

$$m\frac{d^2x}{dt^2} + m\gamma\frac{dx}{dt} + \frac{\partial V(\vec{r}_{\mathrm{tip}}, \vec{r}_{\mathrm{sup}})}{\partial x} = \xi(t). \tag{3.11}$$

The effective mass of the tip is assumed to be $m = 10^{-12}$ kg. Since there is no experimental estimate for the effective mass of the tip that corresponds to the stiffness of the tip, m was varied by several orders of magnitude for the simulation, but found to have no significant influence on the key results presented in this paper. Because the mass of the cantilever is many orders of magnitude larger than the mass of the tip, the thermal effects on the cantilever may be neglected. The Langevin equation for the y-direction is defined in the same manner. In addition to the Newton equation of motion, a term $\xi(t)$ is added which represents the Brownian motion of the tip. $\xi(t)$ is a Gaussian distributed random noise satisfying the fluctuation-dissipation theorem

$$< \xi(t)\xi(t') >= 2m\gamma k_{\mathrm{B}}T\delta(t - t'), \tag{3.12}$$

where the angular brackets denote the mean, k_{B} is the Boltzmann constant, $\delta(t - t')$ the delta function, and γ the damping coefficient of the tip movement. The temperature in the simulation is controlled and set to room temperature via $\xi(t)$. The Langevin equation is solved with an integration algorithm. A commonly used integrator for "Brownian dynamics" simulations is used, that is referred to the Ermak

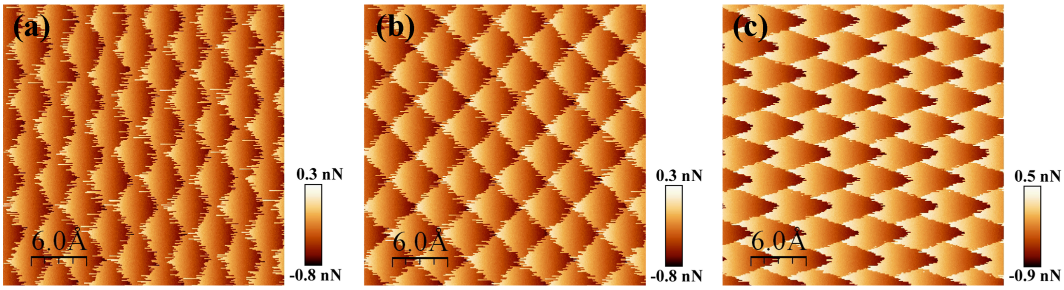

Figure 3.9: Calculated lateral force map of NaCl (forward scan direction) for different spring constants in y-direction, (a) $k_{\mathrm{y-eff}} = 1\,\mathrm{N/m}$, (b) $k_{\mathrm{y-eff}} = 2\,\mathrm{N/m}$ and (c) $k_{\mathrm{y-eff}} = 10\,\mathrm{N/m}$, whereas the spring constant in x-direction $k_{\mathrm{x-eff}} = 2\,\mathrm{N/m}$ is retained. The movement of the tip is heavily damped, thus an overshooting or jump over two lattice constants is avoided and the stick-slip behaviour is sustained. The lateral force maps reveal different patterns, however a good agreement with experiment is only achieved when $k_{\mathrm{x-eff}} \approx k_{\mathrm{y-eff}}$. The amplitude of the corrugation potential is $E_0 = 1$ eV.

algorithm [65]. This algorithm is an attempt to treat properly both the stochastic and dynamic elements of the Langevin equation. At low values of the damping coefficient γ, the dynamical aspects dominate, and the Newtonian mechanics recover as $\gamma \to 0$. The damping coefficient γ is set to 10 times the critical damping $\gamma_{\mathrm{critical}} = 2\sqrt{k/m}$. An overdamped motion of the apex is typical for nanoscale systems and avoids oscillations of the tip. Hence the overdamped system is always in an adiabatic state, as it is assumed in the quasistatic Tomlinson model [66]. Following the conditions of the experiment, the simulation is performed at room temperature and for a constant scan velocity of $v = 25$ nm/s. An appropriate time step of $\Delta t = 10^{-7}$ s is used for the support movement to achieve reasonable computation time without introducing artefacts.
At low temperature, the equation of motion of the tip can be solved analytically in a quasi-static limit corresponding to very low tip velocities, and is only suitable at very low temperatures. In such a case, the tip resides most of the time in the minima of the potential energy landscape $V(\vec{r}_{\mathrm{tip}}, \vec{r}_{\mathrm{sup}})$ (see equation (3.4)) and "jumps" from one minimum into an adjacent minimum when the driving force exerted by the support overcomes a critical threshold [67]. In the minimum positions the condition $\nabla V(\vec{r}_{\mathrm{tip}}, \vec{r}_{\mathrm{sup}}) = 0$ has to be satisfied. Substituting $\vec{r}_{\mathrm{sup}} = (vt, y_{\mathrm{sup}})$, where v is the velocity of the support and y_{sup} is a constant, one can easily see that the tip trajectory is defined by the condition $\partial V/\partial y = 0$, whereas $\partial V/\partial x = 0$ gives the time dependence of the tip coordinates. Using equation (3.4) in the condition $\partial V/\partial y = 0$, one gets

$$\frac{E_0\pi}{a}\cos(\frac{2\pi}{a}x)\sin(\frac{2\pi}{a}y) + k(y - y_{\mathrm{sup}}) \quad = \quad 0 \tag{3.13}$$

for the tip trajectory on NaCl and

$$\frac{8E_0\pi}{9\sqrt{3}a}(\cos(\frac{2\pi}{a}x)\sin(\frac{2\pi}{a\sqrt{3}}y)+\sin(\frac{4\pi}{a\sqrt{3}}y))+k(y-y_{\mathrm{sup}})=0 \tag{3.14}$$

on HOPG, respectively. Examples for these tip trajectories on NaCl and HOPG are shown in Fig. 3.7. However the tip can only reside at points where the system is in stable equilibrium. In order to define these positions, the Hessian matrix $\mathcal{H}=(\partial^2 V/\partial x_{\mathrm{i}}\partial x_{\mathrm{j}})$ of the total potential is evaluated and its two eigenvalues $\lambda_{1,2}$ are determined [55,68]. These eigenvalues have the form

$$\lambda_{1,2}^{\mathrm{NaCl}}=k+\frac{2E_0\pi^2}{a^2}\cos(\frac{2\pi}{a}x\pm\frac{2\pi}{a}y) \tag{3.15}$$

in the case of NaCl and

$$\begin{aligned}\lambda_{1,2}^{\mathrm{HOPG}} = \quad & k+\frac{16E_0\pi^2}{27a^2}\bigg(2\cos(\frac{2\pi}{a}x)\cos(\frac{2\pi}{a\sqrt{3}}y)\\ & +\cos(\frac{4\pi}{a\sqrt{3}}y)\pm\big(\cos^2(\frac{2\pi}{a}x)\cos^2(\frac{2\pi}{a\sqrt{3}}y)\\ & +\cos^2(\frac{4\pi}{a\sqrt{3}}y)+3\sin^2(\frac{2\pi}{a}x)\sin^2(\frac{2\pi}{a\sqrt{3}}y)\\ & -2\cos(\frac{2\pi}{a}x)\cos(\frac{2\pi}{a\sqrt{3}}y)\cos(\frac{4\pi}{a\sqrt{3}}y)\big)^{1/2}\bigg)\end{aligned} \tag{3.16}$$

for HOPG. The equilibrium is stable in the regions defined by the conditions $\lambda_{1,2}>0$. The stability regions corresponding to the potentials (3.2) and (3.3) are shown in Fig. 3.7 as well. When either $\lambda_1<0$ or $\lambda_2<0$, the stability is lost and the tip suddenly jumps.

The analytical description of the tip movement has been compared to numerical solutions of equation (3.11) at 0 K. In the stability regions, a very good agreement between analytical and numerical results is observed (see Fig. 3.7). When the borders of these regions are reached, the numerical results suggest that the tip follows a straight line until it reaches the next stable position defined by the curves (3.13) or (3.14). Note that numerical simulations of the tip trajectory on graphite have already been shown by Fusco *et al.* [69], however they were not compared to analytical expressions.

Lateral force maps computed for three different ratios of the x- and y- spring constants are shown in Fig. 3.9. The obtained stick-slip patterns all show the expected lattice periodicity, but are qualitatively different. As illustrated in Fig. 3.9(a), if the spring constant in y-direction is lower than the spring constant in x-direction ($k_{\mathrm{x-eff}}>k_{\mathrm{y-eff}}$), stripes appear perpendicular to the scan direction, which are not observed in the experiments [53]. If the spring constant in y-direction is significantly higher than the spring constant in x-direction ($k_{\mathrm{x-eff}}<<k_{\mathrm{y-eff}}$), the friction pattern in each unit cell (see Fig. 3.9(c)) is distinctly different from that observed in the experiment. Only if the spring constants are chosen in the same range ($k_{\mathrm{x-eff}}\approx k_{\mathrm{y-eff}}$, see Fig. 3.9(b)), the rhombus shaped patterns observed on NaCl [53] as well as on KBr [70,71] are reproduced. A similar dependence on the ratio between the spring

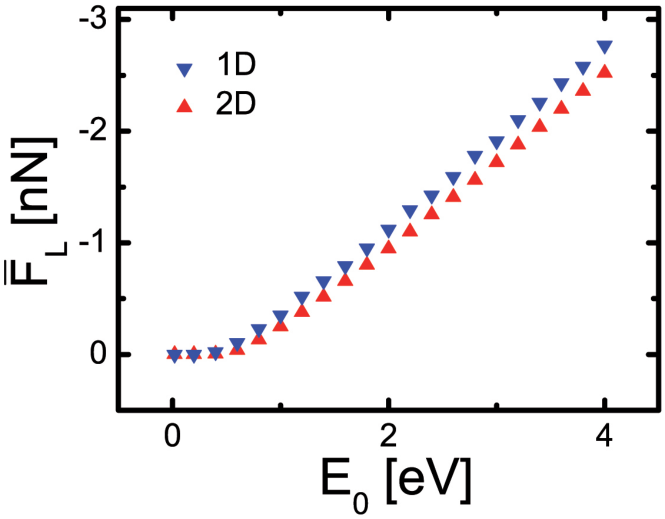

Figure 3.10: Average friction force $\bar{F}_\mathrm{L}$ for NaCl versus amplitude E_0 of the corrugation potential. The amplitude E_0 increases with the externally applied load in the experiment and shows a linear relation to the average friction force $\bar{F}_\mathrm{L}$. However below a critical threshold of E_0, the linear relation goes over into an ultra low friction state where the average friction force $\bar{F}_\mathrm{L} \approx 0$. In two-dimensions the tip avoids passing the maximum of the corrugation potential, which leads to a zig-zag movement and thus the average friction force $\bar{F}_\mathrm{L}$ is lowered compared to a one-dimensional simulation.

constants for the x- and y-direction is found in the case of HOPG, as demonstrated in earlier atomistic simulations [72].

The conclusion is that the effective spring constants k_eff for the x- and the y-direction are in the same range. As shown above, the lateral spring constants k_lateral for both directions are also in the same range. This implies that the contact stiffness is isotropic ($k_{\mathrm{x-contact}} \approx k_{\mathrm{y-contact}}$). This result might be expected for a symmetric tip, but it was not demonstrated before, last but not least because the relevant parameters cannot be measured with a conventional FFM. Another important conclusion is that the lateral force patterns hitherto observed on cleaved alkali halides cannot be satisfactorily explained by a one-dimensional Prandtl-Tomlinson model.

The maximum absolute value of the lateral force is proportional to the amplitude E_0 of the corrugation potential [42] and can therefore be experimentally determined from maps like those shown in Fig. 3.9. The amplitude E_0 depends on the mean tip-sample distance, which can in turn be controlled by the applied load in actual experiments. A linear dependence has been found between E_0 and the mean normal force in experiments on NaCl [42] and HOPG [73] in a limited ”soft contact” range, where no wear or plastic deformation occur. The average friction force $\bar{F}_\mathrm{L}$ is calculated over a reduced scan area, so that the longer initial stick component of each scan line is removed, because it does not contribute to the average friction force corresponding to periodic stick-slip events. A linear dependence of the average friction force $\bar{F_\mathrm{L}}$ on the amplitude E_0 is only obtained at relatively high values of E_0, as shown in Fig. 3.10. When E_0 falls below a critical threshold, the system enters into an ultra low friction regime, where the average friction force practically vanishes ($\bar{F_\mathrm{L}} \approx 0$). Both features, the linear dependence of the average friction force at high loads and the appearance of an ultra low friction state at loads below a critical threshold, were observed on NaCl in UHV [42]. In the experiment, friction could not be detected in the ultra low friction regime because of an insufficient signal-to-noise ratio. In the simulation the average friction force $\bar{F_\mathrm{L}}$ is not equal to zero, but is in the piconewton range. This value is consistent with the assumed parameters, i.e.

$$\bar{F_\mathrm{L}} = -m\gamma v = -0.7 \text{ pN}. \tag{3.17}$$

Finite damping always implies a net energy loss. However, the jump instabilities, which give the dominant contribution to the observed dissipation under stick-slip conditions, disappear in the superlubricity regime.

A comparision was performed to a one-dimensional simulation along a line with maximal corrugation. Fig. 3.10 indicates that the absolute value of the average friction force $\bar{F_\mathrm{L}}$ is lowered in two-dimensions, because the tip avoids passing the maxima of the corrugation potential due to a zig-zag movement [55, 72]. A noticeable consequence is that the one-dimensional Prandtl-Tomlinson model parameters extracted from fits to scan lines showing maximum lateral force variations actually describe the potential profile along the corresponding zig-zag path rather than along the scan line per se.

By increasing the temperature the probability for the tip to jump into an allowed adjacent minima is enhanced [15, 45]. This leads to an earlier jump of the tip compared to lower temperatures, even though the energy barrier between the two minima remains finite. Above a critical temperature T_critical the thermally activated jumps thus reduce the average friction force. Below the critical temperature T_critical, the average friction force approaches $\bar{F_\mathrm{L}} = -m\gamma v$, and falls below the detection limit in the experiments. Due to the thermal effect that causes the reduction of friction, this kind of superlubricity has been called thermolubricity [74]. In Fig. 3.11 the computed average friction force $\bar{F_\mathrm{L}}$ is plotted for NaCl as a function of temperature for different E_0. The reduction of friction shows a non-linear dependence on the temperature. According to activation rate theory [15, 63, 75], the absolute value of the average friction force $\bar{F_\mathrm{L}}$ deviates from its maximum value $|\bar{F_\mathrm{c}}|$ at $T = 0$, with a correction of the form [15]

$$\bar{F_\mathrm{c}} - \bar{F_\mathrm{L}} \propto T^{2/3} ln^{2/3}\left(\frac{cT}{v}\right), \tag{3.18}$$

where T is the temperature and c is a constant depending on other parameters. Below a critical temperature T_critical, which is proportional to the potential amplitude E_0, the analytical formula is in good agreement with the calculation (see fits in Fig. 3.11). Note that at ambient pressure NaCl has a melting temperature of 1074 K, which is far below the upper limit of 2000 K in the simulation. Atomic scale friction on NaCl close to the melting temperature was also explored by Zykova-Timan *et al.* [76] by molecular dynamics simulations at high scan velocity of 50 m/s. Nevertheless, the model is not restricted to NaCl, but is also applicable to other substrates

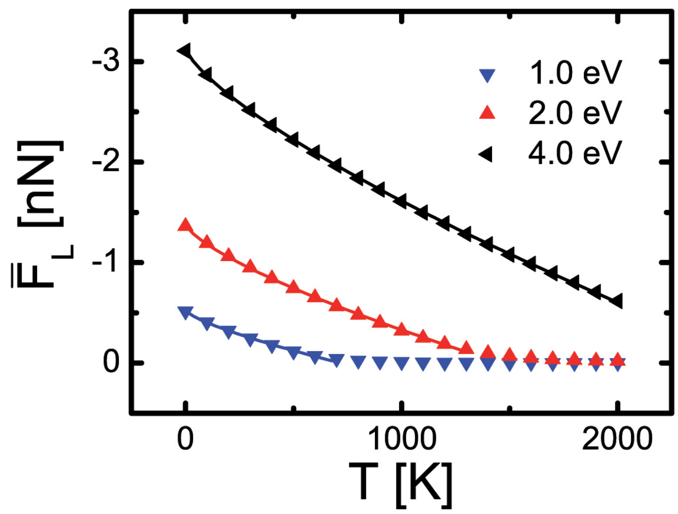

Figure 3.11: Temperature dependence of the average friction force $\bar{F}_{\mathrm{L}}$ for NaCl for different corrugation amplitudes E_0. Above a critical temperature T_{critical}, which depends on E_0, the system passes into the thermolubricity regime, where the average friction force $\bar{F}_{\mathrm{L}} \approx 0$. The activation rate theory is in good agreement at lower temperatures (fitting curves) but cannot be applied to the thermolubricity regime, where the average friction force nearly vanishes.

which have much higher melting temperatures. For instance HOPG, which has a melting temperature of 3400 K, reveals the same dependence on the temperature. Even though the temperature only influences the tip movement in this model, the thermal activation of the substrate should also be considered. The velocity dependence [15] of the average friction force $\bar{F}_{\mathrm{L}}$ is not systematically investigated in this section, but is essential for the discussion of thermolubricity [58, 74, 77]. The following simulations are performed at room temperature in order to satisfy the conditions of most experiments.

An efficient way to ”switch” friction on and off at the atomic scale is achieved by exciting mechanical resonances of the sliding system perpendicular to the contact plane. This was demonstrated on several surfaces as NaCl [43,53], KBr [43], mica [53] and HOPG [53]. When the cantilever is excited in the normal direction, while the tip is still in contact with the surface, the distance between the tip and the sample slightly oscillates. The fundamental assumption is that the corrugation potential E_0 oscillates with the frequency of actuation. Therefore the energy barrier between adjacent minima in the potential energy landscape is also oscillating. The momentary lowering of the energy barrier allows the tip to move earlier to the adjacent minima compared to the case without actuation. Thus the atomic stick-slip curve can evolve into smooth sliding over the surface. As in the original simulation [43], the corrugation amplitude E_0 in equation (3.2) and (3.3) is replaced by a time dependent amplitude $E(t)$

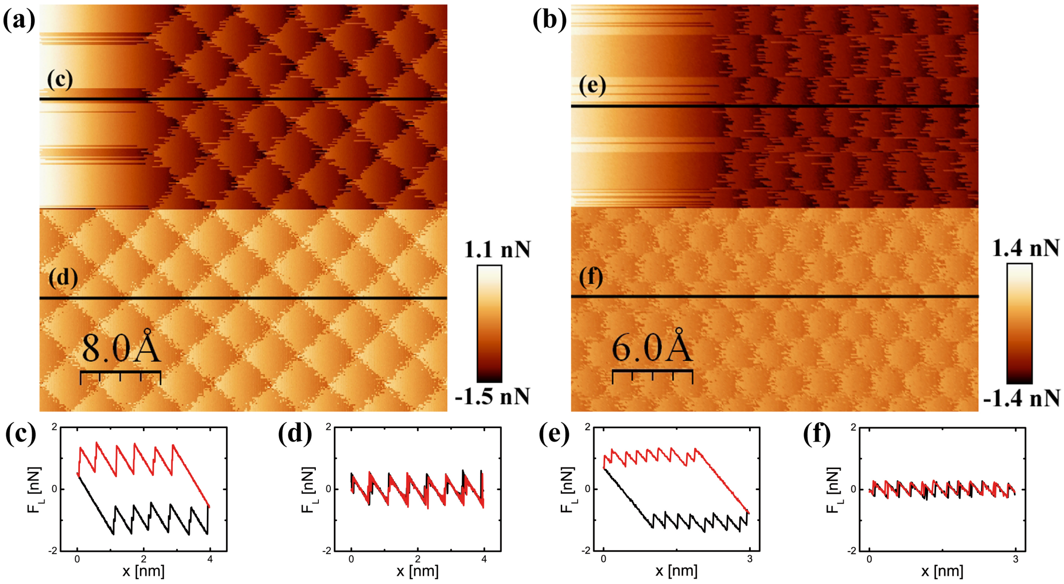

Figure 3.12: (a) Calculated lateral force map on NaCl using $E_0 = 2$ eV (forward scan direction). In the upper part of the image is $\alpha = 0$, whereas in the lower part actuation with $\alpha = 0.9$ is switched on. Typical line scans (black: forward, red: backward) on NaCl, (c) without actuation showing a friction loop, (d) with actuation showing no hysteresis. (b),(e) and (f) are the analog lateral force map, line scan profiles without and with actuation for HOPG using $E_0 = 1$ eV.

$$E(t) = E_0(1 + \alpha cos(2\pi f t + \phi)). \tag{3.19}$$

The parameter α is assumed to be proportional to the strength of actuation amplitude in the experiment. Thus $\alpha = 0$ corresponds to the quasi-static case without actuation and $\alpha = 1$ to the maximum theoretically allowed actuation. The actuation frequency f corresponds to the flexural resonance frequency in contact in the experiment, but in the simulation an actuation frequency of $f = 2000$ Hz is used to keep reasonable computation times. The inertia and damping of the nanotip have a small effect in the adiabatic limit, where the forces acting on the tip are in balance at almost every instant. This leads to the following criteria [43]: $f_{\text{tip}} >> f$ and $f\Gamma << 4\pi f_{\text{tip}}^2$, where $f_{\text{tip}} = \sqrt{k/m}/(2\pi)$ is the resonance frequency of the tip and $\Gamma = \gamma/m$ is the damping rate of the tip. The additional criterion $f >> v/a$ ensures that the tip experiences the minimum corrugation many times within a lattice constant. A change in the actuation frequency f leads to a change in the number of minimum corrugations experienced by the tip within a lattice constant, but as long as the abovementioned conditions are fullfilled, there is little influence on the main result. Furthermore, as long as the actuation frequency f is not a multiple of the so-called washboard frequency v/a, the phase shift ϕ has no influence, which is the case in the simulation.

The effect of the time-dependent corrugation potential amplitude on the tip motion is illustrated for NaCl and HOPG in Fig. 3.13. In this case, the expressions for the

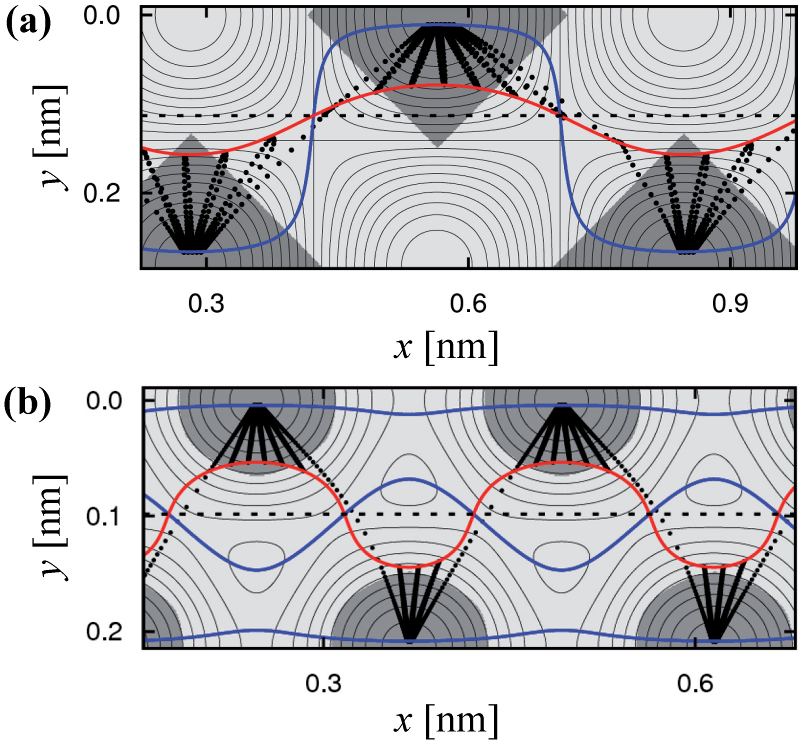

Figure 3.13: Tip paths at $T = 0$ K on (a) NaCl with $E_0 = 1$ eV and (b) HOPG with $E_0 = 0.5$ eV in the case of actuation with $\alpha = 0.9$. The support paths with (a) $y_{\mathrm{sup}} = 0.2\, a$ and (b) $y_{\mathrm{sup}} = 0.4\, a$ are indicated as dashed lines. The stability regions for E_0^+ are mapped dark grey, while the corresponding stability regions for E_0^- cover the whole image (light grey). Analytic tip trajectories for the extreme cases E_0^+ are plotted as blue lines, for E_0^- as red lines, respectively. Between these lines, the numerically calculated tip path (black dots) spatially oscillates and thus jumps are supressed. For visualization reasons, the actuation frequency is lowered to $f = 500$ Hz.

tip trajectories (equation (3.13) and (3.14)) and eigenvalues (equation (3.15) and (3.16)) have to be modified by replacing E_0 with $E(t)$. For visualization purposes, only the extreme values $E_0^+ = E_0(1+\alpha\,)$ and $E_0^- = E_0(1-\alpha\,)$ are considered. As in the one-dimensional case [42], dynamic superlubricity is reached as soon as $2\, E_0^- \pi^2/ka^2 < 1$. In this case, the stability regions cover periodically the entire potential energy surface, allowing the tip to enter the stability region of an adjacent minima. Hence, the non-adiabatic jumps of the tip are suppressed and thus also the energy dissipation. The oscillating potential energy surface leads to a spatial oscillation of the tip path, which is envelopped by the curves $\partial V(E_0^+)/\partial y = 0$ and $\partial V(E_0^-)/\partial y = 0$. If finite temperature effects are taken into account, these well defined tip paths get delocalized by thermal fluctuations. For sake of simplicity only the tip paths at $T = 0$ K are shown in Fig. 3.13.

Several simulations have been performed with different actuation amplitudes α and corrugation amplitudes E_0. To reveal the differing features of the simulations with

and without actuation, it is appropriate to switch on and off the actuation while generating an image. In Fig. 3.12 the results for NaCl and HOPG are presented. $E_0 = 2$ eV for NaCl and $E_0 = 1$ eV for HOPG are assumed and actuation with $\alpha = 0.9$ is switched on in the lower half of the image. The number of pixels in both direction is set to 300, which is comparable to experiments, where typically 256 ×256 pixels are recorded. An increase in the number of pixels has no influence on the main result, apart from increasing the computation time. The line scan in the forward direction (black) and backward direction (red) without actuation (upper half) exhibits the well-known stick-slip behaviour that also causes a hysteresis loop (Fig. 3.12(c,e)). The enclosed area of this hysteresis loop is equal to the energy that is lost during one scan cycle due to friction. Beyond the line where actuation is switched on, the profile changes dramatically. Instead of stick-slip, the lateral force indicates continuous sliding on the surface. The forward and backward line scans are overlapping and thus the hysteresis loop disappears (Fig. 3.12(d,f)). This suppression of friction and of the associated energy dissipation is in agreement with the experiments, and can be called dynamic superlubricity. Furthermore the results show that the more realistic two-dimensional Prandtl-Tomlinson model can account for the observed effects.
Next, the effect of varying actuation amplitude between $\alpha = 0$ and $\alpha = 1$ is analysed for several corrugation amplitudes E_0. The average friction force $\bar{F_\mathrm{L}}$ shows a linear dependence on the actuation strength (see Fig. 3.14) until α approaches a critical value α_critical, where the system enters into the superlubricity regime. This behaviour resembles the temperature dependence, where the system enters into the thermolubricity regime above a critical temperature T_critical. The value of α_critical strongly depends on the corrugation potential amplitude E_0. A smaller corrugation amplitude E_0, that can be adjusted by the load in the experiment, requires a weaker actuation to enter the superlubricity regime. In the extreme case of $\alpha_\mathrm{critical} = 0$, the system is already in the superlubricity regime even without actuation. In this case, the dynamic superlubricity state is superposed by the static superlubricity state, because the corrugation amplitude E_0 is below the critical threshold. In addition thermally activated jumps of the tip occur and reduce the average friction force at room temperature. This situation is presented in Fig. 3.14 for NaCl with a corrugation amplitude $E_0 = 0.5$ eV.

In conclusion, three different types of ultra low friction regimes are analysed numerically with an extended two-dimensional Prandtl-Tomlinson model. First, the load dependence of friction reveals an ultra low friction regime when the normal load acting on the tip decreases below a critical threshold, as shown experimentally by Socoliuc *et al.* [42]. The characteristic stick-slip motion is suppressed and sliding occurs smoothly and without abrupt jumps. This type of friction regime is often referred to static superlubricity. Second, the temperature dependence predicts an ultra low friction regime when the temperature reaches a critical temperature. In that case, thermally activated jumps of the tip occur. The development of the sticking part is prevented by an early jump to the adjacent minima. This type of friction reduction is called thermolubricity [74] but was not shown experimentally up to now. Third, an externally applied actuation of the system facilitates the reduction of friction. For instance, an actuation of the cantilever in normal direction at the contact resonance frequency leads to an ultra low friction regime, as shown

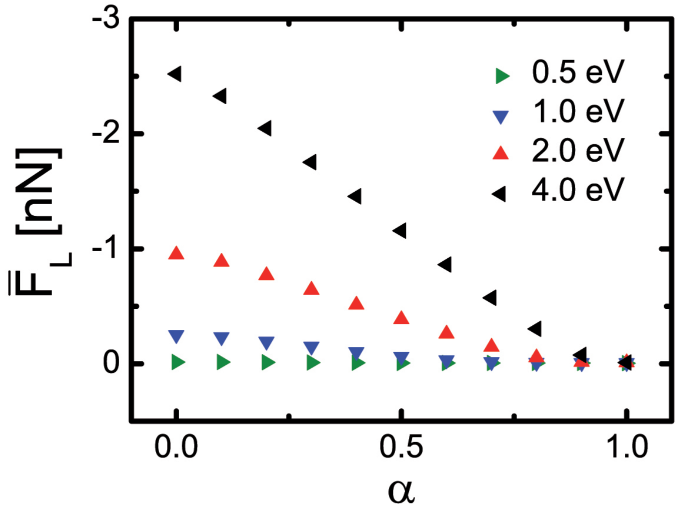

Figure 3.14: Average friction forces $\bar{F}_{\mathrm{L}}$ for three different corrugation amplitudes E_0 on NaCl as a function of normalised actuation amplitude α. For larger corrugation amplitudes E_0, a stronger actuation is required to enter the superlubricity regime. For sufficiently small corrugation potential amplitudes ($E_0 = 0.5$ eV), the system is already in the superlubricity regime independent of actuation.

by Socoliuc *et al.* [43, 53]. Because an externally applied actuation is required, this type of ultra low friction regime is referred to dynamic superlubricity. In all three cases, the simulation reveals that the average friction forces are not equal to zero in the ultra low friction regime, but they are found to be in the piconewton range. Hence they are below the experimental detection limit of the FFM.

These new calculations are capable of describing the ultra low friction regimes originated from different mechanisms of friction reduction, and are in good agreement with the experiments. The recently introduced mechanism of dynamic superlubricity has been discussed in details. The calculations have shown how the tip trajectories, which are analytically and numerically estimated in the model cases of NaCl and HOPG, are modified by the external actuation. Here the tip oscillations smooth the jumps between adjacent minima, ”opening the gate” to the superlubricity regime. Compared to the one-dimensional models presented so far, all three effects of friction reduction appear slightly enhanced in two-dimensions. This result is important, since it allows extending the one-dimensional formalism with only minor modifications. Future theoretical and experimental investigations should clarify how this picture is modified when larger and multiple contact areas, formed by more realistic adjoining surfaces, are taken into consideration.

3.5 Extension of the Numerical Model to Superstructures

In this section, recent friction measurements on ordered superstructures performed by atomic force microscopy are reviewed. In particular, ultrathin KBr films on NaCl(001) and Cu(111) surfaces, single and bilayer graphene on SiC(0001), and the herringbone reconstruction of Au(111) are considered. Atomically resolved friction images of these systems show periodic features spanning across several unit cells. Although the physical mechanisms responsible for the formation of these superstructures are quite different, the experimental results can be interpreted within the same phenomenological framework. A comparison between experiments and modelling shows that, in the cases of KBr films on NaCl(001) and of graphene films, the tip-surface interaction is well-described by a potential with the periodicity of the substrate which is modulated or, respectively, superimposed with a potential with the symmetry of the superstructure.

Atomic force microscopy (AFM) is an invaluable technique to investigate friction forces on the nanometer scale [26]. When the probing tip of an AFM slides on a flat crystal surface in a clean environment such as an ultra-high vacuum, and the tip is sufficiently sharp, stick-slip motion across the unit cells of the sample can be easily observed [50]. Atomic stick-slip appears in time as a sawtooth signal reflecting the torsional deformation of the cantilever holding the tip. The periodicity of the stick-slip pattern usually corresponds to the unit cell of the surface lattice, although tip jumps of a few lattice constants can be detected [33, 78]. The cantilever torsion can be readily quantified if the AFM is equipped with a four-quadrant photodector. In such a case, the instrument can be operated as a friction force microscope (FFM). It is important to note that atomic stick-slip can be recognised also with blunt tips or even when sample material is worn off and transferred to the tip apex [79]. The only requirement in such cases is that a commensurable contact between tip and surface is established. This can be achieved via a reorganization of the atomic layers transferred from sample to tip [80] or via sudden rotations of flakes picked up from the substrate in the case of layered materials [52]. If a commensurate contact is not formed, a regime of ultralow friction, so-called "structural lubricity", may be observed [37,81]. Ultralow friction can also be experienced with sharp tips, provided that the normal load is reduced below a certain "superlubric" threshold [42, 82].

Topography and friction maps of atomically flat crystal surfaces are necessarily convoluted with the atomic structure of the tip apex. This makes the resolution limits of AFM in contact mode quite difficult to determine, and friction imaging a complex process to model. A better understanding could be gained by imaging atomic-scale impurities or nanostructures. However, although atomic defects can be revealed in non-contact AFM (NC-AFM) [83], and even in contact when mechanical resonances are tracked [84], this is usually not the case in lateral force images of flat surfaces. Larger structures formed by annealing or irradiating materials like alkali halides are neither good candidates to test the ultimate resolution of FFM, since step edges and corner sites are prone to be worn off, due to the lower coordination of the atoms at these sites [85]. More stable patterns, eventually formed by different materials, are desirable. In this context, quite interesting structures can be realised by the heteroepitaxial growth of thin films. For instance, it is well-established that Moiré patterns can be observed by STM on ultrathin alkali halide films on metal single crystals [86, 87]. Superstructures can also be observed when a thin film is grown on a reconstructed surface. This is the case of graphene on SiC, as also demonstrated by STM [88–90]. However, whether the superstructure observed by STM has an influence on mechanical properties like friction on the adsorbate films cannot be revealed by STM alone.

The goal of this section is to discuss recent studies that demonstrated the observation of ordered superstructures on atomically flat substrates by FFM and revealed tribological properties of these structures down to the atomic scale. In particular, attention is focussed on thin alkali halide films deposited on single crystals of another alkali halide or a metal surface, on graphene overlayers formed on SiC(0001), and on the herringbone reconstruction of Au(111).

Experimental results are reproduced modelling the tip-surface interaction with phenomenological potentials, which extend the classical Prandtl-Tomlinson model used to interpret friction on atomically flat surfaces [48, 49] to the superstructures. The importance of these studies goes beyond understanding the mechanisms and testing the resolution limits of FFM. The investigation of the KBr/NaCl(001) system, for instance, clearly revealed how both the periodicity of the overlayers and the superperiodicity of the "buried" KBr/NaCl interface have a comparable influence on the motion of the tip sliding on the top of the composite system.

One should mention that atomically ordered superstructures were observed by AFM also on other systems without friction maps. In the past decade hexagonal superstructures were discerned in intercalation compounds of the layered $MnPS_3$ and associated to protruding sulfur atoms [91]. Incommensurate superstructures were recognised on insulating layered material and attributed to a phase transition in the perovskite structure of the crystal [92], and also on conducting surfaces, where they were related to charged density waves [93].

Since the lattice constants of NaCl (0.564 nm) and KBr (0.660 nm) are almost in a ratio 6:7, a significant rearrangement of the ions at the interface is expected when one of the two alkali halides is deposited on the second one. Recent NC-AFM studies pointed out important differences between NaCl/KBr(001) and the "reciprocal" system, i.e. KBr/NaCl(001) [95]. In the first case the ionic bonds are allowed a considerable relaxation and the overlayer stretches over the substrate to match its lattice structure. This is not the case when KBr is deposited on NaCl, and a "rumpling" of the interface is energetically preferred to a compression of the K-Br bonds. The latter effect can be easily understood observing that ions with the same sign overlap with a periodicity of 7 NaCl lattice constants so that the Coulomb repulsion increases the corrugation of the interface at the locations of these ions. The deformation of the interface will also affect the growth of KBr thin films up to a few monolayers, as suggested by Monte Carlo simulations [96]. While a single KBr layer could not be recognised in NC-AFM measurements, the rumpling was observed on 2 and 3 monolayer thick islands. The ions in the KBr top layer organised in a square superstructure whose unit cell covered 7×7 unit cells of the substrate. The apparent corrugation of the superstructure in NC-AFM topographies was about 0.12 nm on 2 monolayer and 0.11 nm on 3 monolayer thick islands [95]. The rumpling effect has been recently recognised also in topographies acquired in contact mode (not shown), and clear evidence of atomic stick-slip was given by the

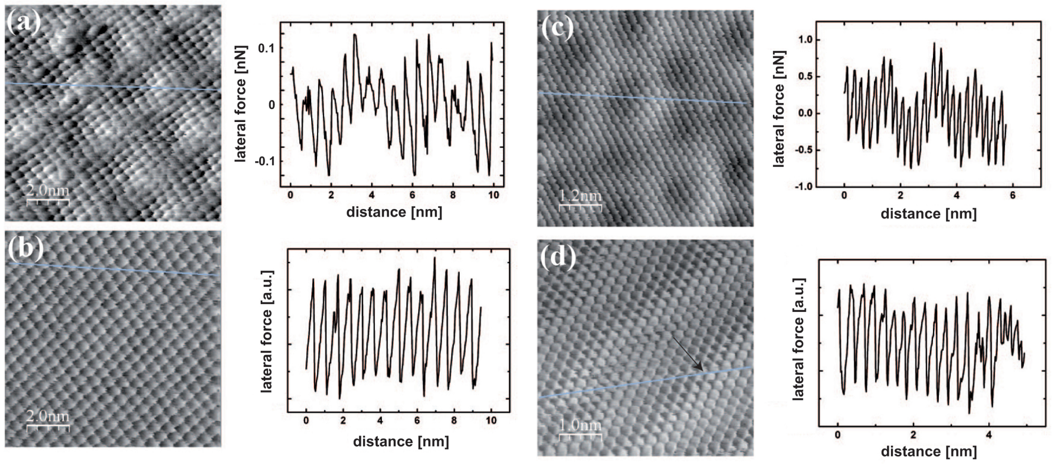

Figure 3.15: Friction force maps experimentally acquired on (a) KBr/NaCl(001) (adapted from [94]), (b) KBr/Cu(111), (c) Graphene/SiC(0001), and (d) the herringbone reconstruction of Au(111). Ordered superstructures can be recognised in all systems. Cross sections taken along one of the principal crystallographic directions of the substrates are shown on the right side of the images.

corresponding friction maps (Fig. 3.15(a)). Compared to the regular stick-slip on bulk-truncated KBr(001) surfaces, the stick-slip ampitude on 2 ML KBr/NaCl(001) is modulated with the periodicity of the superstructure and the offset oscillates with the same period.

The modulation of the friction force is reduced on 3 ML films, where the KBr/NaCl interface has clearly less influence. If the normal load is lowered below a certain threshold (close to the cantilever jump-off) regular stick-slip is observed. In the section profiles in Fig. 3.15(a) a slight variation of the slope can be also recognised. This slope is essentially associated with the lateral stiffness of the contact region [42], so that the question arises whether this quantity, rather than the tip-surface interaction, is more influenced by the superstructure.

In the case of KBr growing on Cu(111) the ratio between Cu (0.361 nm) and KBr lattice constants is slightly larger than 6 :11 , which also results in the formation of regular superstructures. Since a rumpling effect caused by the repulsion of similar ionic species is excluded, the structuring will be essentially caused by the compression of K-Br bonds. The presence of a square pattern with a periodicity of 3.96 nm was revealed in NC-AFM topographies on 2 , 3 and 4 monolayer thick films [38]. A slight corrugation of about 30 pm was also measured, which is in the same range of the atomic corrugation of the lattice. Friction force images acquired on the same system also show a very weak spatial modulation (Fig. 3.15(b)). The values of the friction force and lateral contact stiffness recorded on the KBr film are in the same range of bulk-truncated KBr(001) surfaces.

The presence of a 6 × 6 superstructure on 1 monolayer and 2 monolayer thick graphene films grown on SiC(0001) using thermal decomposition under atmospheric pressure was recently revealed by NC-AFM [97]. This superstructure of graphene is

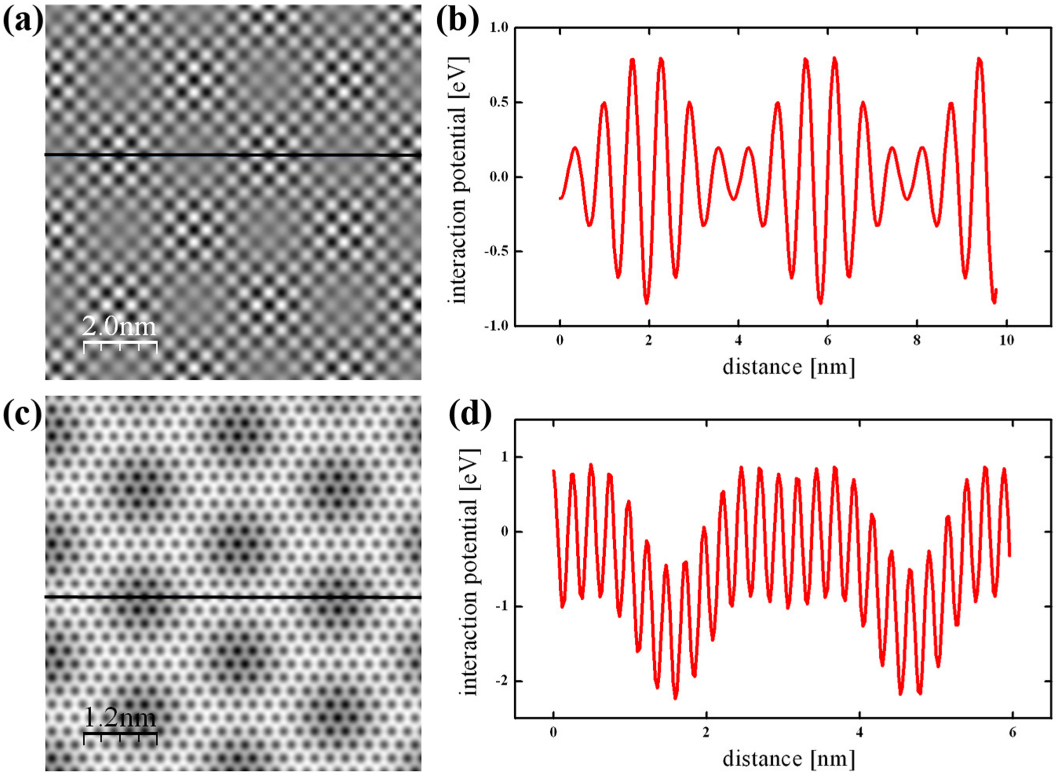

Figure 3.16: Tip-surface interaction potentials corresponding (a) to the expression (3.20) and (b) to the expression (3.22) introduced in the text. The parameters α and β are both set equal to 0.7 . In (b) the superpotential V_{sup} is rotated by 30° with respect to the normal potential V_{lat}.

following the 6 × 6 reconstruction of the substrate surface, a carbon-rich interface layer which develops in the thermal decomposition process. Atomically resolved friction maps show that the superstructure also appears as a modulation in the lateral force (Fig. 3.15(c)). However, compared to the films formed by KBr on NaCl(001) and Cu(111), a remarkable difference can be noticed. Whereas KBr films show an amplitude modulation of the friction force, the graphene layers present a periodic variation in the offset of the stick-slip pattern. Furthermore, the superstructure is maintained in the superlubric regime, which sets on at relatively high loads (around 40 nN).

Finally, recent FFM measurements are presented on the well-known herringbone reconstruction of the Au(111) surface [98]. Fig. 3.15(d) shows a lateral force map acquired at low load (in the nN range) on a flat area of this surface. The signature of the herringbone reconstruction is given by periodic shifts in the atomic rows, one of which is highlighted by the section. These shifts reflect a change of stacking across the surface, which does not allow extracting the modulation of stick-slip as it was done for the superstructures presented so far. On reconstructed Au(111) the average value of the friction force remained below the noise level for normal loads up to 3.8 nN [99]. Above this value, friction suddenly increased and wear set on.

Atomic friction on flat surfaces is well-interpreted by the Prandtl-Tominson model

[48,49] (or by its extension known as Frenkel-Kontorova-Tomlinson model in the case of extended contact areas [100]). In the Tomlinson model the probing tip is approximated by a point mass m which is laterally driven by an elastic spring (with spring constant k) across a potential $V(x, y)$, describing the chemical interaction between the tip apex and the surface lattice. Here, this model is extended to the ordered superstructures discussed above. The most striking observation in the experimental results is the different response of KBr films on NaCl(001) and graphene. On KBr films both amplitude and offset of stick-slip are modulated, whereas on graphene only the offset of the stick-slip oscillates with the periodicity of the superstructure. Both behaviors can be well-reproduced if the tip-surface interaction potential $V(x, y)$ is written as a combination of two potentials: $V_{\text{lat}}(x, y)$, with the periodicity of the top layer, and $V_{\text{sup}}(x, y)$, with the periodicity of the superstructure. If one limits the analysis to the first Fourier components of V and V_{sup}, these potentials can both be written as superpositions of two (for square symmetries) or three plain waves (for hexagonal symmetries) $e^{i\mathbf{k}\cdot\mathbf{r}}$, where the wave vector $\mathbf{k}$ and the radius $\mathbf{r}$ are oriented parallel to the substrate surface. These waves are tilted with respect to one another by 90° in the case of KBr films and by 60° in the case of graphene. Introducing the spatial periodicity a of the atomic lattice and the periodicity b of the superstructure, the wave numbers for the potentials V_{lat} and V_{sup} are $2\pi/a$ and $2\pi/b$, respectively. Good agreement with the experimental results is found when introducing the following assumptions.

(a) In the case of KBr/NaCl(001) the amplitude of the potential V_{lat} is assumed to be modulated by the "superpotential" V_{sup}

$$V(x, y) = V_{\text{lat}} \left(1 + \alpha \frac{2V_{\text{sup}}}{E_0}\right), \tag{3.20}$$

where E_0 is the corrugation amplitude of the potential V_{lat} and the parameter α gives the strength of the modulation effect. Since the substrate has a square symmetry, the potential V_{lat} can be written in the form

$$V_{\text{lat}}(x, y) = -\frac{E_0}{2} \cos\frac{2\pi x}{a} \cos\frac{2\pi y}{a}. \tag{3.21}$$

The potential V_{sup} has also the form Eq. (3.21), with the lattice constant a replaced by the period b of the superstructure. The interaction potential (3.20) is shown in Fig. 3.16(a).

(b) In the case of graphene, the experimental results are better reproduced by a superposition of two potentials V_{lat} and V_{sup}:

$$V(x, y) = V_{\text{lat}} + \beta \widehat{R} V_{\text{sup}}, \tag{3.22}$$

where the parameter β gives the ratio between the amplitudes of the superperiodic potential V_{sup} and the atomic potential V_{lat} and the operator $\widehat{R}$ describes a possible rotation of the coordinate system. Due to the hexagonal symmetry of the system, the potential V_{lat} takes now the form

$$V_{\text{lat}}(x, y) = -\frac{E_0}{4.5} \left(2\cos\frac{2\pi x}{a} \cos\frac{2\pi y}{a\sqrt{3}} + \cos\frac{4\pi y}{a\sqrt{3}}\right), \tag{3.23}$$

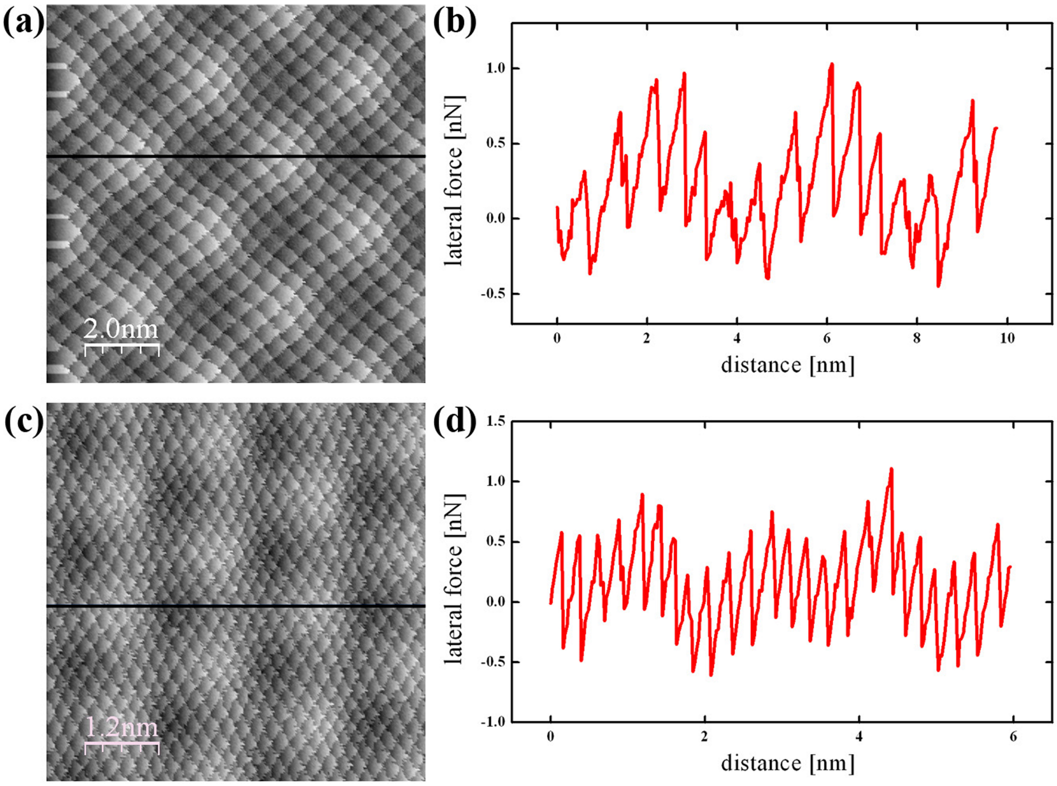

Figure 3.17: Simulated friction maps corresponding to the potentials in Fig. 3.16. The values of scan speed, tip mass, and damping coefficient are $v =$ 25 nm/s, $m = 10^{-12}$ kg and $\gamma = 10\gamma_{\mathrm{cr}}$, respectively.

and similarly V_{sup} (with the length a replaced by b). Fig. 3.16(b) shows a possible interaction potential $V(x, y)$ with the form of Eq. (3.22).

The equations of motion of the tip, with its support moving at a speed v in the x-direction, have consequently been solved in the two cases (a) and (b). Since the experiments were performed at room temperature, a noise term is introduced satisfying the fluctuation-dissipation theorem, and a damping term $-m\gamma(v_{\mathrm{x}}, v_{\mathrm{y}})$, as usual in this kind of calculations [32]. The latter term guarantees the occurrence of atomic stick-slip provided that the parameters k, m and γ satisfy the relation $\gamma \gg \gamma_{\mathrm{cr}} = 2\sqrt{k/m}$, i.e. that the oscillations of the tip, immediately after jumping, are overdamped [101]. Fig. 3.17 shows numerical results obtained using the assumptions (a) and (b) respectively. In this figure, the lateral force $F_{\mathrm{x}} = k(vt - x)$, as recorded along the fast scan direction, is mapped as a function of the support coordinates, as in the experiments. A satisfying agreement with the experimental data was obtained using the values (a) $E_0 = 1$ eV, $k = 2$ N/m, and $\alpha = 0.7$ for the KBr film and (b) $E_0 = 2$ eV, $k = 4.7$ N/m, and $\beta = 0.7$ for graphene. In the last case, the AFM data could be matched only after rotating the potential V_{sup} by 30° with respect to V_{lat}. Note that the rotation by 30° between the graphene lattice and the 6×6 reconstruction was observed using STM and LEED [88].

With the choice of potential Eq. (3.20) the tip-surface interaction is implicitly assumed to enhance in the troughs of the superstructure. When the load is lowered or

α decreases this effect is reduced till the interaction gets confined within the unit cell of the superstructure when $\alpha = 0$. Another possibility is that the lateral stiffness rather than the interaction potential is spatially modulated. However, calculations performed under this hypothesis (shown in the 1D case [94]) are inconsistent with the experimental observations. This result gives a strong indication the KBr/NaCl interface plays an important role in determining the frictional response on the top layer. On the other side, it is difficult to rationalise the good matching between the assumption (b) and the frictional maps acquired on graphene. One can only postulate that the modulated offset of the lateral force originates from the fact that the substrate surface undergoes a significant reconstruction during the growth of the graphene film. The much smaller modulated offset which is observed for KBr on NaCl(001) in addition to the amplitude modulation is well reproduced in the simulations in Fig. 3.17(b) based on the model potential (3.20). The simulations were repeated for various parameters and found that in general a modulation of the lateral force amplitude occurs only for model potential of type (3.20), i.e. with a modulated amplitude of the atomic potential. In conclusion, there is a fundamental difference between the effective lateral potentials on the KBr and the graphene films. While for the KBr films the amplitude of the lateral atomic potential is modulated by the superstructure, it is not modulated but periodically offset in the case of graphene. The origin of this difference is not clear at this time, and explanation will probably require a simulation with realistic atomic potentials.

The reproduction of the frictional response of the reconstructed Au(111) surface is not attempted by periodically shifting the atomic rows. Here, one can only suggest that the tilt in the lateral force curve in Fig. 3.15(d) is caused by the facetting of the Au(111) surface due to the herringbone reconstruction. Furthermore, it is likely to emphasise the details of the structure resolved in Fig. 3.15(d). As shown by the arrow, the shift in the herringbone reconstruction can be localised within the spatial limit of a lattice constant. Similarly, Fig. 3.15(a) shows stable defects at well-defined atomic locations. Since these defects differ in both shape and size, they are not simply mirroring the atomic arrangement at the tip apex. This gives an answer to the question about the resolution limits of FFM which was stated above. Friction force microscopy is shown here to approach atomic resolution, provided that the probing tip is very sharp and one operates at very low loads close to the superlubric regime [42]. There are indeed indications that the corrugation of the superstructure as observed in lateral force maps becomes smaller (and defects disappear) using blunter tips.

In conclusion, four recent examples of frictional imaging on atomically ordered superstructures are discussed. Two of them (KBr on NaCl(001) and graphene on SiC(0001)) could be well reproduced invoking the Prandtl-Tomlinson model and using appropriate combinations of two periodic potentials to describe the tip-surface interaction. The amplitude of the atomic potential is modulated by the superstructure in the case of KBr films on NaCl(001), whereas the two potentials are superimposed and rotated in the case of graphene films. The form of the first potential is traced back to the rumpling of the buried KBr/NaCl interface, whereas more detailed theoretical investigations should clarify the physical mechanisms responsible for the shape of the second potential. The friction maps presented in this section also demonstrate the atomic scale resolution capabilities of FFM.

Frictional investigations on superstructures may be extended beyond the few examples discussed in this section. A regular arrangement of ion impurities resulting in the so-called Suzuki phase was recently recognised by Barth and Henry on alkali halide surfaces [102]. Another noticeable system are boron nitride nanomeshes, whose structure seems to be quite resistant to external sollicitations [103]. Quasicrystals are also attracting considerable interest in nanotribology [104] and it would be quite intriguing although challenging to determine whether superstructures can be grown on them and resolved by friction force microscopy.

3.6 Multiple Slips in Atomic-Scale Friction

The occurrence of multiple jumps in 2D atomic-scale friction measurements is used to quantify the viscous damping accompanying the stick-slip motion of a sharp tip in contact with a NaCl(001) surface. Multiple slips are observed without apparent wear for normal forces between 13 nN and 91 nN. For scans parallel to [100] directions, the tip jumps between minima of the substrate corrugation potential in a zig-zag fashion. An algorithm is applied to determine histograms of lateral force jumps which characterize multiple slips. The same algorithm is used to classify multiple slips occurring in calculated lateral force maps. Comparisons between simulations and experiments indicate that the nanometer-sized contact is underdamped at intermediate loads (13 nN - 26 nN) and becomes slightly overdamped at higher loads. The proposed procedure is a novel way to estimate the lateral contact damping which plays an important role in the interpretation of measurements of the velocity and temperature dependence of friction, of slip duration, and of the reduction of friction by applied perpendicular or parallel oscillations.

Since the invention of the friction force microscope (FFM) [7], stickslip movement was found to be characteristic for a sharp tip at the end of a cantilever which is moved perpendicular to its axis in soft contact with an atomically flat surface. Since the periodicity of the observed sawtooth-like lateral force pattern often corresponds to the spacing between adjacent unit cells, such experimental observations were readily associated with atomic stickslip motion, where the tip slips between energetically favored neighboring lattice sites [7, 105]. Each slip is accompanied by a jump in the lateral force F_{L} at the corresponding position x_{s} of the cantilever support.

The 1D Prandtl-Tomlinson model [48, 49] has often been used to interpret such atomic-scale friction phenomena. A particle representing the tip is dragged by an elastic spring of stiffness k_{eff} connected to a support moving at a constant velocity v over a sinusoidal potential of peak-to-peak amplitude E_0 and period a representing the surface. Note that k_{eff} accounts for the combined torsion of the cantilever and the contact shear. In contrast to earlier assumptions [101], recent atomic-scale FFM measurements on alkali halide surfaces at loads in the few nN range have shown that $k_{\mathrm{eff}} \approx 1$ N/m is typically dominated by the lateral contact stiffness, so that the entities which are most deflected during each stick stage are the contacting atoms at the tip apex and at the sample surface rather than the cantilever [42, 106]. Atoms further away are also deflected sideways, albeit less because more atoms take up the stresses generated in the contact region. The net shear displacements in that region, in opposite directions at the apex and at the surface, can in principle exceed

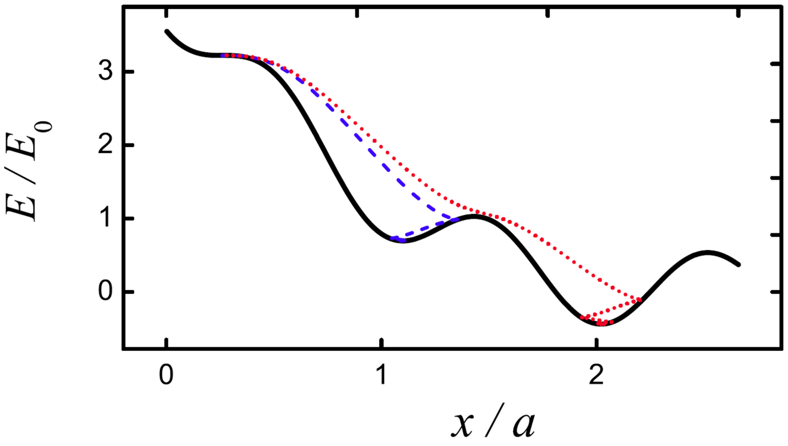

Figure 3.18: Variation of the total energy E during a slip event versus the instantaneous tip coordinate x (in units of the corrugation amplitude E_0 and the lattice constant a) calculated for two values of the damping ratio: $\gamma/\gamma_c = 1$ (dashed blue curve) and $\gamma/\gamma_c = 0.8$ (dotted red curve). The potential energy U (solid black line) at the onset of the slip is shown for comparison. For the assumed value $\eta = 12.8$, slips of up to 4 a are in principle allowed [78], but only a and 2 a slips are realised in the two illustrated cases.

several lattice spacings but still remain elastic. During each slip, the energy stored in the preceding stick stage is released and carried away from the contact. In the wearless regime realized at low loads, the stressed atoms return to their respective equilibrium positions on time scales which are long compared to typical periods of lattice vibrations, but almost instantaneously compared to the time required to scan over a surface unit cell. Actually, FFM experiments suggest that transfer of the softer material initially occurs until a regular stickslip pattern is observed. This is confirmed by simulations on ionic crystals which show that the tip apex then adopts a "self-limited structure" at a given load [80]. As long as this structure remains relatively sharp, the tip deforms more than the sample, hence contributes more to the slip distance and to the accompanying energy dissipation. Asserting that the tip slips, as is often done for the sake of exposition, therefore also has a physical basis. Within the Prandtl-Tomlinson model, slips over more than one lattice spacing a can in principle occur for a sufficiently strong corrugation amplitude E_0 and/or a sufficiently low k_{eff}. In the quasi-static limit, the number of minima in the total potential energy determines the possible landing points of the tip after a slip. The Prandtl-Tomlinson parameter $\eta = 2^2 E_0/k_{\text{eff}} a^2$ can distinguish regimes where the tip is sliding smoothly ($\eta < 1$), executes stickslip motion with single slips ($1 < \eta < 4.6$) or, possibly exhibits double slips ($4.6 < \eta < 7.79$) or even bigger multiple slips ($\eta > 7.79$). Whereas a few authors focused attention on the occurrence of single versus double slips as a function of additional parameters (contact damping, support velocity, temperature) [107–109], Medyanik *et al.* [78] derived the abovementioned η threshold values from a simple analytic criterion. Most studies, however, assumed that the tip slips to the adjacent available energy minimum once the current min-

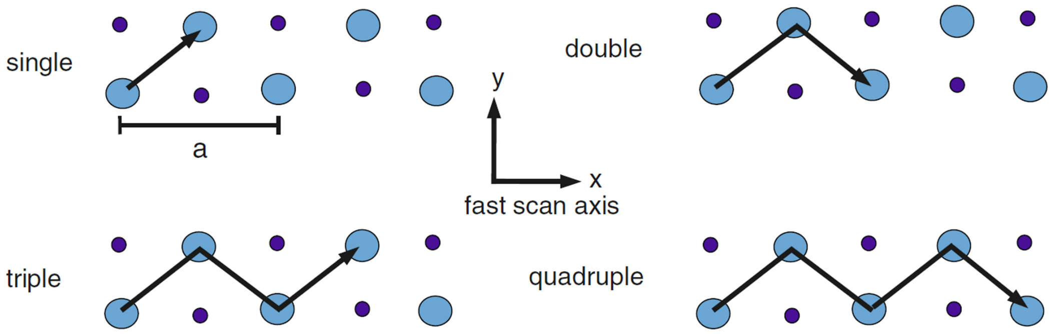

Figure 3.19: Schematic illustration of the path of the tip while scanning along the [100] direction of a rocksalt (001) surface. The tip jumps from one minima to the next one in a zig-zag fashion in steps of $a/2$, which is the distance between two consecutive minima of the 2D corrugation potential projected on the scan direction. Whether the Na^+- or the Cl^--sublattice correspond to the potential minima depends on the unknown nature and structure of the tip apex [71]

imum disappears as the support is slowly pulled past a critical position x_{sc} (mod a). This is justified if lateral contact vibrations are overdamped, owing to coupling to substrate (and/or tip) excitations, so that the energy released in each jump is dissipated quicker than the tip would cross a lattice spacing in the absence of damping. This inelastic coupling increases with decreasing tip-sample distance, just as for atoms or molecules adsorbed with different bond strengths on a clean surface [110]. One therefore expects the contact damping to increase with applied load, at least for dry friction of sub-nanometersized single-asperity contacts. Effects due to interface incommensurability, roughness, defects, or adsorbed species, which are especially relevant in wider area contacts [106, 111] are then likely not so important. Recent FFM measurements on graphite showed transitions from single to double and to triple slips with increasing load, in agreement with the abovementioned threshold η values [78]. This is qualitatively in accordance with the near independence of k_{eff} and the linear dependence of E_0 on the applied load previously measured on NaCl(001) in ultra-high vacuum (UHV) [42]. However, it is by no means obvious whether the increase in η with load should dominate over the expected increase in γ, as seems required to explain the transitions in question.

In dynamic extensions of the Tomlinson model [101, 107, 108, 112], an effective tip or contact mass m and damping coefficient γ are introduced in the equation of motion for the tip in contact, thus making the prediction of multiple slips more realistic. Since some fraction of the tip kinetic energy is lost during each jump due to non-zero damping, not all energy minima can be reached. Thus, the number of possible slips calculated from η alone must be considered as an upper limit which may be achieved in the strongly underdamped case. In the opposite case, multiple jumps become suppressed, as mentioned earlier. Thus, the occurrence of multiple slips and the lateral contact damping are intimately connected. This study provides a novel way to estimate γ relative to a critical value which distinguishes overdamped from

underdamped contacts. The lateral contact damping plays an important role in the interpretation of FFM measurements of the velocity and temperature dependence of friction [63, 75], of slip duration [113], and of the reduction of friction by applied perpendicular [32, 43] or parallel oscillations [44].
Direct estimates of γ have so far been obtained in a few situations where a viscous contribution to the average friction proportional to the support velocity could be detected. Thus, Bilas *et al.* [114] found $\gamma \approx 10^{-5}$ kg/s $\sim 5\,\gamma_c$ for an FFM tip scanning on $NbSe_2$ in air by comparing measured velocity-dependent friction curves with simulated ones. The damping was attributed to viscous drag by adsorbed water. At low scan velocities and loads, regular single slips were observed, consistent with overdamping. Yabing *et al.* [115] estimated $\gamma \approx 5 \times 10^{-6}$ kg/s for a voltage-dependent contribution to the friction of oxidized highly n-doped GaAs forward-biased by means of a platinum-coated tip in UHV conditions. They associated the small excess friction with electric coupling to slowly relaxing trapped charges in the oxide. Reinstädtler *et al.* [116] obtained $\gamma \approx 10^{-6}$ kg/s from the measured quality factor in air of the torsional resonance of a cantilever in contact with an oxidized silicon sample driven by ultrasonic shear waves under ambient conditions. The contact was described by a lateral stiffness and damping coefficient, but zero inertial mass.
In all those cases, the contacts had estimated radii of several nanometers and therefore encompassed many atoms. The measured load dependence of the average friction, assumed proportional to the contact area was well described by continuum elasticity models. The proportionality constant (shear strength) roughly plays the same role as the slope of E_0 versus load, although no site-dependent corrugation potential enters such models. Their applicability has recently been questioned on the basis of large-scale atomistic simulations [111] which reveal that multiple contacts are formed and broken even for nominal contact radii of several nanometers.
An absolute determination of contact damping from atomically resolved FFM measurements appears impossible because scan velocities are orders of magnitude lower than those required to directly detect the viscous friction force $-\gamma v$. The interpretation of such measurements relies on uncertain assumptions about the contact mass or the angular frequency $\omega_x = \sqrt{k_{\text{eff}}/m}$ of lateral contact vibrations, the damping rate $\Gamma = \gamma/m$ or the ratio Γ/Γ_c, $\Gamma_c = 2\omega_x$ being the critical damping rate. In particular, identifying m with the mass of the whole tip, ω_x with the torsional resonances frequency of the cantilever in contact or Γ with the full width at half-maximum of the corresponding spectral peak is unfortunately not justified for atomic-scale contacts [113].

In order to illustrate how damped dynamics determines the landing point of the tip, in Fig. 3.18 the potential profile $U(x)$ (surface corrugation + energy stored in the spring) at the onset of a slip is displayed together with the variation of the tip (kinetic + potential) energy during the slip event for two values of the relative damping γ/γ_c. For the sake of simplicity, the calculations are performed within the 1D Prandtl-Tomlinson model without thermal activation.
During the preceding stick stage, the tip is located in a potential minimum satisfying the mechanical equilibrium condition $dU/dx = 0$. This adiabatic approximation holds as long as the support velocity v is low so that slips occur much faster than the time to move over one lattice spacing a. The slip is initiated at the tip position

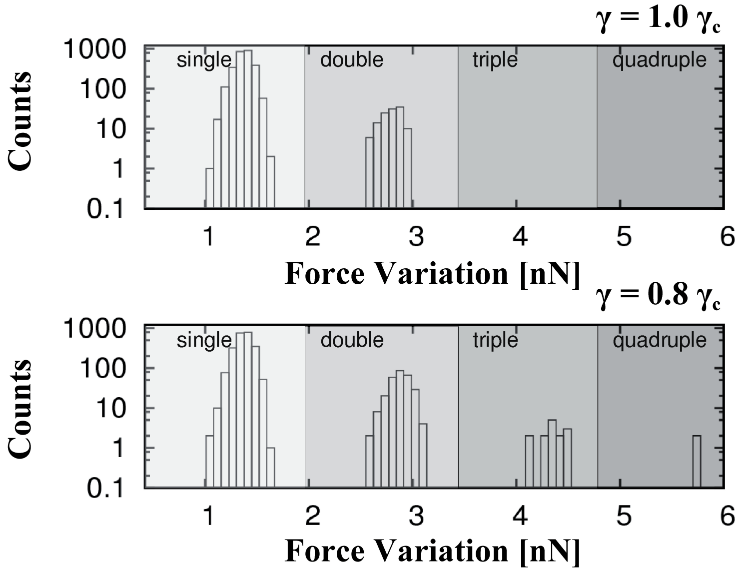

Figure 3.20: Room temperature histograms of force jumps calculated for $\eta = 12.8$ for two representative values of the relative damping. The upper histogram shows the distribution for $\gamma = 1.0\,\gamma_c$ where only single and double slips are identified. The lower histogram is the result of a simulation with $\gamma = 0.8\ \gamma_c$ where triple and quadruple slips are manifested.

x_c where in addition the equilibrium becomes unstable, i.e. $d^2U/dx^2 = 0$. For the chosen value $\eta = 12.8$, the instability occurs at $x_c/a = 0.2645$ when the support is at $x_{sc}/a = 2.2934$. In both cases shown, the tip executes oscillations, i.e. its dynamics is underdamped in the potential well where it is trapped. A particular well is selected if the energy reduced by damping during the initial tip swing drops below the nearest blocking potential maximum. The damping range allowing double slips and the corresponding values for larger multiple slips are therefore determined by the overall potential landscape. Nevertheless, referring those values to the critical damping $\gamma_c = 2\sqrt{k_{\text{eff}} m}$ defined by the oscillation frequency of the harmonic spring potential is justified not only by computational convenience, but also by the physics of the problem. Indeed, multiple slips can only occur for relatively high values of η. On the one hand, the spring extension just before a slip is then $(x_{sc} - x_c) \approx \pi E_0/(k_{\text{eff}} a)$ [42], and contributes almost exclusively to the stored potential energy. On the other hand, the potential energy after completion of a slip to the lowest well (around $x = x_{sc}$) is nearly $-E_0/2$. Therefore, the energy released and dissipated during such a slip is approximately

$$\Delta E_{\max} \sim \frac{k_{\text{eff}}(x_{sc} - x_c)^2}{2} + \frac{E_0}{2} = \left(\frac{\eta}{2} + 1\right)\frac{E_0}{2}, \tag{3.24}$$

hence is dominated by the first, harmonic spring term. For $\eta = 12.8$, Eq. (3.24) predicts $\Delta E_{\max} = 3.7E_0$, which is remarkably close to the calculated value for the double slip illustrated in Fig. 3.18. In accordance with this conclusion, this figure, and similar plots for other values of γ/γ_c (data not shown), illustrates that during most of the "slip time", the modulation of the total potential by the surface corru-

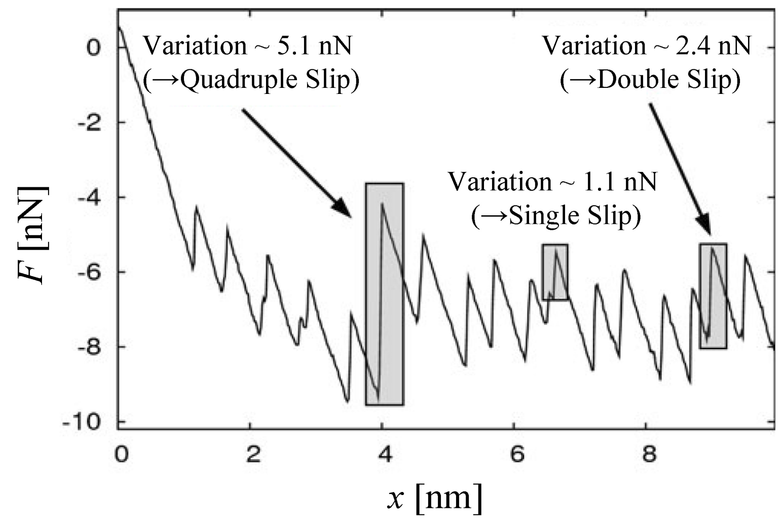

Figure 3.21: Experimental lateral force trace taken at 91 nN normal load showing different types of jumps within one scan line.

gation has a relatively small influence on the "total energy trajectory" which ends up in the lowest well. Thus, although for large η the curvatures at the minima of the corrugation potential are higher than k_{eff}, the critical damping for the energetically most favorable slips is largely determined by k_{eff}. Note finally that at a finite temperature slips can be prematurely activated over the energy barrier which vanishes when $x_{\mathrm{s}} = x_{\mathrm{sc}}$ [45, 63, 75]. As a consequence of the underlying probability distribution of initial tip positions and velocities, slips of different lengths can randomly occur along single scan lines around the abovementioned η threshold values in the underdamped case. This has been observed in previous simulations [107–109] and experiments [78], as well as in this section (see Fig. 3.21).

In this section, room temperature lateral force measurements are presented and analysed, that were performed over a NaCl(001) substrate in UHV for a wider range of applied loads than hitherto studied [42]. As shown in that study, the amplitude of the tip-sample corrugation potential is a linear function of the applied load. One can therefore control the parameter η, which can in turn be experimentally determined from $\eta = 2\pi F_{\mathrm{L}}^{\max}/(k_{\exp} a) - 1$, where $F_{\mathrm{L}}^{\max}$ is the maximal lateral force experienced by the tip, $a = 0.564$ nm is the lattice constant of NaCl, $k_{\exp}$ is the slope of the stick part of the lateral force versus support displacement, itself connected to the effective stiffness via $k_{\mathrm{eff}} = \frac{\eta+1}{\eta} k_{\exp}$ [42, 106].

As illustrated in Fig. 3.19, for scans along $\langle 100 \rangle$ directions parallel to the (001) cleavage surface of rocksalt-type crystals, previous FFM simulations in two dimensions [32, 112], as well as those discussed below, show that the tip slips over saddle points connecting adjacent minima of the corrugation potential, at least for η values not close to 1 . As a consequence, the double and quadruple slips illustrated in Fig. 3.19 correspond to the single and double slips discussed above. A sorting algorithm was applied to both experimental and computed lateral force data in order to classify slip events according to the magnitude ΔF_{L} of particular jumps and thus to distinguish among single, double, triple, or quadruple slips. The dynamic

2D Prandtl-Tomlinson model used to interpret the experimental room temperature data is based on coupled Langevin equations for the x and y tip coordinates, namely

$$m\frac{d^2x}{dt^2} + \gamma\frac{dx}{dt} + \frac{\partial U_{\mathrm{int}}(x,y)}{\partial x} = \zeta(t), \tag{3.25}$$

and similarly for y, where m is the effective mass of the tip in contact, γ its lateral damping coefficient, and $\zeta(t)$ a stochastic term proportional to γ according to the fluctuationdissipation theorem [63, 75]. In accordance with the discussion of Eq. (3.24), critical damping is defined by $\gamma_{\mathrm{c}} = 2\sqrt{k_{\mathrm{eff}} m_{\mathrm{tip}}}$. Referring γ to γ_{c} makes the analysis independent of the effective mass, which is not accurately known. For computational convenience, the mass of the tip apex is set to $m = 10^{-12}$ kg. This choice enables efficient computations on a computer with a time step which allows a fine sampling of the fast tip motion during slips.

The interaction potential $U_{\mathrm{int}}(x,y)$ is represented by the lowest Fourier component of the rocksalt lattice for the corrugation part and by an isotropic harmonic spring term, as recently justified by a comparison of calculated and measured lateral force maps on the same system [32]

$$U_{\mathrm{int}}(x,y) = -\frac{E_0}{2}\left[\cos\left(\frac{2\pi}{a}x\right)\cos\left(\frac{2\pi}{a}y\right)\right] + \frac{1}{2}k_{\mathrm{eff}}(x - x_{\mathrm{s}})^2, \tag{3.26}$$

where $x_{\mathrm{s}} = vt$ the position of the support uniformly scanned along a [100] scan line specified by y. These coupled equations were solved numerically using the Ermak algorithm [65]. Two-dimensional lateral force maps were generated [32] using realistic parameters (v, E_0, k_{eff}, T) corresponding to previous measurements on the same system [42]. Simulations were done for a range of damping coefficients on both sides of γ_{c}. By comparing the resulting histograms of ΔF_{L} from experiment and theory, an estimation of $\gamma/\gamma_{\mathrm{c}}$ can be made for different loads, an aspect barely discussed in the literature, although it is quite important in the field of nanotribology.

The (001) surface of an in situ cleaved NaCl crystal was used as the sample. To remove surface charges created during the cleavage process, the crystal was heated up to 100°C for 30 min in UHV. Rectangular silicon cantilevers with spring constants of $k_{\mathrm{norm}} = 0.097$ N/m for normal bending and $k_{\mathrm{T}} = 64$ N/m for torsion were used. Normal loads varying between 13 nN and 91 nN were applied to the cantilever, which was scanned at a velocity of 13 nm/s parallel to the [100] direction of the surface. Above this range, wear processes set in. All normal forces are defined with respect to the unbent cantilever (i.e. without adding adhesion forces).

As in previous 2D simulations of scans along the [100] direction [112], the tip exhibits regular zig-zag slips between adjacent corrugation energy minima in the overdamped case. In the underdamped case, multiple jumps of the type sketched in Fig. 3.19 appeared as η was successively increased, although no sharp threshold values could be identified at room temperature. The force variation during a n-tuple jump is then given by $n \times a/2 \times k_{\mathrm{eff}}$. Note that for all values of $\eta > 1$, double slips occurred when the path of the support is very close to the atomic rows. As abovementioned, they correspond to single slips by a in the 1D Prandtl-Tomlinson model. If the time resolution of the calculated friction maps is rather low, it is not possible to distinguish between two very fast consecutive $a/2$ jumps and a direct jump by a. For a realistic comparison, the same time and spatial resolutions were set in both experiment and

simulations. However, the resulting artifacts do not affect the general conclusions. By adjusting the damping γ in the range of $0.1\,\gamma_\mathrm{c}$ - $10\,\gamma_\mathrm{c}$, an upper limit for the damping can be estimated. For $\eta = 12.8$, the calculated histograms which show the onset of multiple slips are shown in Fig. 3.20. Solutions of Eqs. (3.25,3.26) for fixed x_s (i.e. assuming that support motion during a slip can be neglected) only depend on the dimensionless parameters η, $E_0/k_\mathrm{B}T$, and Γ/ω_x, ω_x being the angular frequency of some characteristic vibration of the model. With the choice $\omega_\mathrm{x} = \sqrt{k_\mathrm{eff}/m}$ and the definition $\Gamma_\mathrm{c} = 2\omega_\mathrm{x}$ appropriate for a damped harmonic oscillator, energetically most favored multiple jumps for a given η appear in distributions like those shown in Fig. 3.20 once γ becomes slightly undercritical. This consequence of the abovementioned discussion provides a simple criterion to estimate the ratio γ/γ_c from jump histograms obtained from FFM measurements.
Fig. 3.21 shows an example of the coexistence of different force jumps ΔF_L in an experimental scan. For the five values of the normal load that have been thoroughly analysed, namely 13 , 26 , 39 , 78 , and 91 nN, the corresponding values of k_eff only varied in the range between 5.2 N/m and 5.9 N/m. *This is consistent with a contact encompassing just a few atoms.* The amplitude E_0 of the corrugation potential was extracted from the measured maximum lateral force $F_\mathrm{L}^\mathrm{max}$ versus load [42] and subsequently increased by 25 % in order to roughly account for thermal activation which lowers the value of $F_\mathrm{L}^\mathrm{max}$ [32, 63, 75]. Experimental histograms of force jumps are shown in Fig. 3.22. For the lowest loads, $\eta = 5.6$ and $\eta = 7.1$, mostly single slips with a small number of double slips occur. For higher loads, triple and quadruple slips could also be identified. Owing to the significant amount of instrumental noise in the experimental data, the histograms do not exhibit separated peaks like in Fig. 3.20, but rather a continuous distribution extending to higher ΔF_L at higher loads.

From a systematic visual comparison of experimental and simulated scans and histograms of ΔF_L, the following conclusions concerning the relative damping can be drawn for the last three plots in Fig. 3.22. When $\eta = 8.2 :\ \gamma < 0.3\,\gamma_\mathrm{c}$, when $\eta = 12.8 :\ \gamma < 1.0\,\gamma_\mathrm{c}$, and when $\eta = 14.5 :\ \gamma < 1.5\,\gamma_\mathrm{c}$. The successive appearance of higher multiple slips with increasing load can therefore be used to quantitatively estimate the ratio γ/γ_c in the range where an atomic-scale contact can be maintained without wear. Recalling that the load dependence of the critical damping γ_c, which in this model only comes from k_eff, is practically negligible, these conclusions imply that the load dependence of the lateral contact damping is weaker than that of the surface corrugation amplitude E_0, at least for the system under study. More generally, the lateral vibrations of an atomic-scale or nanometer-size contact with a clean crystal surface is not necessarily overdamped as often assumed. Upon increasing the load at room temperature, smooth crossovers from an underdamped regime to a critical damped state and finally to a slightly overdamped regime have been observed before wear sets in, previously on cleaved graphite [78], and now on the NaCl(001) surface.
Note finally that no systematic excitation of cantilever oscillations has been observed right after a lateral force jump, although several resonances of the cantilever in contact lie within the 3 MHz cutoff of the recording electronics [113]. This is expected if the effective mass of the contact is orders of magnitudes smaller than the masses of the tip as a whole and of the cantilever [43, 58]. The motion of the contact being

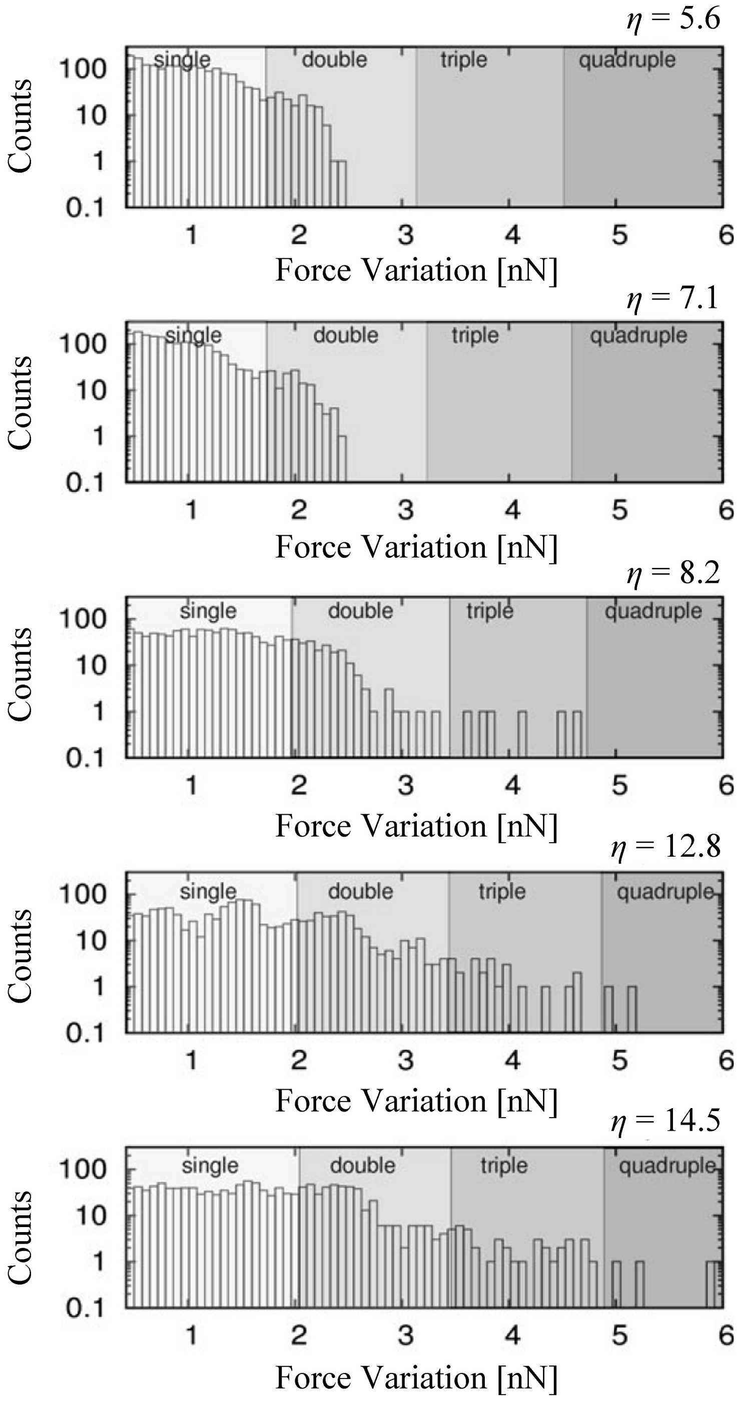

Figure 3.22: From top to bottom: Room temperature histograms of force jumps obtained from measured lateral force maps for increasing loads corresponding to $\eta = 5.6, 7.1, 8.2, 12.8, 14.5$. At the lower loads, only single and double slips could be revealed, whereas at higher loads, genuine multiple slips were identified.

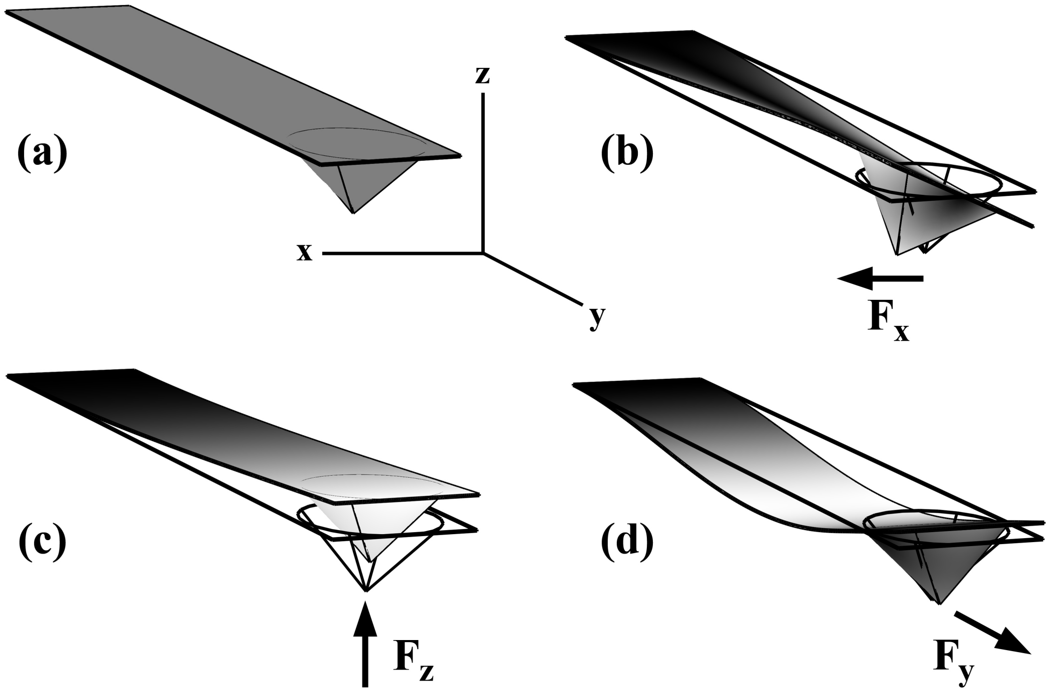

Figure 3.23: (a) Force components which act on the tip apex of the cantilever. F_x, F_y and F_z are defined as the force accross the cantilever (fast scan direction), along the cantilever (slow scan direction) and normal to the cantilever, respectively. (b) F_x causes a torsion of the cantilever due to the displacement in the x-direction and is detected in the horizontal deflection channel. (c) F_z causes the displacement in the z-direction and also a deflection of the cantilever due to the z-direction displacement, and is detected in the vertical deflection channel. (d) F_y causes a deflection of the cantilever due to the y-direction displacement, which is referred to the buckling, but does not induce the z-direction displacement.

much faster than the mechanical resonance modes of the cantilever in contact, no such modes can be effectively excited. Since the signals arising from the bending and torsion of the cantilever are filtered above the 3 MHz cutoff, the actual dynamics of the tip cannot be followed. It can nevertheless manifest itself at temperatures such that thermal activation induces frequent random contact slips over the time scale of cantilever torsional oscillations [58]. It is then necessary to consider the coupled dynamics of the contact and the cantilever [101, 113]. Whether the contact motion is underdamped [117] or overdamped [118] is then also of concern. Because multiple slips occur for relatively large values of η, hence E_0, the dynamics of the cantilever has been neglected in this study.

3.7 Determination of the Tip Trajectory

In FFM measurements, the lateral force is measured as a function of the torque of the cantilever. Beside the torque of the cantilever, there is also a vertical deflection

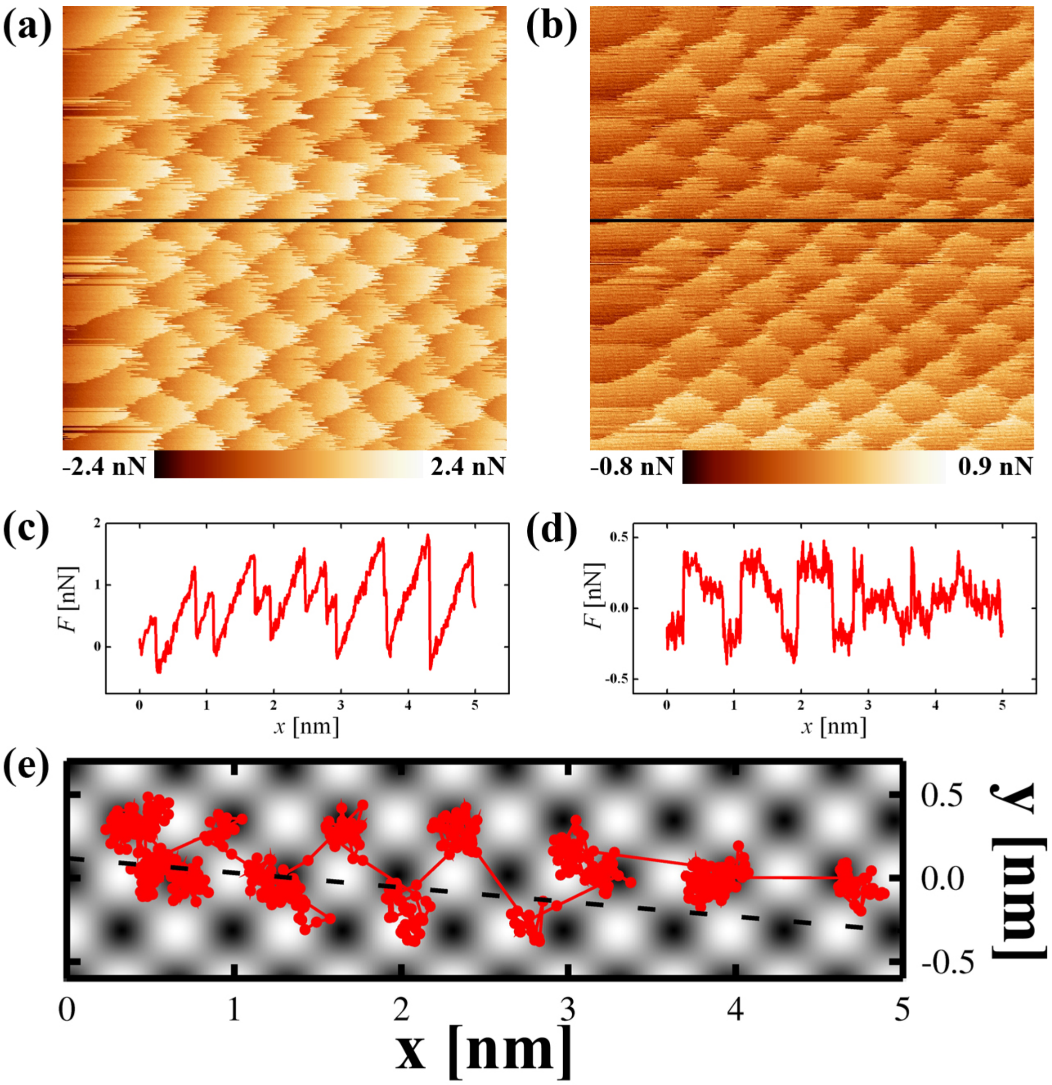

Figure 3.24: (a) Horizontal deflection image measured on KBr deposited on Cu(111) and (b) the vertical deflection image. Profiles for the (c) horizontal deflection and (d) vertical deflection were taken along the fast scan direction from (a,b). Note that the forces in the vertical deflection image were calibrated by adjusting the jumps in the profile to half the lattice constant of KBr (see text). (e) Reconstructed tip trajectory superposed on the calculated surface corrugation potential.

of the cantilever, especially in constant height measurements. Both, the torque and the vertical deflection, not only represent the dynanmics of the cantilever, but also reflect the motion of the tip apex itself. By this means, the motion of the tip apex, i.e. the position of the tip apex as a function of time, may be reconstructed using the horizontal deflection signal and the vertical deflection signal. In this section, a method is presented for the tip trajectory reconstruction based on a conventional FFM measurement.

As usual, the horizontal deflection image needs to be offset corrected, because the laser spot on the four-quadrant diode is not always well centered. The offset is determined by summing up the values of the forward and backward image and dividing by two. The same procedure is repeated for the vertical deflection channel. The lateral forces are then calibrated as described in Section (2.3). The force calibration in the case of the vertical deflection is more complex. A profile of the vertical deflection exhibits regular jumps in direction of the slow-scan direction (see Fig. 3.24(d)). These major jumps are attributed to the buckling of the cantilever [47,119,120] and are adjusted to half of the lattice constant $a = 0.66$ nm for KBr, i.e. $\Delta F_{\text{vertical}}[\text{mV}] \equiv a/2$, and thus converted to nm. The multiplication of the values now in [nm] with the spring constant then results in $F_{\text{vertical}}[\text{nN}]$ as shown in Fig. 3.24(b,d) for the image and profile. Here, the spring constant was assumed to be isotropic, as demonstrated recently by computer simulations [32]. The spring constant $k = 1.8$ N/m determined for the horizontal direction in the usual way is now also applied to tip motion in the slow-scan direction. The position of the tip $\mathbf{r} = (x_{\text{tip}}, y_{\text{tip}})$ as a function of time t can then be determined with

$$\begin{aligned} x_{\text{tip}} &= F_{\text{x}}/k + v_{\text{x}}t \\ y_{\text{tip}} &= F_{\text{y}}/k + y_0, \end{aligned} \tag{3.27}$$

where v_{x} is the cantilever velocity in the fast scan direction, and y_0 is the offset according to a individual line profile in the slow-scan direction. However, the actual offset (x_0, y_0) can not be calculated, but is adjusted arbitrary to fit on the potential minima of the potential, which is underlayered in Fig. 3.24(e). In addition, the path of the support, i.e. the cantilever motion, is added as a dashed line by using the same offset as for the tip trajectory and an angle determined by the lateral force map in Fig. 3.24(a).

In Fig. 3.24(e) the positions of the tip trajectory are connected by red lines, which illustrates nicely the zig-zag path of the tip movement, while the cantilever itself is moving straight along the dashed black line. The underlying surface corrugation potential is calculated using

$$V_{\text{KBr}}(x, y) = -\frac{E_0}{2}\cos(\frac{2\pi}{a}x)\cos(\frac{2\pi}{a}y), \tag{3.28}$$

where the amplitude of the corrugation potential E_0 is of arbitrary units and the maxima correspond to white and the minima to black colour. The positions of the tip apex do not perfectly fit into the minima during the whole scan profile, but most of the time the tip trajectory follows quite well the minima around the cantilever path. The deviations from a perfect path through only minima arise from different

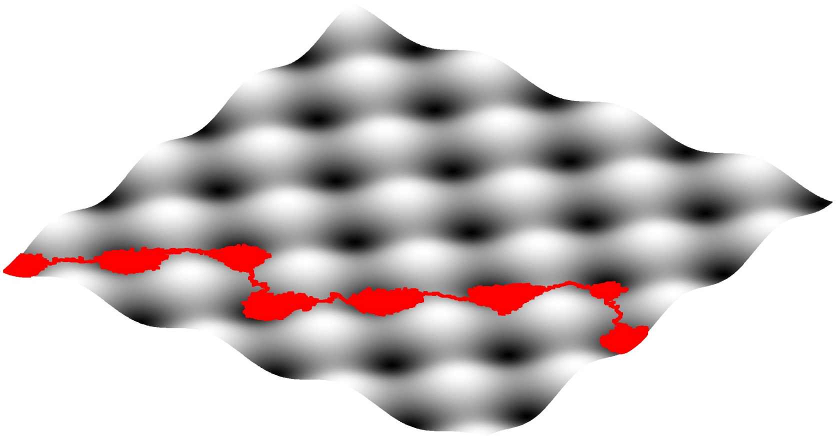

Figure 3.25: Calculated tip trajectory for KBr(001) based on the Prandtl-Tomlinson model at room temperature. The tip always resides in a minima until the pulling force is high enough to induce a jump into an adjacent minima.

effects in the experimet, for instance thermal effects, and the fact that the tip apex does not consist of only one atom.

A computer simulation based on the Prandtl-Tomlinson model using the parameters from the experiment with $\eta = 11.8$ was performed. A typical tip trajectory is illustrated in Fig. 3.25. Here, the tip apex always resides in potential minima and passes minor potential barriers, i.e. a saddle point, when jumping into an adjacent minima. Morita *et al.* [47,60] also investigated the tip trajectory based on experimental data similar to the profiles and images in Fig. 3.24, and combined the images to give a tip position map. However, they did not examine the tip trajectory of one scan profile, but performed model calculations based on the principle of so-called "stick-points". However, the idea of the stick-points is obselete because even at zero temperature it is more a broad region on the corrugation potential surface (*stability region*), where the tip apex is allowed to reside (for more details see Chapter 6). The experimental and numerical results presented here are now focussing on the implicit tip trajectory. The numerical calculation nicely support the experimental determined tip motion of a scan line, even though the experimental tip path reconstruction is not everywhere commensurate with the surface lattice.

A further step could be to combine the tip trajectories of all san lines to give an image of the minima of the surface lattice, similar to the tip position map [60]. This method could give rise to have a better insight into and help to develop a potential energy surface also for more complex systems [121], where analytical and numerical potentials are highly demanded. A better understanding of the tip movement during scaning could also improve the comprehension of damping and energy dissipation on the atomic scale.

3.8 Step Edge on NaCl(001)

Measuring the friction forces acting on a nano-object (such as an atomically sharp tip) sliding across a well-defined obstacle (such as a monoatomic step edge) is quite important for a better understanding of mechanical processes occurring on the nanoscale. A common observation in the few experimental studies on this topic [122–126] is the enhancement of friction at the step edge, which has been attributed to the presence of a Schwöbel barrier [124]. Compared to a flat terrace, where the nanotip performs regular atomic stick-slip across the surface lattice, the higher number of chemical bonds formed at the bottom of step edges increases the magnitude of the lateral force required to detach the tip. In the investigations reported so far, friction was found to increase when the step is crossed either upwards or downwards, although the load dependence of friction is not the same in the two cases [126]. However, the studies reported so far were performed on large length scales (in the micrometer range), with no atomic resolution along the scan direction. This would be quite important to gain further insight into the mechanical properties of tiny objects.

Different AFM tips are to scan cleavage step edges on NaCl(001) surfaces in UHV. When the tip climbs up an edge, the latter always acts as an obstacle, increasing the friction force experienced by the tip. However, when the tip crosses the edge downwards, two different tendencies are observed. Blunt tips are still pinned — and friction consequently increases — at the step edge as before. Atomically sharp tips, in contrast, easily slip into the bottom of the edge, thus experiencing a positive friction force, i.e. a force which is parallel to the direction of motion. These results cannot be simply interpreted within the standard models commonly used to reproduce friction measurements on atomically flat surfaces.

The measurements were performed using a a home-built AFM setup with a base pressure of about 10^{-10} mbar [17]. The NaCl(001) surfaces were cleaved in UHV, annealed at 150 °C to remove surface charges. A commercial cantilever with normal resonance frequency $f_{\mathrm{norm}} = 10.8$ kHz and stiffness $k_{\mathrm{norm}} = 0.117$ N/m was used (Nanosensors, PPP-CONT). The lateral force F_{L} was detected using a four quadrant photodiode, which is sensitive to the cantilever torsion. The method discussed in Ref. [127] was used to calibrate the normal and lateral forces. Apart from static measurements, normal and torsional vibrations of the cantilevers are also excited by means of mechanically coupled piezo-elements. This allows to reduce and even 'tune' friction while scanning [43, 128] and may influence the resolution of the step edge.

Fig. 3.26 (a-b) shows a topography and the corresponding friction image acquired on a 15×15 nm^2 area across a step edge. The normal force was kept constant at the value $F_{\mathrm{norm}} = -0.2$ nN (attractive regime). As shown by the arrow, some kink sites are present along the step. The most noticeable feature is the atomic resolution of the step edge. This is clearly revealed by the profile in Fig. 3.26(c), where the surface height drops of 0.22 nm (slightly less than half lattice constant $a = 0.564$ nm) within 0.28 nm. Furthermore, the change of contrast in both images suggest that the tip apex has a width of two lattice constants in the fast scan direction. Since the measurements were performed after some days of cleaving the NaCl surface, many

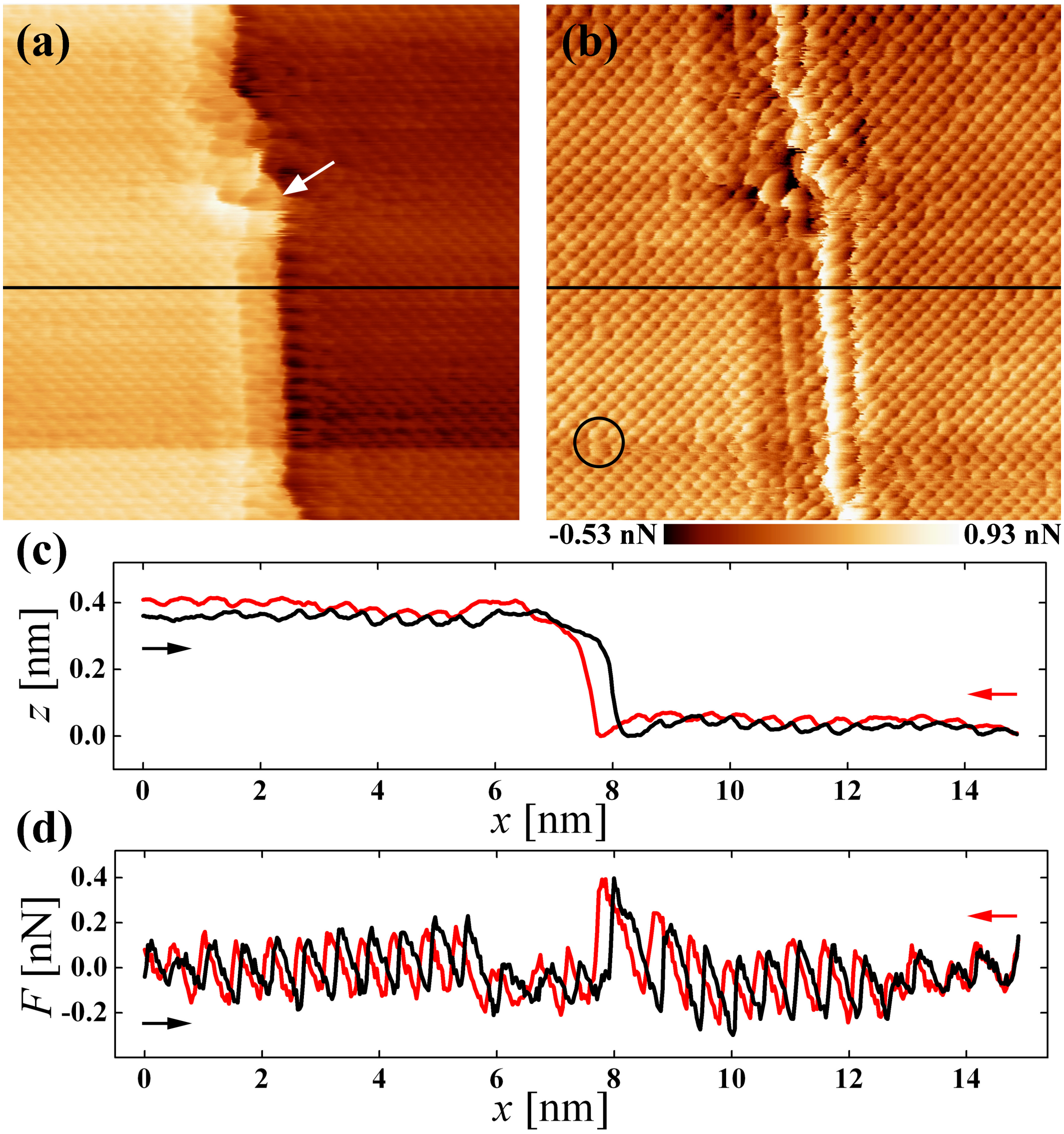

Figure 3.26: a) Topography image and (b) the corresponding lateral force image of 15 × 15 nm^2 acquired on NaCl(001) using a load of -0.2 nN. A few kink sites are indicated in (a) by the white arrow and the circle in (b) points out a defect that the tip size is in the order of twice the lattice constant of NaCl. Profiles are taken along the black line for (c) the topography and (d) lateral force for the forward scan direction (black lines). Red profiles represent the backward scan directions (images not shown).

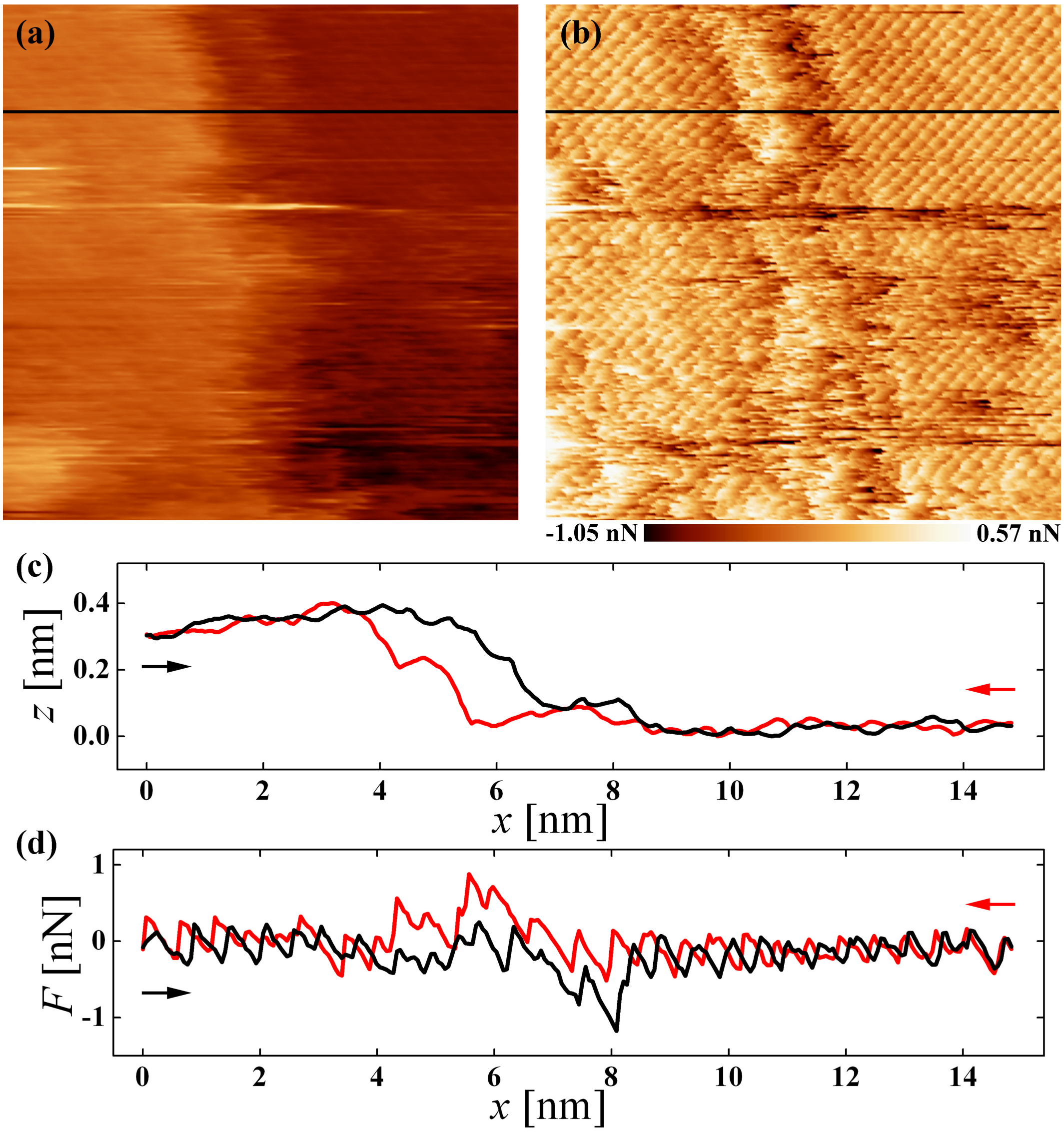

Figure 3.27: (a) Topography and (b) lateral force images using the same sample, cantilever and imaging conditions as in Fig. 3.26. However, after prolonged scanning at high load, the tip sharpness is considerably reduced. Profiles are taken along the black line for (c) the topography and (d) the lateral force (black curves). Red profiles represent the backward scan directions (images not shown). Note that the lateral force is increased at the step edge for both, the step-up direction (black) and the step-down direction (red), which is reflected in the friction loop.

atomic defects are present. As shown by the circle in Fig. 3.26(b), the defects always appear as squares with side length $2a$, meaning that the tip end has a width of at least two lattice constants also in the slow scan direction. The lateral force profiles for the forward and backward scans are overlapping. For the scan in step-up direction (red) the lateral force is increased at the step edge as expected. In contrast to this, the lateral force for the step-down direction (black) exhibits a positive value when crossing the edge, meaning that the tip temporarily overtakes the cantilever. Here, the friction loop is very small, i.e. the measurement is performed in the ultra-low friction regime.

Although the images like those presented in Fig. 3.26 have been reproduced with several cantilevers, they still represent an exception rather than the rule. Fig. 3.27 shows a topography and a friction map across another step edge, acquired with the same tip after repeated scanning with high loads in different regions on the NaCl sample. The horizontal traces clearly indicate the presence of abrasion wear, which contaminates the tip and increases the size of the contact area between tip and surface. The friction profiles in the two directions change also considerably. Friction is now enhanced in both directions when the tip crosses the step edge. Images taken with other blunt tips present similar features. In order to improve the resolution of these images, the normal and torsional resonance of the cantilever were tried to excite while scanning. Although friction is significantly reduced by normal excitations, as in previous experimental work [53], this did not result in better resolution.

Friction on atomically flat terraces is well-explained by the Prandt-Tomlinson (PT) model [129]. Essentially, a point mass representing the tip apex is driven by one or more lateral springs (with effective spring constant k_{eff}) across a periodic energy landscape representing the tip-surface interaction potential. In an attempt to extend the PT model to the step edge, the electrostatic surface potential across the step edge is first calculated (Fig. 3.28(a)), a point mass is placed at a distance $d = 0.4$ nm from the surface (Fig. 3.28(b)) and the lateral force F_{L} is calculated which acts on the tip when it is laterally driven by a spring (Fig. 3.28(c)). However, a qualitative agreement with the experimental results is only observed when the tip climbs up the step edge (Fig. 3.28(c), black line). In the opposite direction, the friction reduction was enabled by introduceing additional hypotheses. For instance, if the feedback gain is too low, the separation between tip and surface will increase, leading to a decrease in friction. This is shown by the red line in Fig. 3.28(c), corresponding to the tip pathway described by the red curve in Fig. 3.28(b). Despite of that, it was not possible to reverse the sign of the lateral force, as in the experiment. This strongly suggest that in presence of step edges the PT model with a single-atom tip is too naive.

An alternatie approach to the electrostatically calculated potential is the heuristic Prandtl-Tomlinson approach using modified potentials for the step-up and step-down directions. The tip-surface interaction potential is assumed to increase for the tip apex hitting the step edge from the direction of the lower terrace, and to decrease for the tip apex moving downwards from the direction of the higher terrace, which is described by the one-dimensional corrugation potential

$$V_{\pm}(x) = C \cos\big(\frac{2\pi}{a}x\big)\big[1 \pm A e^{-\frac{(x-D)^2}{2B^2}}\big], \tag{3.29}$$

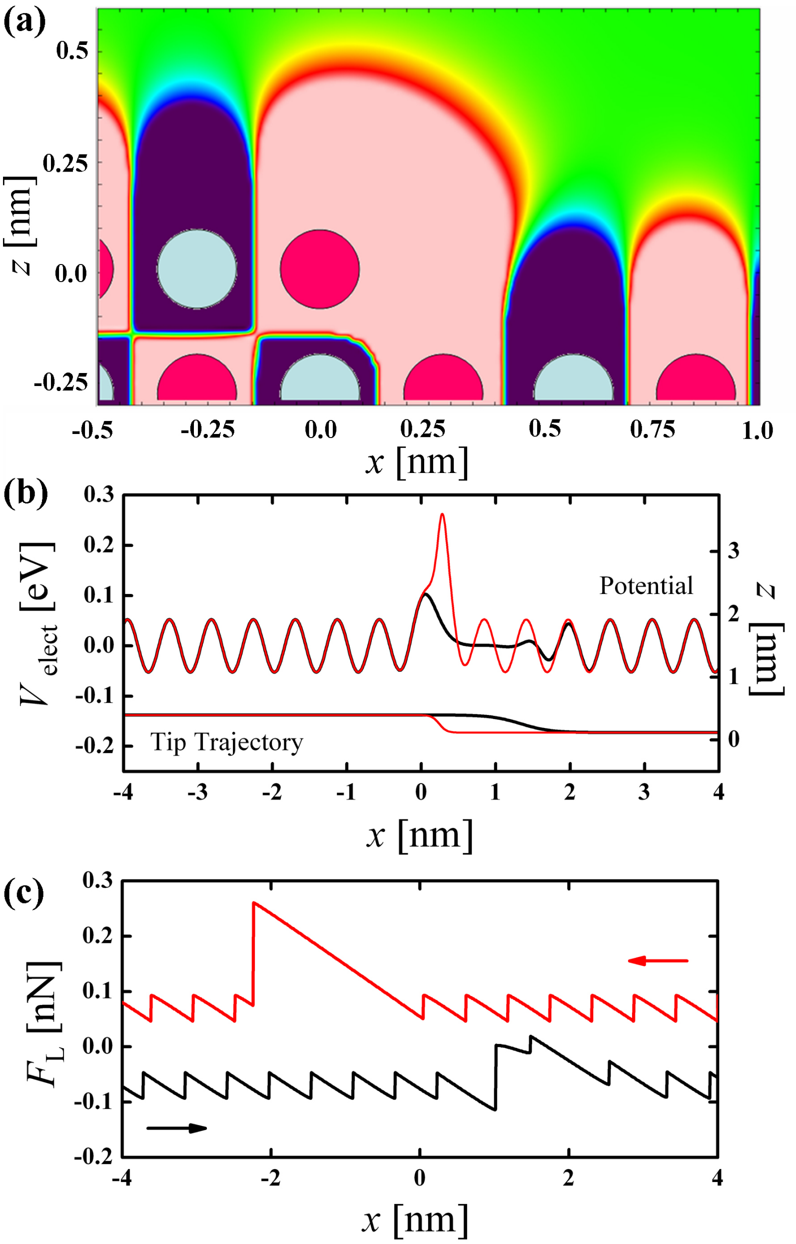

Figure 3.28: (a) Electrostatic potential map in the step edge region. (b) Tip path for the step-up (black) and step-down direction (red) with the corresponding variation of the electrostatic potential. The tip-surface distance over the terraces is $z = 0.4$ nm. (c) Profiles of the lateral forces calculated in the static approximation for the trajectories shown in (b). Note that for the sharp tip the lateral force is reduced at the step edge for the step-down direction. In addition there is a slight shift in the maxima of the lateral force profiles due to the torsion of the cantilever and the topography loop, as indicated also in the experiments.

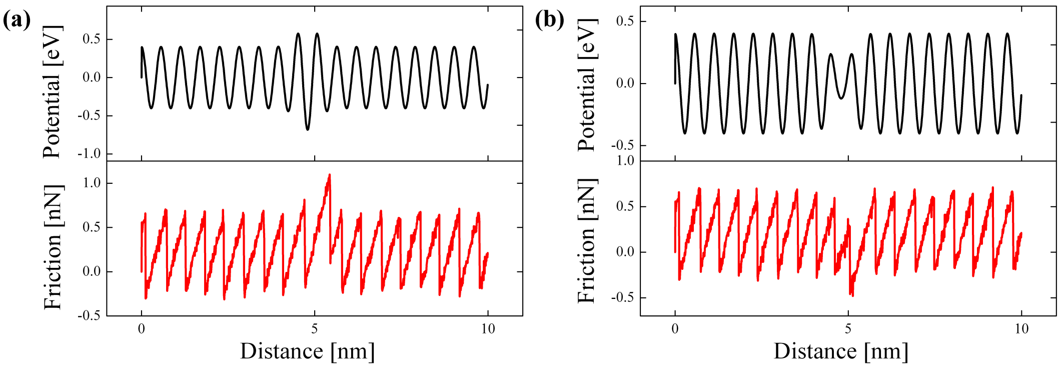

Figure 3.29: Calculated corrugation potential amplitudes and lateral friction forces on a step edge for (a) the step-up scan direction and (b) step-down scan direction. The calculation is based on the assumption that the tip apex feels a strong interaction when hitting the step edge from the lower terrace, whereas the interaction potential is reduced when the tip apex is sliding down to the lower terrace, as indicated by the hysteresis in topography in experiment. The higher corrugation potential in (a) leads to an increase in lateral force when scanning in step-up direction. Contrairy to this the reduced corrugation potential in (b) lowers the lateral force and the tip apex overcomes the cantilever and jumps in forward direction. Note that the positive sign of the lateral forces correspond to higher friction.

where A and B correspond to the weight and width of the Gaussian, which describes the increase and decrease of the corrugation potential at the step edge. C corresponds to the corrugation potential amplitude and D is the displacement of the step edge. In Fig. 3.29 the corrugation potentials and lateral forces are shown for (a) the step-up and (b) step-down scan directions using $A = 0.7$, $B = 0.5$ a, $C = 0.4$ eV and $D = 8.5$ a. Note that both scans are from left to right and positive values of the lateral force correspond to higher friction. The increased tip-surface interaction leads to higher lateral forces at the step edge, whereas a decrease of the interaction potential at the step edge leads to reduced lateral forces. This is in qualtitative agreement with the experiment using a sharp tip. Nevertheless, a more detailed model will be required, eventually on the basis of molecular dynamics simulations, to give further insight into the tip dynamics at the step edge. Furthermore, the model calculations described above are not capable of elastically deform the step edge itself, i.e. the sample material, which is indicated in the experiments by the fact that the unit cells appear to be larger at the step edge than on the terraces. This deformation of the step edge seems likely to have an influence on friction measurements and may be analysed using a more detailed calculation in future.

The tip used in Fig. 3.26 was terminated by a square area with side length $2a$. Based on simple geometry considerations, it is reasonable that the tip crosses that the step with a double jump, as shown in Fig. 3.30. This is confirmed by the bright stripe parallel to the step edge in Fig. 3.26(b), the width of which is $2a$. In such a way, the tip overtakes the cantilever, and experiences positive friction after jumping. When

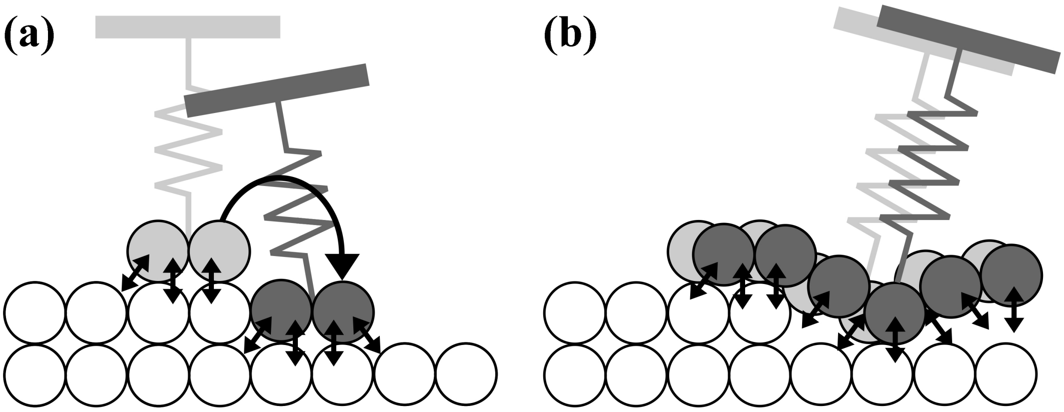

Figure 3.30: Simple model representing (a) the sharp tip and (b) the blunt tip. In (a) the tip overcomes the electrostatic barrier by overtaking the cantilever as indicated by the experiment and calculation. In the case of (b) the blunt tip the electrostatic forces act on both the upper and the lower terrace, which manifests in the overall enhanced attractive behaviour of the step edge and the increased lateral force for the step-down scan. For sake of simplicity, the fact that each unit cell is formed by two ions is ignored.

the tip is blunt, a "clean" jump like in Fig. 3.30 cannot occur. Quite reasonably, the crossing of the step edge occurs via by the formation and rupture of several ionic bonds. Local deformations and redistribution of the atoms at the tip apex cannot be excluded. Altogether, the edge will act as a pinning center for the tip motion, with an almost symmetric behavior of the lateral force in the two directions (upwards and downwards).

To sum up, the lateral force was measured across step edges using a commercial AFM tip in a sharp and a blunt condition. In the first case, a well-defined stick-slip motion is observed at the step edge, with a jump length corresponding to the tip width. The configuration of tip and cantilever with respect to the surface are quite similar while scanning up and down the step edge. This leads to overlapping lateral force profiles and indicates that the lateral force is reduced at the step edge when scanning step-down, which is contradicting to experimental results performed on larger scales [126]. The sharpness of the tip facilitates scanning the step edge without occurrence of the Schwöbel-Barrier. Contrary to this a blunt tip acts as a pinning center, where the lateral force is increased for the step-up direction as reported in previous experimental studies. In such case, only atomistic simulations [71] can reproduce the complex behavior of the tip apex, which is subject to localized deformations and to the formation of multiple ionic bonds with the surface atoms in the step region.

3.9 Conclusions

The probing tip of a FFM scanning on a flat surface is sticking in a potential well until the pulling force is high enough to overcome the static force and to induce a jump to an adjacent potential minima. This phenomenon is called *stick-slip* and is discussed in detail for a sharp tip scanning on flat surfaces like alkali halides and HOPG. Experimental results indicate that the tip apex consists of only a few atoms, which allows nearly atomic resolution in the lateral force maps as well as in the topography. Since the experiments are performed in UHV and the home-built FFM is properly damped and operated at excellent conditions, the obtained friction force images are of superior quality.

Numerical calculations are performed for a point mass dragged over a two-dimensional corrugation potential surface [32]. The dynamics are calculated using an extended Velocity Verlet algorithm, which is an integrator for the solution of the Langevin equation and comprises temperature effects. The use of a point mass is an appropriate assumption due to the experimental results which show that the tip apex consists of only a few atoms and the fact that the numerical results are in good agreement with experimental data. The transition from stick-slip to the smooth sliding of the tip over the surface in the ultra low friction regime is analysed. The numerical calculations support an improved understanding of three superlubricity states, namely the *static superlubricity*, *dynamic superlubricity* and *thermolubricity.* The static and dynamic superlubricity regimes are investigated numerically and experimentally, whereas the thermolubricity could not be demonstrated experimentally.

The code of the numerical model calculations is adapted to the fine superstructure which are observed in experiments in literature [130]. Different origins of rumpling effects which distort the surface planarity are all successfully attributed to a modulation of the corrugation potential, which are in good agreement with experimental data. In addition, the numerical calculations are also compared to stick-slip measurements at higher loads, where *multiple slips* occur. A comparison with the calculation also gives a further insight into mechanical properties as contact stiffness and dynamical properties of the sliding system as the damping coefficient, which is usually hard to determine experimentally [33].

The motion of the tip apex is analysed in detail numerically to improve the understanding of the stick-slip motion and effects of friction reduction. In experiments, the vertical and horizontal deflections give no direct insight into the motion of the tip apex itself. Here, an attempt is done to approach the tip motion from the experimental side. A combination of the vertical and horizontal deflections then result in a back-calculated trajectory of the tip. A superposition of the trajectory with the calculated surface lattice indicates that this approach is very promising.

To conclude, the stick-slip motion of the tip apex has been experimentally and numerically analysed profoundly in the case of normal friction and ultra low friction. The comparisons of experimental and numerical data give good agreement and result in an improved understanding of the tip dynamics in contact-AFM.

Glattes Eis, ein Paradies für den, der gut zu tanzen weiss.

FRIEDRICH NIETZSCHE

Chapter 4

Flexural Contact Resonance Atomic Force Microscopy

4.1 Introduction

In order to decrease the length scale in promising technological applications, instruments and techniques are being developed that are capable of characterising material mechanical properties with sub-micron spatial resolution. For instance, information about local mechanical properties of heterogenous materials such as elastic modulus, adhesion and friction is desirable. This demand is partly motivated by the increasingly common practice of integrating several materials, sometimes with very different properties, into a single device or structure. Therefore, a determination of the "average" properties of a sample is no longer sufficient. Instead, quantitative measurements and imaging techniques able to visualize the spatial distribution of properties are necessary, ultimately with nanoscale lateral resolution.

One instrument which can provide both the desired imaging capability and spatial resolution is the AFM [5]. Since the seminal work by Albrecht *et al.* [131], frequency demodulation detection has become a well-established technique in NC-AFM, which can in particular be used to obtain atomically resolved images of surfaces in UHV [132]. The detection of cantilever resonance characteristics has also emerged as the basis of techniques such as contact resonance atomic force microscopy (CR-AFM) including atomic force acoustic microscopy (AFAM) [133] and ultrasonic force microscopy (UFM) [134] as special cases as well as other AFM related techniques such as heterodyne force microscopy (HFM) [135], passive overtone microscopy [136], resonant difference-frequency atomic force ultrasonic microscopy (RDF-AFUM) [137]. Although termed "atomic", these techniques have actually been applied to probe surfaces and subsurface properties composite and/or structured materials on lateral scales of several up to typically hundreds of nanometers. In the same context Yamanaka *et al.* [138] were the first to use a phase-locked-loop (PLL) to track fundamental resonance frequency in contact while scanning. The more widespread method relies on the acquisition of the frequency spectrum of the cantilever in order to detect a number of contact resonance frequencies at each scan point [139–144]. Despite impressive advances in instrumentation and data processing [145], the latter method has the disadvantage that measurements of spectra are time-consuming.

Here, as state of the art NC-AFM, a PLL is used to both track and actuate the first flexural resonance frequency of a cantilever bearing a sharp AFM tip which executes stick-slip motion matching the lattice periodicity on an atomically flat crystal surface in UHV at room temperature. Variations of the contact resonance frequency during the stick stage in each atomic unit cell of the surface lattice are reliably detected, which represents a quite significant improvement in lateral resolution compared to previous contact resonance mapping. Furthermore, an enhanced sensitivity of the contact resonance to atomic scale defects is observed. More precisely, the variation of the resonance frequency in a particular unit cell is clearly distinct from its variation in the surrounding lattice sites, whereas the lateral force signal barely reveals specific features at this location. "True atomic resolution" of point defects within the limitations of conventional contact AFM and friction force microscopy (FFM) has seldom been observed, first by Ohnesorge *et al.* [146].

Several phenomenological models have been proposed to estimate the normal and lateral contact stiffness from the observed contact resonance frequencies for sufficiently small oscillation amplitudes [140, 145, 147]. They differ in the number of springs and dashpots, but have in common that each linear element accounts for a particular type of deformation (elastic or viscous, normal or lateral). Such deformations, which decay away from the contact region into the sample and the tip apex are inevitable. It is also important to take the cantilever inclination into account because it leads to a coupling of normal and lateral tip motion [140,142]. Here, these procedures are applied for the first time to a sharp tip contacting an alkali halide (001) surface on the atomic scale. It is shown that the resulting normal contact stiffness determined experimentally on the atomic scale is significantly smaller than in experiments on larger scales [139–144]. However, these experiments have been performed using either much higher loads and/or adhesion forces, which lead to a noticeably larger contact area and thus to a higher stiffness of the larger adjacent deformed region. Moreover, the contact stiffness and the diameter of the contact area have previously been estimated using continuum mechanics. Extensive comparisons between experiments and atomistic simulations have recently shown that although estimates based on continuum mechanics often yields reasonable values for high loads, they become questionable for nanometer-sized contacts, as demonstrated by sophisticated atomistic simulations [50, 111, 148, 149].

4.2 Atomic Scale Experiments on NaCl(001)

Cleaved alkali halide crystals are well-known model systems for studying friction on the atomic scale [42, 45, 151, 152]. The measurements have been performed on a NaCl(001) surface, which exhibits atomic scale stick-slip up to loads of tens of nN. The high intrinsic Q-factor ($> 3 \times 10^5$) of the cantilever (Nanosensors, PPP-CONT) drops as soon as the contact is formed ($< 5 \times 10^2$) whereas the fundamental flexural resonance frequency increases, as predicted by elastic beam theory [153]. Time-averaged variations of the lateral force F and of the flexural resonance frequency f_1 were simultaneously recorded in scans parallel to the [100]-symmetry direction. The measurements have been analyzed by means of the WSxM software [61]. Mechanical excitation of the cantilever at the contact resonance has to be performed in a careful way. Large excitation amplitudes have to be avoided in order not to deform the contact zone nonlinearly or in a destructive manner or to modify the conditions of atomic scale stick-slip. Nevertheless, the excitation must be strong enough to yield a deflection signal well above the noise within the measurement bandwidth. These requirements are easily met by the in-house designed UHV AFM [17] and a PLL-based detection electronics (Nanonis OC4) which can accurately track resonance frequency changes across the surface. In addition, the use of sufficiently small amplitudes avoids distortions of the contact resonance peak [154], also due to nonlinear effects, which may impede proper tracking of the contact resonance. The calibration of the oscillating deflection signal is nontrivial. Indeed, if the contact resonance frequency is strongly shifted away from its value out of contact, the cantilever end is nearly pinned, so that its oscillatory deflection profile considerably deviates from the commonly assumed quasistatic deflection profile [139, 153]. The measured time-dependent optical beam deflection is still proportional to the force on the tip, but the dynamic calibration constant is different from the quasistatic one. The amplitude of the oscillating force approximately estimated by assuming that the cantilever end is pinned, as described in the Appendix of Ref. [53], was 0.6 nN, i.e. much lower than in previous experiments which showed a significant reduction of friction by applied perpendicular actuation [43, 53]. Compared to the average static normal force of 2.9 nN and the small adhesion force of -0.9 nN, this small oscillating force ensures that in the present experiments the tip-sample normal force can be represented by a linear spring with effective stiffness $k_{\mathrm{cont,norm}}$ [153].

The interpretation of the contact frequency data is inspired by previous work on AFAM and UFM [140, 145], which relates the contact frequency to the normal and lateral contact stiffnesses. Taking into account that the cantilever is inclined by an angle $\alpha = 15^\circ$ with respect to the sample surface and that the tip is offset from the cantilever end (Fig. 4.1(a)), the contact stiffness in the normal direction $k_{\mathrm{cont,norm}}$ is determined using the linear model [150]:

$$\frac{k_{\mathrm{cont,norm}}}{k_{\mathrm{norm}}} = \frac{-B \pm \sqrt{B^2 - 4AC}}{6A}. \tag{4.1}$$

The quantities A, B and C in Eq. (4.1) can be expressed in terms of the cantilever dimensions, the wave number x_1 of the lowest flexural mode, and the lateral contact stiffness $k_{\mathrm{cont,lat}}$:

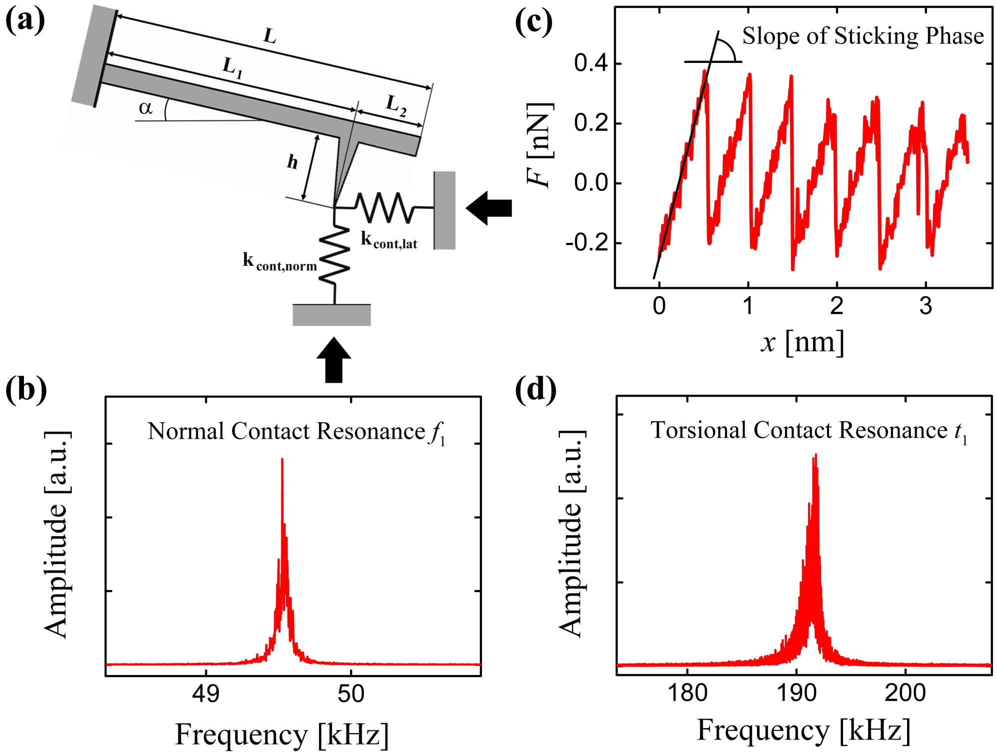

Figure 4.1: (a) The linear contact-resonance model used for rectangular cantilever with length L, width w, thickness t, and tip with height h located at $L_1 < L$ [150]. The remaining distance to the end of the cantilever is L_2. The cantilever is tilted with respect to the sample by an angle α. The tip is coupled to the sample by linear springs $k_{\mathrm{cont,norm}}$ and $k_{\mathrm{cont,lat}}$. The normal contact stiffness $k_{\mathrm{cont,norm}}$ is determined from (b) the flexural contact resonance frequency f_1, whereas the lateral contact stiffness is determined using either (c) the slope of the sticking part of the lateral force or (d) the torsional contact resonance frequency t_1. The resonance frequencies are determined from the positions of the corresponding peaks in measured thermally excited spectra [113].

$$
\begin{aligned}
A = \quad & \left(\frac{k_{\mathrm{cont,lat}}}{k_{\mathrm{cont,norm}}}\right)\left(\frac{h}{L_1}\right)^2(1-\cos(x_{\mathrm{n}}L_1)\cosh(x_{\mathrm{n}}L_1)) \\
& \times(1+\cos(x_{\mathrm{n}}L_2)\cosh(x_{\mathrm{n}}L_2)),
\end{aligned} \tag{4.2}
$$

$$
B = B_1 + B_2 + B_3, \tag{4.3}
$$

$$
C = 2(x_{\mathrm{n}}L_1)^4(1+\cos(x_{\mathrm{n}}L)\cosh(x_{\mathrm{n}}L)), \tag{4.4}
$$

with [155]

$$
\begin{aligned}
B_1 = \quad & \left(\frac{h}{L_1}\right)^2(x_{\mathrm{n}}L_1)^3\big(\sin^2(\alpha)+\frac{k_{\mathrm{cont,lat}}}{k_{\mathrm{cont,norm}}}\cos^2(\alpha)\big) \\
& \times[(1+\cos(x_{\mathrm{n}}L_2)\cosh(x_{\mathrm{n}}L_2))(\sin(x_{\mathrm{n}}L_1)\cosh(x_{\mathrm{n}}L_1) \\
& +\cos(x_{\mathrm{n}}L_1)\sinh(x_{\mathrm{n}}L_1)) - (1-\cos(x_{\mathrm{n}}L_1)\cosh(x_{\mathrm{n}}L_1)) \\
& \times(\sin(x_{\mathrm{n}}L_2)\cosh(x_{\mathrm{n}}L_2)+\cos(x_{\mathrm{n}}L_2)\sinh(x_{\mathrm{n}}L_2))],
\end{aligned} \tag{4.5}
$$

$$
\begin{aligned}
B_2 = \quad & 2\left(\frac{h}{L_1}\right)(x_{\mathrm{n}}L_1)^2\big[\big(\frac{k_{\mathrm{cont,lat}}}{k_{\mathrm{cont,norm}}}-1\big)\cos(\alpha)\sin(\alpha)\big] \\
& \times[(1+\cos(x_{\mathrm{n}}L_2)\cosh(x_{\mathrm{n}}L_2))\sin(x_{\mathrm{n}}L_1)\sinh(x_{\mathrm{n}}L_1) \\
& +(1-\cos(x_{\mathrm{n}}L_1)\cosh(x_{\mathrm{n}}L_1))\sin(x_{\mathrm{n}}L_2)\sinh(x_{\mathrm{n}}L_2)],
\end{aligned} \tag{4.6}
$$

$$
\begin{aligned}
B_3 = \quad & (x_{\mathrm{n}}L_1)\big(\cos^2(\alpha)+\frac{k_{\mathrm{cont,lat}}}{k_{\mathrm{cont,norm}}}\sin^2(\alpha)\big) \\
& \times[(1+\cos(x_{\mathrm{n}}L_2)\cosh(x_{\mathrm{n}}L_2))(\sin(x_{\mathrm{n}}L_1)\cosh(x_{\mathrm{n}}L_1) \\
& -\cos(x_{\mathrm{n}}L_1)\sinh(x_{\mathrm{n}}L_1)) - (1-\cos(x_{\mathrm{n}}L_1)\cosh(x_{\mathrm{n}}L_1)) \\
& \times(\sin(x_{\mathrm{n}}L_2)\cosh(x_{\mathrm{n}}L_2)-\cos(x_{\mathrm{n}}L_2)\sinh(x_{\mathrm{n}}L_2))].
\end{aligned} \tag{4.7}
$$

The cantilever used in the experiment has a length $L = 470\ \mu\mathrm{m}$, a width $w = 45\ \mu\mathrm{m}$, and a thickness $t = 1.64\ \mu\mathrm{m}$ determined from the free resonance frequency f_1^0 of the first mode [28]. The tip height is $h = 13\ \mu\mathrm{m}$, and the tip is located at $L_1 = 445\ \mu\mathrm{m}$. Using elastic beam theory, spring constants of $k_{\mathrm{norm}} = 0.095$ N/m for the flexural and $k_{\mathrm{tors}} = 59.4$ N/m for torsional deflections are estimated [59]. The wave number x_1 is given by

$$
x_1 L = x_1^0 L\sqrt{\frac{f_1}{f_1^0}}, \tag{4.8}
$$

where f_1 is the resonance frequency of the fundamental normal mode in contact, f_1^0 is the resonance frequency out of contact, and $x_1^0 L = 1.875$ [153].

The stiffness $k_{\mathrm{cont,lat}}$ is assumed to be isotropic, as suggested by a recent comparison

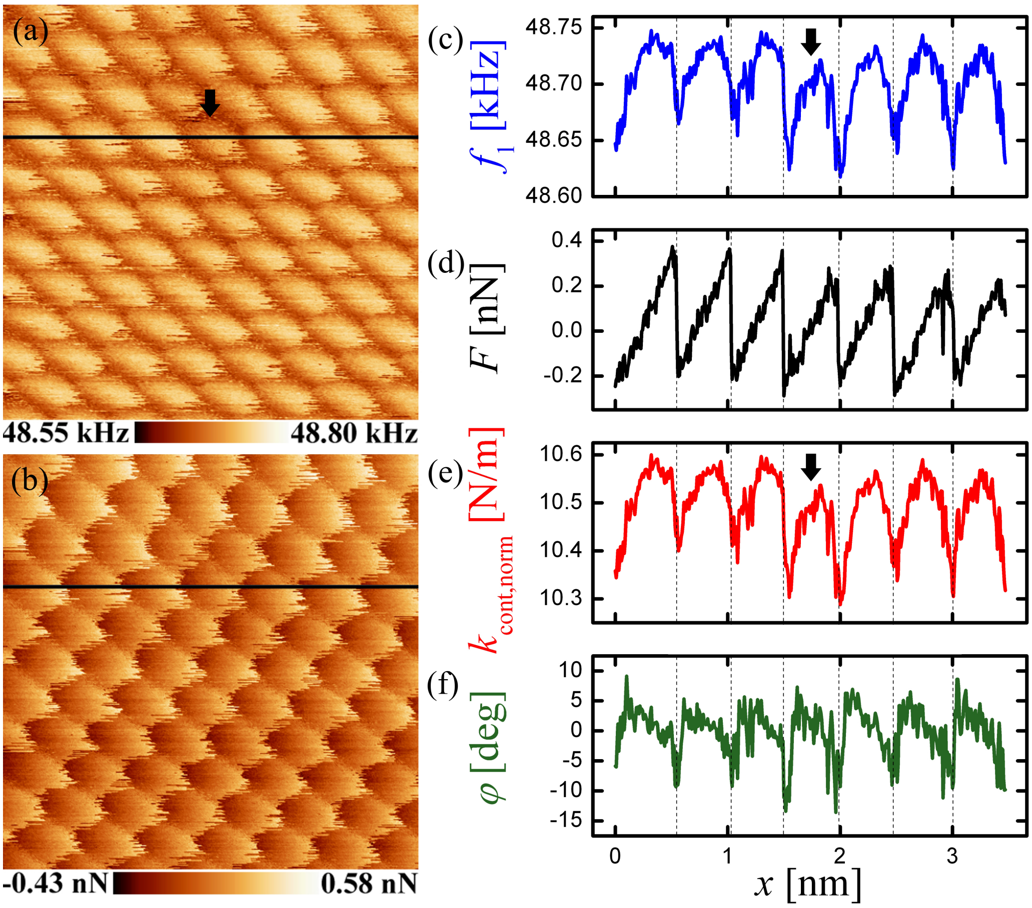

Figure 4.2: Raw data of (a) the flexural contact resonance map and (b) lateral force map measured simultaneously on NaCl(001). The contact resonance frequency map is used to calculate the normal contact stiffness $k_{\mathrm{cont,norm}}$. (c)-(f) Profiles along the indicated scan line show the contact resonance (blue), the lateral force (black), the calculated contact stiffness (red) and phase (green), which all exhibit patterns consistent with atomic scale stick-slip motion. As indicated by the black arrows, the contact resonance and thus the contact stiffness show a local decrease, indicating an atomic defect, with no equivalent feature in the lateral force or in the vertical deflection (not shown). Load = 2.9 nN, normal oscillation amplitude = 50 pm.

between computer simulations of atomic scale friction [32] and in-house measurements on alkali halides [53]. This hypothesis allows us to use two different methods to estimate $k_{\mathrm{cont,lat}}$ (see Fig. 4.1). One possibility is to extract $k_{\mathrm{cont,lat}}$ from the slope k_{exp} of the stick segments of the lateral force, taking into account the correction due to the tip-surface corrugation potential, namely [42]

$$\frac{1}{k_{\mathrm{exp}}} = \frac{1}{k_{\mathrm{eff}}}\left(1 + \frac{1}{\eta}\right), \tag{4.9}$$

η being the ratio of the lateral "interaction stiffness" at the bottom of each potential well where the tip sticks and of the effective stiffness of the cantilever in contact k_{eff} [57, 156]

$$\frac{1}{k_{\mathrm{eff}}} = \frac{1}{k_{\mathrm{tors}}} + \frac{1}{k_{\mathrm{cont,lat}}}. \tag{4.10}$$

The parameter η can be experimentally determined from k_{exp}, the maximum lateral force F_{max} and the lattice constant (0.564 nm for NaCl) [42], as

$$\eta = \frac{2\pi F_{\mathrm{max}}}{k_{\mathrm{exp}} a} - 1. \tag{4.11}$$

Eq. (4.11) follows if a cosine corrugation potential is assumed [48, 49], which was shown to describe well wearless stick-slip friction on alkali halide (001) surfaces at low loads [42].

Alternatively, $k_{\mathrm{cont,lat}}$ can be estimated from the measured torsional resonance of the cantilever in contact [157]:

$$\frac{k_{\mathrm{cont,lat}}}{k_{\mathrm{tors}}} = -\frac{y_1 L \cos(y_1 L)}{\sin(y_1 L_1)\cos(y_1 L_2)}. \tag{4.12}$$

The wave number y_1 of the first torsional mode is directly related to the torsional resonance frequencies in contact t_1 and out of contact t_1^0 by

$$y_1 L = \frac{\pi}{2}\frac{t_1}{t_1^0}. \tag{4.13}$$

Note that in contrast to previous work [139, 150, 158] k_{eff} is not dominated by the torsional spring constant of the cantilever, but rather by the lateral contact stiffness, which is much weaker for the low loads (< 5 nN) used in the present experiments. From the slope of the stick-slip curve in Fig. 4.1(c) and Eq. (4.9,4.10)a lateral contact stiffness $k_{\mathrm{cont,lat}} = 5.55$ N/m is estimated. This value differs only by 7 % from the lateral contact stiffness $k_{\mathrm{cont,lat}} = 5.18$ N/m determined from Eq. (4.12).

Figs. 4.2(a) and (c) show a contact resonance map acquired on NaCl(001) in constant height mode and the corresponding line profile (load = 2.9 nN, force modulation 0.6 nN). The profile of the phase in Fig. 4.2(f) shows that that phase errors are small during the stick stages, so that the PLL then tracks the frequency changes. As already mentioned, the average value of the resonance frequency in contact, f_1, is much higher than the resonance frequency $f_1^0 = 10.2$ kHz of the free cantilever and is closer to the flexural resonance of the pinned cantilever rather than to the fundamental resonance out of contact. This is a necessary condition for the applicability of the adopted amplitude calibration procedure. The corresponding lateral force map (Fig. 4.2(b)) shows that the AFM tip periodically sticks in a minimum of the surface potential, until the lateral force becomes high enough to induce a sudden jump into the next minimum [48]. From the slope of the stick-slip curve in Fig. 4.2(d) and Eq. (4.9,4.10) a lateral contact stiffness $k_{\text{cont,lat}} = 1.58$ N/m is estimated. The average value of the normal contact stiffness $k_{\text{cont,norm}} = 11.44$ N/m determined from Eqs. (4.1-4.7) (see profile in Fig. 4.2(e)) is much higher than the cantilever spring constant $k_{\text{norm}} = 0.095$ N/m for the normal mode. This reflects the fact that the cantilever deflection is much stronger than the deformation of the contact region in the normal direction. The opposite situation is observed in the sliding direction, where the lateral deformation of the contact region prevails over the cantilever torsion. The value of the lateral contact stiffness is roughly in agreement with previous measurements [42] on NaCl(001) using loads < 5 nN.

The value of the normal contact stiffness is about a factor of $2 - 8$ larger than the lateral contact stiffness. On different materials (epoxy matrix and carbon fibers [139], WC-C cermet [140], granular Au films [144], polymers [159], metal alloys [160]) much higher values of the normal contact stiffness have been estimated using similar techniques on larger scales. This is likely related to the larger contact areas characterizing these experiments, none of which were performed on the atomic scale. As revealed by recent atomistic simulations [50,111,149], values of the lateral contact stiffness can already differ quite strongly from continuum mechanics models for contact diameters of a few nanometers. Nevertheless, the normal contact stiffness is rather close to predictions of such simple continuum models. In this case, the value of the normal contact stiffness $k_{\text{cont,norm}} = 10.46$ N/m can be used to approximately estimate a small contact diameter of $k_{\text{cont,norm}}/E^*_{\text{eff}} = 0.3$ nm (cylinder on flat [34]), where an effective Young modulus $E^*_{\text{eff}} = 34.8$ GPa was assumed. The effective Young modulus is given by

$$\frac{1}{E^*_{\text{eff}}} = \frac{1-\nu^2_{\text{NaCl}}}{E_{\text{NaCl}}} + \frac{1-\nu^2_{\text{Si}}}{E_{\text{Si}}}, \tag{4.14}$$

which takes into account the bulk Young moduli of NaCl ($E^*_{\text{NaCl}} = 42.7$ GPa) and Si ($E^*_{\text{Si}} = 189.7$ GPa), as well as the Poisson ratios $\nu_{\text{NaCl}} = 0.25$ and $\nu_{\text{Si}} = 0.33$.

This contact diameter is in reasonable agreement with the observed resolution of atomic scale defects, thus confirming that the normal contact stiffness provides adequate estimate of the average contact size. The variation of the contact resonance frequency relative to f_1 across each unit cell are small (0.2 %), which means that the contact size is rather constant during the stick stages.

In order to further understand the normal stiffness variation across the unit cell, the profiles in Figs. 4.2(c) and (d) are compared. The maximum value of the contact resonance frequency approximately corresponds to the perpendicular alignment of the tip, where the lateral force is zero. In this situation of minimum lateral stress, presumably the largest normal contact stiffness $k_{\text{cont,norm}}$ is established. As the lateral stress increases, this stiffness is slightly reduced in a non-linear fashion, a result not expected from continuum mechanics, which clearly demonstrates the nonlinear but still elastic behavior of these small contacts. Qualitatively, the normal restoring force on the tip apex is maximal in the configuration with no applied lateral stress. In contrast, the binding of the nanotip in the stressed case is weaker, and the normal stiffness is consequently lower, for those configurations which are close to the lateral slip instability of the tip. It is important to note that the flexural resonance frequency decreases shortly before each slip event, around which the contact resonance drops to its initial value but cannot be accurately followed, owing to the finite PLL response time (> 1 ms). Hence, the contact resonance may be used as an indicator of a forthcoming slip event. Such a behavior might also be relevant for macro-slip events, such as earth quakes [161], where early warning systems are still missing. At present, it is beyond the scope of this paper to make reliable predictions whether this technique can be extended to larger scales.

The technique of measuring contact resonances using the PLL technique also appears to be more sensitive to atomic defects than conventional FFM. As shown in Figs. 4.2(a) and (c) the resonance frequency f_1 is reduced at one well-defined location on the crystal surface (indicated by black arrows), suggesting the presence of a vacancy or chemical impurity, perhaps at a subsurface site. Note that the corresponding lateral force map (Fig. 4.2(b)) and vertical deflection image (not shown) barely reveal specific features at this location.

4.3 KBr film on Cu(111)

The flexural contact resonance technique can be used to detect and determine a substrate material. However, this works for unknown materials only if there exists a reference measurement with the same cantilever. Buf if the substrate consisting of different chemical compositions is known, the contact resonance can readily determine the composition of the substrate, whereas the topography image does not contain any information about the chemical composition nor does the lateral force image always show a distict difference between the friction forces measured on different materials. Fig. 4.3 shows a measurement on Cu(111) with evaporated KBr islands. The island consist of at least a double layer of KBr and also higher island are observed. The mid part of the contact resonance map consists of bare copper, which is not covered by KBr. The flexural contact resonance is noticably higher on copper than on KBr, which manifests in the bright mid part of the measurement, and makes it possible to identify the different materials by the contatct resonance frequency. In the topography image, the different materials can not be distinguished (image not shown), only structure features like the rectangular island allow to suggest the substrate material. The lateral force shows a minor difference of the friction behaviour on the different materials (see Fig. 4.3(b)). However the determination of the chemical composition by a lateral force measurement is more difficult because the difference in friction is less distinct as in the contact resonance frequency.

In principle, the CR-AFM technique is already demonstrated on large scales for the flexural [139, 140, 142–144, 154, 162] and torsional modes [157, 159, 163]. However, flexural CR-AFM is now shown for the first time on double layer film, and together with the results from Section 4.2 gives evidence that it is possible to determine the chemical composition of structures on the atomic scale.

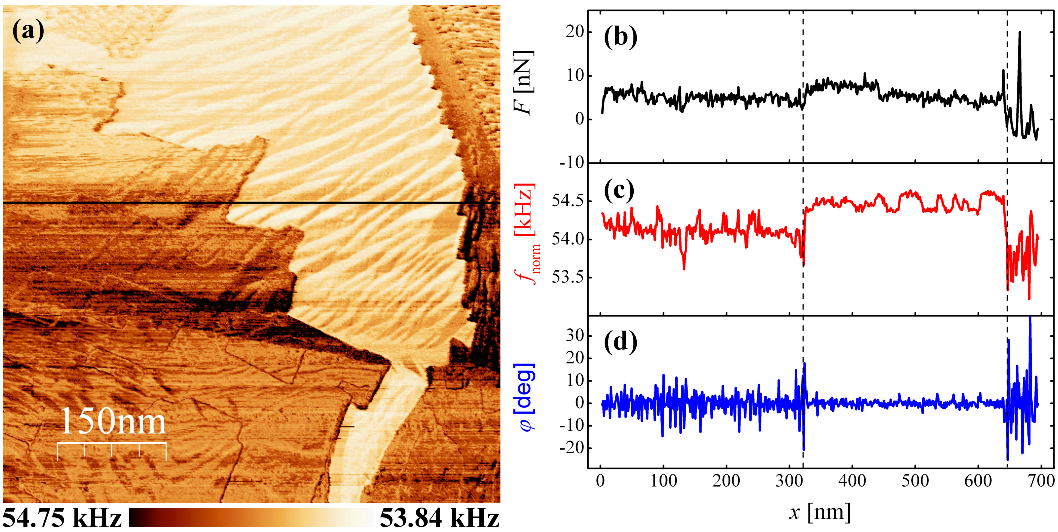

Figure 4.3: (a) Raw data of the flexural contact resonance map measured without actuation and using a load = 3.9 nN. Profiles are taken along the black line for (b) the friction force, (c) the flexural contact resonance and (d) the phase. The contact resonance map clearly shows Cu in the mid, and the evaporated KBr film on the left and right side. The main KBr film consists of a double layer, but also higher islands are visible on the left side. (b) While the friction force only slightly increases on Cu(111), as indicated by the dashed lines, (c) the flexural contact resonance distinctly increases on Cu. (d) The phase demonstrates that the PLL reasonably tracks the contact resonance, apart from the right side where it is also difficult to measure the lateral force. In the contact resonance map the different substrate materials are readily distinguished, wheras the difference in lateral force is less pronounced.

4.4 Conclusions

In conclusion, atomic scale friction studies are extended by applying a dynamical method, where the normal contact frequency is simultaneously tracked by a PLL. Due to the excellent signal-to-noise ratio of the instrumental setup, small excitation amplitudes compatible with a linear elastic model of the contact can be used. Variations of the normal contact frequency are compared with the lateral force variations during atomic stick-slip events. The normal contact frequency and the deduced normal contact stiffness reach maximum values when the contact is not stressed in the lateral direction. A decrease in the normal contact frequency is then followed by a lateral slip of the contact, which may be used as an indicator for predicting a forthcoming slip event even in situations where stick-slip motion is no longer periodic. The technique also reveals atomic defects, which are not clearly detected in the lateral force or in the vertical deflection. Atomic scale contact resonance imaging is also promising for the study of heterogeneous surfaces on the nanoscale. Besides nano-structures, subsurface defects might be easier to detect than in conventional FFM. An application of the PLL technique to torsional resonances would also be of great benefit to study material properties on the nanoscale.

> *Jede Lösung eines Problems ist ein neues Problem.*
>
> Johann Wolfgang von Goethe

Chapter 5

Torsional Contact Resonance Atomic Force Microscopy

5.1 Introduction

The frictional forces experienced by a sharp tip sliding on a solid surface are ultimately related to the stiffness and the resonance frequencies of the contacting region. While frequency detection is well-established in non-contact atomic force microscopy, where atomically resolved images of several crystal surfaces are readily obtained in ultra-high vacuum (UHV) [132], recent contact resonance atomic force microscopy (CR-AFM) measurement using the flexural contact resonance frequency has shown to be capable to detect atomically resolved images of NaCl(001) [84]. In this Chapter, CR-AFM is applied to the first torsional mode on KBr(001) on the atomic scale and show that this technique is also sensitive to atomic defects. In addition, a coupled spring model is derived, which is combined with the Tomlinson model [32] to be compared to the experiment and to explain the behaviour of the torsional contact resonance during the slip stages.

5.2 Atomic Scale Experiments on KBr(001)

Cleaved alkali halide crystals are well-known model systems for studying friction on the atomic scale [42, 45, 151, 152]. The measurements have been performed on an KBr(001) surface, which exhibits atomic-scale stick-slip up to loads of tens of nN. The high intrinsic Q factor ($> 2 \times 10^4$) for the first torsional mode of the cantilever drops as soon as the contact is formed ($< 2 \times 10^2$) whereas the fundamental torsional resonance frequency increases slightly. Time-averaged variations of the lateral force F and of the torsional resonance frequency t_1 were simultaneously recorded in scans parallel to the [100]-symmetry direction. The measurements have been analyzed by means of the WSxM software [61]. The home built Friction Force Microscope (FFM) is operated at room temperature, which means that the torsional contact resonance frequency is thermally actuated. The quality of the resonance peak is high enough to be tracked by the PLL based detection electronics (Nanonis OC4). This is in contrast to the detection of the normal contact resonance [84] where mechanical excitation using constant amplitude was used to facilitate the normal contact resonance to be tracked. Exactly the opposite behaviour is observed, when using mechanical excitation the noise increases and makes it difficult for the PLL to track the signal. The calibration of the torsional oscillation amplitude is non-trivial and is not discussed within this Section. However, this is not necessary because the cantilever is not actuated and the thermal noise amplitude is in the pN range.

Fig. 5.2(a) and (b) show a torsional contact resonance map acquired on KBr(001) in constant height mode and the corresponding line profile (Load = 1.1 nN). The profile of the phase in Fig. 5.2(e) shows that the phase errors are small during the stick stages, which means that the PLL reasonably tracks the frequency changes. The corresponding lateral force map (Fig. 5.2(b)) shows that the AFM tip periodically sticks in a minimum of the surface potential, until the lateral force becomes high enough to induce a sudden jump into the next minimum [48]. From the slope of the stick-slip curve in Fig. 5.2(d) a lateral contact stiffness $k_{\mathrm{cont,lat}} = 3.80$ N/m is estimated. Alternatively, the lateral contact stiffness can be determined using the torsional resonance method [157], which gives $k_{\mathrm{cont,lat}} = 3.47$ N/m and deviates 8% from the lateral contact stiffness estimated by the slope of the stick stages. The value of the lateral contact stiffness is in agreement with previous measurements [38, 70] on KBr(001) using loads < 5 nN.

The torsional contact resonance shows to be sensitive to atomic-scale defects, as indicated in Fig. 5.2(a) and (c) by black arrows, suggesting the presence of a vacancy or chemical impurity. Note that the torsional contact resonance frequency is lowered at this well defined position, whereas the corresponding lateral force map (Fig. 5.2(b)) and vertical deflection image (not shown) barely reveal specific features at this location. The value of the normal contact stiffness $k_{\mathrm{cont,norm}} = 10.64$ N/m can be used to approximately estimate a small contact radius of $k_{\mathrm{cont,norm}}/(2E_{\mathrm{eff}}) = 0.16$ nm (cylinder on flat [34]), where an effective Young modulus $E_{\mathrm{eff}} = 33.6$ GPa was assumed. The effective Young modulus is given by

$$\frac{1}{E_{\mathrm{eff}}} = \frac{1-\nu_{\mathrm{KBr}}^2}{E_{\mathrm{KBr}}} + \frac{1-\nu_{\mathrm{Si}}^2}{E_{\mathrm{Si}}}, \tag{5.1}$$

which takes into account the bulk Young moduli of KBr ($E_{\mathrm{KBr}} = 26.8$ GPa) and Si ($E_{\mathrm{Si}} = 189.7$ GPa), as well as the Poisson ratios $\nu_{\mathrm{KBr}} = 0.28$ and $\nu_{\mathrm{Si}} = 0.33$. This contact radius is in reasonable agreement with the observed resolution of atomic-scale defects, thus confirming that the normal contact stiffness provides an adequate estimate of the average contact size.

In order to further understand the torsional contact resonance variation across the

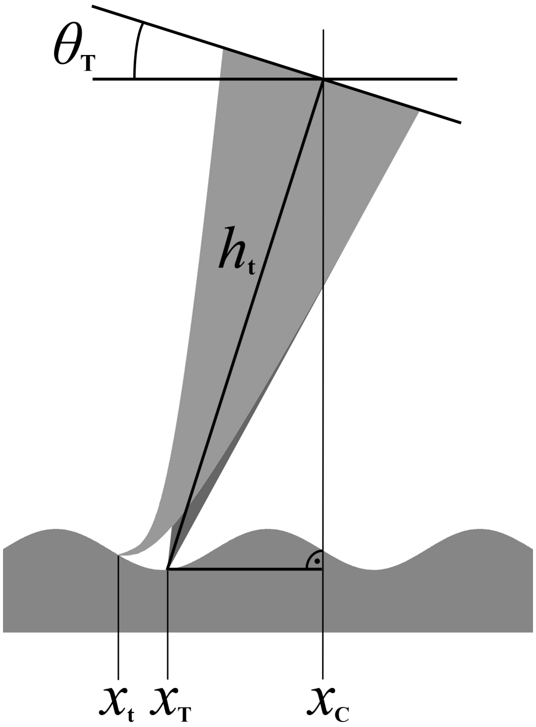

Figure 5.1: The contact resonance model using two coupled springs is used to explain the behaviour of the torsional contact resonance frequency around a slip event. A tip with tip height h_t is tilted during the friction measurement by an angle θ_T. The position of the tip x_T due to the torsion of the cantilever is then slightly shifted from the cantilever position x_C. The flexible tip apex is spring coupled to the tip motion, which leads to a shift of the tip apex position x_t from the tip position x_T. Around this statical tip apex position x_t, the tip apex is oscillating with high frequency (see text).

unit cell, the profiles in Fig. 5.2(c) and (d) are compared with the calculated profiles in Fig. 5.3. The calculation was performed using the same spring constant, load and similar scan velocity as used in the experiment. Because the simulation was performed at zero temperature, slightly higher lateral forces were obtained. A tip mass of $M = 5.1 \times 10^{-11}$ kg was used to obtain the values for the torsional contact resonance as in the experiment. In addition, only points where the tip had double or less of the scan velocity of the cantilever are shown in Fig. 5.3, for clarity and to focus on the characteristic behaviour of the torsional contact resonance around the slip position. In the coupled-spring model, the torsional contact resonance approaches zero at the critical tip position $\overline{x}_\mathrm{crit}$, and then immediately increases again. In principle, at $\overline{x}_\mathrm{crit}$ there is no contact resonance anymore. However, in the experiment the PLL can not track the contact resonance fast enough, which leads to a fast decrease followed by a fast increase. Hence, around the slip events, the torsional contact resonances is not good enough to be trusted, as also indicated by a higher phase error (see Fig. 5.2(e)). The important and characteristic feature is that the contact resonance is decreasing before the slip event, which in principle may be used as an indicator of a forthcoming slip event. Such a behavior might also be relevant for macro-slip events, such as earthquakes [161], where early warning systems are still missing. At present, it is beyond the scope of this paper to make reliable predictions whether this technique can be extended to larger scales.

5.3 Contact Resonance Model

A contact resonance model is developed to explain the behaviour of the torsional contact resonance around the slip stages. The model is basically a two-spring model with corrugation, as is illustrated in Fig. 5.1. One spring k_T describes the torsion of the cantilever using a bulk tip mass M, which position x_T is then slightly shifted from the cantilever support x_C. The bulk tip is coupled by a second spring k_t to the tip apex which is coupled to the support and leads to a tip apex position x_t which is again different from the bulk tip position x_T. In the equilibrium position of the quasi-static limit, the forces acting on these two springs are

$$k_\mathrm{T}(x_\mathrm{T} - x_\mathrm{C}) = k_\mathrm{t}(x_\mathrm{t} - x_\mathrm{T}) = \frac{\partial U}{\partial x_\mathrm{t}}, \tag{5.2}$$

where U is the interaction potential between the tip apex and the periodic surface. As a first approximation the potential U has a sinusoidal profile as [42]

$$U(x_\mathrm{t}) = -\frac{E_0}{2}\cos\left(\frac{2\pi}{a}x_\mathrm{t}\right), \tag{5.3}$$

where a is the lattice constant ($a = 0.660$ nm for KBr) and E_0 is the amplitude of the corrugation potential. The amplitude E_0 is related to the tip-sample interaction (and thus to the externally applied load) in the experiment and is assumed to obey a linear dependence with respect to the load. Combining Eqs. (5.2)and (5.3) and using the relation for the effective spring constant [156] $1/k_\mathrm{eff} = 1/k_\mathrm{T} + 1/k_\mathrm{t}$ gives

$$k_\mathrm{eff}(x_\mathrm{t} - x_\mathrm{C}) = \frac{\pi E_0}{a}\sin(\frac{2\pi}{a}x_\mathrm{t}). \tag{5.4}$$

The dynamics of the tip apex is described by the Newton equation of motion

$$m\ddot{x}_\mathrm{t} + \gamma_\mathrm{t}\dot{x}_\mathrm{t} + k_\mathrm{t}(x_\mathrm{t} - x_\mathrm{T}) = -\frac{\partial U}{\partial x_\mathrm{t}}, \tag{5.5}$$

where $m\ddot{x}_\mathrm{t}$ is the total force, $\gamma_\mathrm{t}\dot{x}_\mathrm{t}$ the damping, $k_\mathrm{t}(x_\mathrm{t} - x_\mathrm{T})$ the restoring force and $\partial U/\partial x_\mathrm{t}$ the force caused by the potential. Eq. (5.5) is coupled by the restoring force $k_\mathrm{t}(x_\mathrm{t} - x_\mathrm{T})$ to the equation of motion of the bulk tip

$$M\ddot{x}_\mathrm{T} + \gamma_\mathrm{T}\dot{x}_\mathrm{T} + k_\mathrm{T}x_\mathrm{T} - k_\mathrm{t}(x_\mathrm{t} - x_\mathrm{T}) = 0. \tag{5.6}$$

When assuming that the system performs only small torsional oscillations, the coordinates $x_\mathrm{t,T}$ can be split up into a "slow" quasi-static part $\overline{x}_\mathrm{t,T}$ and a "fast" dynamic part $\tilde{x}_\mathrm{t,T}$ as $x_\mathrm{t,T} = \overline{x}_\mathrm{t,T} + \tilde{x}_\mathrm{t,T}$.

In the equations of motions the coordinates are then split up into a quasi-static and a dynamic part as described above. Since the dynamic part of the tip apex

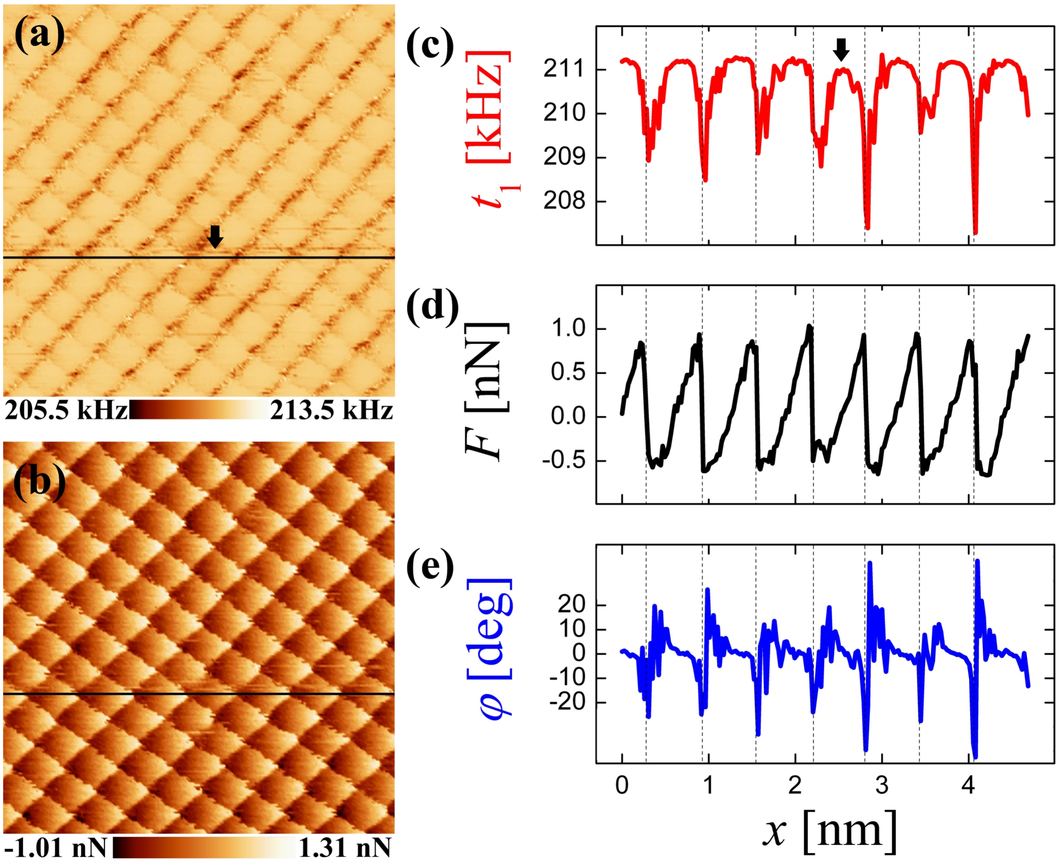

Figure 5.2: Raw data of (a) the torsional contact resonance map and (b) lateral force map measured simultaneously on KBr(001). (c)-(e) Profiles along the indicated scan line show the contact resonance (red), the lateral force (black) and phase (blue), which all exhibit patterns consistent with atomic-scale stick-slip motion. As indicated by black arrows, the torsional contact resonance exhibits a local decrease, indicating an atomic defect, with no equivalent feature in the lateral force or in the vertical deflection (not shown). Load = 1.1 nN.

and bulk tip are assumed to behave in a periodic fashion, they can be described by harmonic oscillations. A Fourier-Transformation is performed where only the real part is considered of the dynamic motions which leads to $\mathrm{Re}(x_{\mathrm{t,T}}) \propto x_{\mathrm{t,T}}e^{-i\omega t}$. The quasi-static motions are not considered because they are not harmonic and consequently their Fourier-Transform do not result in a frequency. The equation of motion for the tip apex is then described as

$$[-m\omega^2 - i\omega_{\mathrm{t}}\gamma_{\mathrm{t}} + k_{\mathrm{t}}]\tilde{x}_{\mathrm{t}} - k_{\mathrm{t}}\tilde{x}_{\mathrm{T}} = -\eta k_{\mathrm{eff}}\tilde{x}_{\mathrm{t}}\cos\left(\frac{2\pi}{a}\overline{x}_{\mathrm{t}}\right) \tag{5.7}$$

and for the bulk tip as

$$[-M\omega^2 - i\omega\gamma_{\mathrm{T}} + k_{\mathrm{T}} + k_{\mathrm{t}}]\tilde{x}_{\mathrm{T}} = k_{\mathrm{t}}\tilde{x}_{\mathrm{t}}, \tag{5.8}$$

using the friction parameter $\eta = 2\pi^2 E_0/k_{\mathrm{eff}}a^2$ in consistency with literature [42]. Note that the frequency $\omega = \sqrt{k_{\mathrm{T}}/M}$ of the bulk tip oscillations is much lower than the frequency $\omega_{\mathrm{t}} = \sqrt{k_{\mathrm{t}}/m}$ of the tip apex with respect to the fixed cantilever. This allows to neglect $m\omega_{\mathrm{t}}^2$ in Eq. (5.7) which leads to

$$[-i\omega\gamma_{\mathrm{t}} + k_{\mathrm{t}} + \eta k_{\mathrm{eff}} \cos\left(\frac{2\pi}{a}\overline{x}_{\mathrm{t}}\right)]\tilde{x}_{\mathrm{t}} \approx k_{\mathrm{t}}\tilde{x}_{\mathrm{T}}. \tag{5.9}$$

Solving Eq. (5.9) for $k_{\mathrm{t}}\tilde{x}_{\mathrm{t}}$ and substituting into Eq. (5.8) gives

$$\begin{aligned} &[-M\omega^2 - i\omega\gamma_{\mathrm{T}} + k_{\mathrm{T}} + k_{\mathrm{t}}]\tilde{x}_{\mathrm{T}} \\ &= \frac{k_{\mathrm{t}}\tilde{x}_{\mathrm{T}}}{-i\frac{\omega\gamma_{\mathrm{t}}}{k_{\mathrm{t}}} + 1 + \frac{\eta k_{\mathrm{T}}}{k_{\mathrm{t}} + k_{\mathrm{tT}}}\cos\left(\frac{2\pi}{a}\overline{x}_{\mathrm{t}}\right)}, \end{aligned} \tag{5.10}$$

The denominator of Eq. (5.10) is expanded to the first order of $(\omega\gamma_{\mathrm{t}})/k_{\mathrm{t}}$:

$$\begin{aligned} [-M\omega^2 - i\omega\gamma_{\mathrm{T}} + k_{\mathrm{T}} + k_{\mathrm{t}}]\tilde{x}_{\mathrm{T}} &= \frac{k_{\mathrm{t}}\tilde{x}_{\mathrm{T}}}{D - i\frac{\omega\gamma_{\mathrm{t}}}{k_{\mathrm{t}}}} \\ = \frac{k_{\mathrm{t}}\tilde{x}_{\mathrm{T}}}{D}\left(1 + i\frac{\omega\gamma_{\mathrm{t}}}{k_{\mathrm{t}}D}\right) &= \frac{k_{\mathrm{t}}\tilde{x}_{\mathrm{T}}}{D} + i\frac{\omega\gamma_{\mathrm{t}}}{D^2}\tilde{x}_{\mathrm{T}}, \end{aligned} \tag{5.11}$$

where the function $D(\overline{x}_{\mathrm{T}})$ is defined as

$$D = 1 + \frac{\eta k_{\mathrm{T}}}{k_{\mathrm{t}} + k_{\mathrm{T}}}\cos\left(\frac{2\pi}{a}\overline{x}_{\mathrm{t}}\right). \tag{5.12}$$

Eq. (5.11) is then rewritten as

$$0 = (-M\omega^2 - i\omega\gamma_{\mathrm{T,eff}} + k_{\mathrm{T,eff}})\tilde{x}_{\mathrm{T}}, \tag{5.13}$$

where the effective spring constant $k_{\mathrm{T,eff}}$ of the bulk tip is defined as

$$k_{\mathrm{T,eff}} = k_{\mathrm{T}} + k_{\mathrm{t}}(1 - \frac{1}{D}) \tag{5.14}$$

and the damping coefficient $\gamma_{\mathrm{T,eff}}$ is defined as

$$\gamma_{\mathrm{T,eff}} = \gamma_{\mathrm{T}} + \frac{\gamma_{\mathrm{T}}}{D^2}. \tag{5.15}$$

Since the resonance frequency $\omega_{\mathrm{T,eff}}$ of the bulk tip is related to the effective spring constant of the contact by $\omega_{\mathrm{T,eff}} = \sqrt{k_{\mathrm{T,eff}}/M}$, the torsional contact resonance can be determined at each tip position $\overline{x}_{\mathrm{t}}$. To combine the calculation of the torsional contact resonance with the lateral friction force, a one-dimensional Prandtl-Tomlinson model [48, 49] at zero temperature is used, which was shown to accurately describe

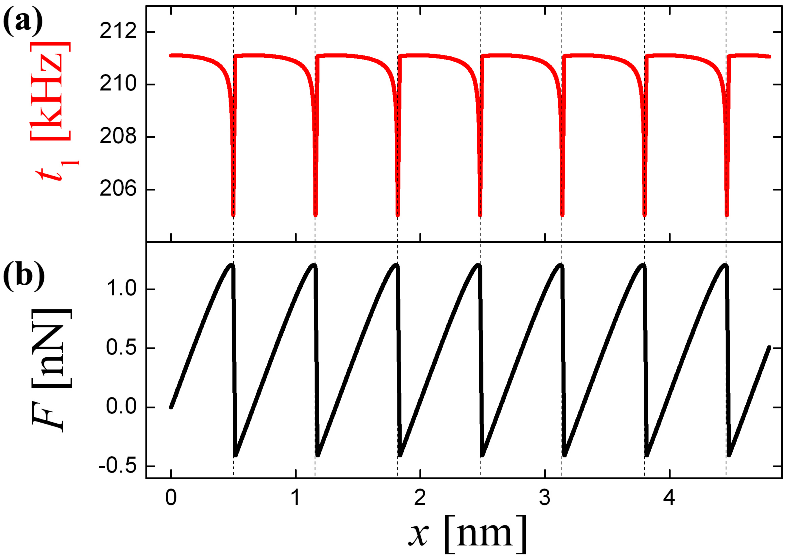

Figure 5.3: Calculated (a) torsional contact resonance using the coupled-spring model and (b) lateral force using the Prandtl-Tomlinson model [32]. The contact resonance is decreasing shortly before the slip event. Points during the fast slip event (> 50 nm/s), where the contact resonance instantly approaches 0 Hz, are not shown to point out the behaviour of the contact resonance before a slip event, which is the main message of the coupled spring calculation.

lateral friction measurements on alkali halides [32]. Hence, the torsional contact resonance t_1 can be calculated in parallel to the friction force F.

5.4 Experiments on Mixed Alkali Halide Crystal

In CR-AFM based on the first flexural mode, active actuation of the cantilever at the contact resonance frequency enhances the amplitude of the oscillation and facilitates tracking the resonace frequency by the PLL. In Section 5.2 the CR-AFM is investigated using the first torsional mode without any mechanical excitation of the system. Even though the torsional actuation reduces the friction as successfully demonstrated in Section 3.3, tracking the broad resonance peak is not more facile for the PLL, as one might expect based on the results of the flexural CR-AFM. Many experiments have been performed on several alkali halides using torsional actuation. In gereral the quality of the tracked torsional contact resonance is not enhanced by the mechanical actuation of the contact. Since the experiments are performed in low friction regime and together with the reduced friction due to the torsional actuation, the torsional CR-AFM in this Section are referred to the ultra low friction regime. Similar to the torsional contact resonance map, the quality of the lateral force map is typically not improved. However a torsional CR-AFM measurement shall be shown in this Section, which is of minor quality compared to the experiment in Section 5.2,

but contains additional information and effects and also exhibits analogies to the flexural contact reasonance experiments in Chapter 4.
In Fig. 5.4 a torsional CR-AFM experiment on a mixed crystal is shown. The anions of the NaCl(90 %)Br(10 %) crystal consist of 90 % chloride and 10 % bromide ions. However, the different anions are not homogenously distributed over the crystal, which may be caused by the crystallisation process and/or the annealing process of the sample preparation which may have an influence on the migration of the bromide ions, i.e. the ratio of chloride to bromide is noticably below 9 : 1. The adhesion force of 0.7 nN is relatively small and indicates that the tip apex is in good condition and the phase is within ±5° showing that the PLL reasonably tracks the contact resonance frequency, except during the slip events where the phase error is increased (see Fig. 5.4(e)). The amplitude is controlled to a fix arbitrary value, and in contrast to the flexural oscillation amplitude, there exists no amplitude calibration for the torsional oscillation in contact mode. The arbitrary amplitude is reasonably controlled apart from the slip events, around which the measured amplitude is decreased because the PLL hardly tracks the correct resonance frequency. Interestingly the excitation is increasing not only at the slip event, where the phase error increases and the measured amplitude decreases, but exhibits a broadened peak. The result that the excitation is increased around the slip event is well reproduced and indicates that more energy is required to maintain the constant amplitude, i.e. the energy mostly dissipates during the slip event. In principle, the result that the energy dissipates mainly during the slip stage in the atomic scale stick-slip process, is known. But this experiment illustrates this phenomenon from the perspective of a damped oscillator sliding on an atomically corrugated surface potential. Even though the energy dissipation is not yet quantitatively analysed, i.e. to determine the energy loss per oscillation cycle, this result support the atomic scale stick-slip investigations from Chapter 3 and gives a direct and new evidence that the energy dissipates mostly in the slip event and not in the sticking phase.
The mixed crystal provides the possibilty to analyse the torsional contact resonance as a function of the different chemical elements, which also differ in size and in principle also in the resonance frequency. The basic requirement is that the tip apex is sufficiently small to be able to differentiate between the chloride and bromide ions. Since the contact diameter is typically in the order of a few atoms of even larger, the contact resonance and lateral force map are consequently influenced by neighboring atoms. However, a general tendency is observed concerning the torsional contact resonance during the sticking phase, during which the resonance frequency is reaching its maximum values. On larger atom sites, which are likely attributed to the bromide ions, the torsional contact resonance is slightly increased compared to the smaller atom sites that are referred to the chloride ions. The deviation in the resonance frequency is relatively small (in the order of ≈ 25 Hz), but the tendency at least is observed. These qualitative results may be supported by further experiments using extremely sharp tips giving a more detailed and quantitative analysis.

5.5 Conclusions

In conclusion, the atomic-scale CR-AFM method is extended to the torsional mode, which was recently shown for the first flexural mode. The PLL was able to track

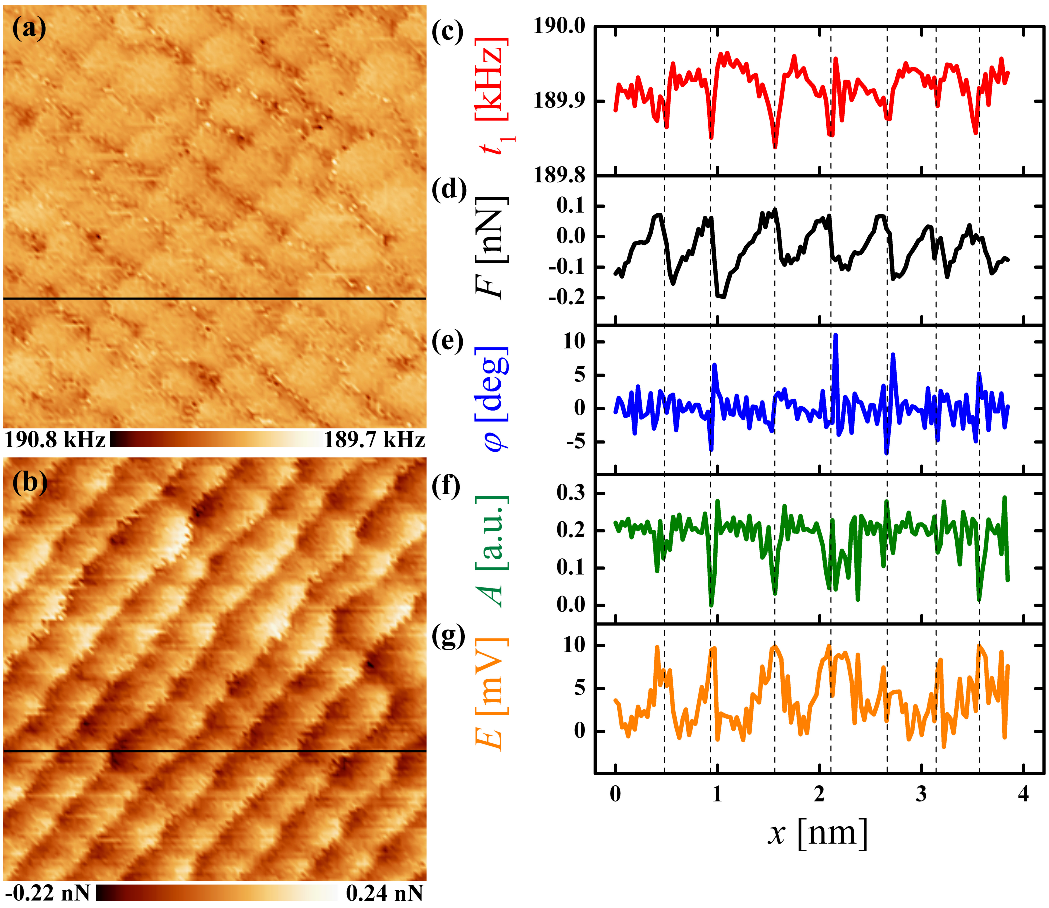

Figure 5.4: Raw data of (a) the torsional contact resonance map and (b) lateral force map measured simultaneously on NaCl(90 %)Br(10 %). (c)-(g) Profiles along the indicated scan line show the contact resonance (red), lateral force (black), phase (blue), amplitude (green) and excitation (orange), which all exhibit patterns consistent with atomic-scale stick-slip motion. The measurement was performed using torsional actuation in constant amplitude mode using a load $= -0.6$ nN (attractive regime). Both, the torsional contact resonance and lateral force maps indicate atoms with different dimensions and the torsional contact resonance is slightly increased on atom sites with bigger dimensions, that are most probably referred to the bromide ions.

the thermally excited torsional contact resonance, i.e. without any mechanical excitation. Experiments using mechanical actuation for the first torsional mode result in minor quality of both, the torsional contact resonance and lateral force signal. The torsional contact frequency reaches maximum values around positions where the tip is perpendicular to the surface. When the tip is tilted the torsional contact frequency is decreasing up to the slip stage, around which it reaches a minimum. The behaviour of this resonance frequency drop before a slip event is explained using a coupled spring model combined with the Prandtl-Tomlinson model, which are in agreement with the experimental data. The fact, that the torsional contact resonance is followed by a slip event may also be used as an indicator to predict a forthcoming slip event, even in situations where stick-slip motion is no longer periodic. In addition, the torsional CR-AFM also appears to be sensitive to atomic-scale defects, whereas the simultaneously detected lateral force barely revealed any feature. The torsional CR-AFM technique is promising to study nanostructures, heterogeneous surfaces and maybe also subsurface structures. The integration of a PLL into conventional FFM makes it possible to upgrade any FFM to CR-AFM, which allows to analyse material properties down to the nanoscale in parallel. The application of torsional CR-AFM to more complex systems than single crystals would be of great benefit to emphasise not only the potential but also the limits of AFM.

> *Ich behaupte aber, dass in jeder besonderen Naturlehre nur so viel eigentlich Wissenschaft angetroffen werden könne, als darin Mathematik anzutreffen ist.*
>
> IMMANUEL KANT

Chapter 6

Angular Dependence of Static and Kinetic Friction

6.1 Introduction

A dependence of friction on the sliding direction (*friction anisotropy*) has been experimentally established even on high symmetry crystal surfaces. In a pioneering study with a scratch apparatus, Bowden and co-workers reported a significantly higher friction along $\langle 100 \rangle$ directions on diamond, MgO, and LiF compared to $\langle 110 \rangle$ directions, which was attributed to enhanced surface damage along the former high-symmetry directions [164]. A similar trend was observed more recently by friction force microscopy (FFM) on the (001) cleavage surface of several alkali halide crystals, and attributed to the enhanced corrugation of the tip-surface interaction potential along $\langle 100 \rangle$ directions [151, 165]. A sinusoidal dependence of friction on the sliding angle was revealed in early investigations on diamond [166]. On the hexagonal cleavage plane of highly oriented pyrolitic graphite (HOPG), a remarkable suppression of friction (often called superlubricity) sometimes observed if the sample was rotated away from directions differing by 60° was attributed to the sliding of a graphite flake attached to the probing tip and incommensurately oriented with respect to the sample [37]. It is important to distinguish such effects which depend on this *misfit angle* from the dependence on the sliding or scan angle φ with respect to a particular high-symmetry axis on the sample surface. Special anisotropy effects reported on less symmetric samples with specific preferred directions are not considered here.

Only a few theoretical simulations, mostly based on the two-dimensional Prandtl-Tomlinson (2D-PT) model [48, 49] or the Frenkel-Kontorova-Tomlinson (2D-FKT) model recently reviewed by Braun [167], have dealt with friction in particular off-symmetry directions [56,68] or with friction anisotropy [66,168]. In the former model the tip is represented by a single particle, whereas in the latter a flake picked up by the tip, or the sliding counterpiece, is represented by a periodic array of particles connected by lateral springs. In both models the particle(s) interact with a 2D sinusoidal potential representing the sample surface, and are connected by separate spring(s) to a support which is scanned at a constant velocity $\mathbf{v}$ parallel to the surface. The PT model is recovered in the absence of the lateral springs or in the limit of hard ones for matching sample and flake lattices (zero misfit). Broad maxima of the average lateral force in the scan direction (*kinetic friction*) around angles corresponding to $\langle 100 \rangle$ directions on (001) cleavage surfaces of rocksalt-type crystals and cusp-like minima along $\langle 110 \rangle$ directions were found in the latter limit for square lattices [66]. For the force required to initiate sliding (*static friction*), however, cusp-like maxima and broad minima were found along the above-mentioned directions in an equivalent 2D-FK model (zero misfit, lateral force directly applied to the support) [169]. For finite misfit angles, friction, both kinetic and static, becomes much lower, as expected from canceling contributions from particles trapped at various positions in different minima of the corrugation potential, especially for misfits approaching incommensurability [66]. A similar behavior of the computed kinetic friction between a rigid flake and a corrugated surface potential, both having the graphene structure, was obtained by Verhoeven *et al.* [168], except that the sharp maxima around zero misfit angles differing by 60° had a angular finite width equal to the flake diameter in units of the lattice constant. For zero misfit they found a dependence of the kinetic friction on scan angle with broad maxima along directions of maximum corrugation and with sharper minima along symmetry directions halfway in between. They could thus interpret the experimental results from the same group on HOPG [37, 73].

These pioneering experiments were conducted with a complex dedicated instrument designed to independently detect force components acting on the tip in three orthogonal directions. In conventional FFM setups, however, only the torsional and flexural deflections of the cantilever with a tip at its end are monitored. Whereas torsion is caused by the lateral force component perpendicular to the cantilever axis, flexure is due to the component perpendicular to the scanned surface, as well as to the bending moment exerted by the lateral component parallel to the cantilever axis [59]. This third component typically dominates the flexural deflection in FFM measurements on atomically flat surfaces for applied normal loads of tens of nanonewtons, and thus distorts the "apparent topography" [170]. Such observations motivated Fujisawa and coworkers [47, 105] to reconstruct the 2D trajectory of the tip apex from lattice-resolved FFM measurements of both deflections.

The goal, however, is to understand the 2D motion of a sharp tip as a function of scan angle at normal forces in the nanonewton range, by focusing on the (001) surface of alkali halide crystals where atomic-scale contacts can be realized [42, 113]. Results can then be quantitatively compared to computations based on the PT model assuming zero misfit, without [42] or with [32, 171] thermal effects included. Because the interpretation of the flexural signal becomes ambiguous at low normal forces, the dependence of friction on scan angle is most reliably studied via the torsional deflection while scanning perpendicular to the cantilever axis and incorporating a

rotatable sample holder in a conventional FFM setup. Having such measurements in mind, for the first time analytical formulas are derived describing the angular dependence of static and kinetic friction in the case of an atomically sharp tip slowly pulled by an elastic spring across a surface lattice with square symmetry whose corrugation is represented by its lowest 2D Fourier component [172].
The predicted dependencies exhibit the above-mentioned features computed using 2D-FKT models for zero misfit [66, 169] and are interpreted in terms of the 2D motion of the tip apex, as revealed by numerical simulations. In particular, the origin of the cusps at the maxima of the static friction and the minima of the kinetic friction is clarified. Moreover, the *offset* between the first scan line and the potential minimum in the unit cell where it is started is shown to cause a spread of possible static friction values, although it has no effect on the kinetic friction. The determination of the corrugation amplitude is also reexamined, which was introduced earlier on the basis of a comparison of lateral force profiles with 1D simulations [42]. The predicted $\langle 100\rangle / \langle 110\rangle$ ratio agrees well with those measured on the (001) surface of alkali halides with similar cation and anion radii [151, 165]. Finally, the present model is proposed to provide a useful benchmark to detect deviations in friction anisotropy due to hitherto neglected higher components of the lateral tip-sample interaction potential.

6.2 Numerical and Analytical Calculations

As in previous simulations of FFM on alkali halide (001) surfaces, which considered scans in high-symmetry directions [107, 108, 112], the motion of the sharp FFM tip is described within the 2D-PT model. The system is represented by a point mass m elastically coupled to a rigid support by a spring of stiffness k. Comparisons between dry friction experiments in ultrahigh vacuum and numerical simulations on alkali halide surfaces have shown that for normal forces in the wearless nanonewton range, the spring constant k is dominated by the lateral stiffness of the contact region rather than by the torsion of the cantilever [42, 113] and is essentially isotropic [32]. Furthermore, the nearly constant and low value of $k \sim 1-2$ N/m indicated that the contact is of atomic size. The elastic potential experienced by the FFM tip is expressed as

$$V_{\text{el}}(x,y;t) = \frac{k}{2}\left[(x-x_0-v_{\text{x}}t)^2 + (y-y_0-v_{\text{y}}t)^2\right], \tag{6.1}$$

where (x, y) are the coordinates of the tip apex, (x_0, y_0) those of the support at time $t = 0$, and $(v_{\text{x}}, v_{\text{y}})$ the components of the scan velocity along the x and y axes. The scan direction is defined by the polar angle $\varphi = \arctan(v_{\text{y}}/v_{\text{x}})$. The total potential experienced by the tip apex,

$$V_{\text{tot}}(x,y;t) = V_{\text{int}}(x,y) + V_{\text{el}}(x,y;t), \tag{6.2}$$

involves in addition the tip-sample interaction potential V_{int} which, for simplicity, is limited to its first 2D Fourier component compatible with square symmetry

$$V_{\text{int}}(x,y) = -\frac{E_0}{2}\left(\cos\frac{2\pi x}{a} + \cos\frac{2\pi y}{a}\right). \tag{6.3}$$

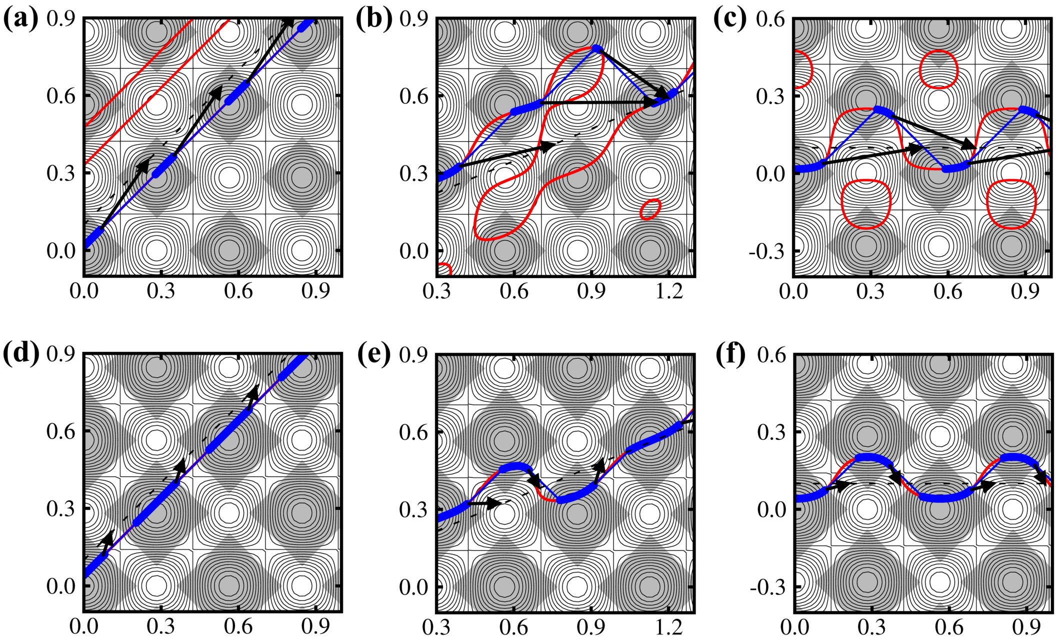

Figure 6.1: 1.0 × 1.0 nm^2 Contour plots of the tip-surface interaction V_{int} on NaCl(001). The dashed lines indicate the scan line (support path), assuming an initial vertical offset of 0.1 nm from the minimum at the origin. The shaded areas denote the stability domains of the tip motion. Inside those areas the computed tip trajectories (thick blue points) essentially coincide with the loci where forces balance in the quasistatic limit (continuous red curve) . Thin blue lines connect the initial and final tip positions in the course of slips between adjacent domains, whereas black arrows point towards the corresponding support positions. Scan lines and trajectories are shown for $\eta = 5$ (a-c) and $\eta = 1.5$ (d-f), for $\varphi = 0°$ (left), which corresponds to the [110] direction, $\varphi = -22.5°$ (center) and $\varphi = -45°$ (right), which corresponds to the [100] direction.

The total potential is then separable, i.e. x and y become decoupled. The quantity E_0 is the load-dependent corrugation of the tip-surface potential. The strength of the interaction energy V_{int} relative to the elastic energy V_{el} stored in the spring is quantified by the parameter $\eta = 2\pi^2 E_0/ka^2$. This parameter was used in previous 1D treatments to define the transition from atomic stick-slip ($\eta > 1$) to a superlubric ($\eta < 1$) regime of motion [42,82]. In view of the lattice periodicity, the *offset* (x_0, y_0) can be chosen to lie within the unit cell in which the first scan line is started. Indeed, in a real FFM experiment the corrugation of V_{int} switches on as the tip first comes into contact with the sample at a preset (x_0, y_0) support position.
Neglecting thermal effects, the tip motion is described by Newton's equation

$$m\frac{d^2\mathbf{r}}{dt^2} + m\Gamma\frac{d\mathbf{r}}{dt} + \nabla V_{\text{tot}} = 0, \tag{6.4}$$

where $\mathbf{r} \equiv (x, y)$ and Γ is the damping rate. Since alkali halides have been extensively studied by FFM [42,113,151,165], the (001) surface of rocksalt is chosen as a model

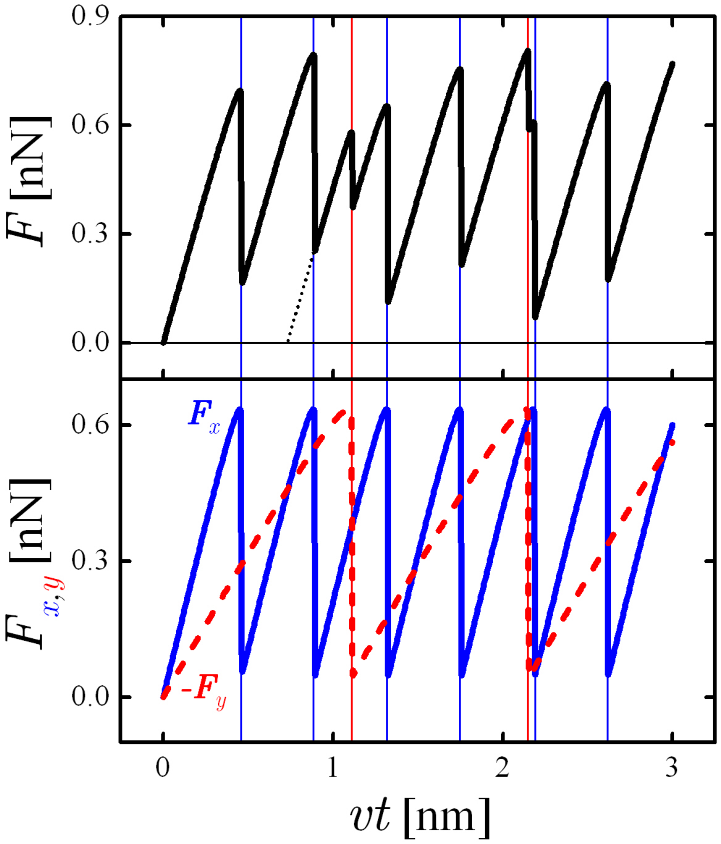

Figure 6.2: Top: Computed dependence of the lateral force exerted by the spring for $\eta = 5$ projected on the scan direction for $\varphi = -22.5°$ starting at $x_0 = y_0 = 0$. Bottom: Corresponding force components versus support displacement (for the chosen direction F_y is negative, so that $-F_\mathrm{y}$ is plotted together with F_x). Because the assumed interaction potential is separable, both components exhibit periodic stick-slip patterns only differing by horizontal stretches proportional to the velocity components $v_\mathrm{x}, v_\mathrm{y}$.

system for testing the predictions. The unit cell of NaCl contains two different ionic species, but only a pattern showing the lattice periodicity is usually imaged in FFM. Note that the [100] and [010] directions are rotated by $\mp 45°$ with respect to the x and y axes and that the usual lattice constant ($a_1 = 0.564$ nm) corresponds $\sqrt{2}a$ in this notation. For comparison with the analytic results valid in the limit of vanishing temperature T and scan velocity, numerical simulations were performed using the velocity Verlet algorithm [65] adapted to include the damping term in Eq. (6.4) using a time step $\Delta t = 10^{-7}$ s and the parameters: $k = 2$ N/m, $v = 25$ nm/s, $\Gamma = 2.8 \times 10^6$ s^{-1}, $m = 10^{-12}$ kg [32]. This choice enables efficient computations on a PC while allowing an adequate sampling of the fast tip motion during slips. Moreover, the damping is close to critical damping, which ensures that all slips occur between adjacent unit cells [32]. Most numerical results illustrated here refer to

$E_0 = 0.5$ eV; the parameter η is then close to 5 , in accordance with FFM measurements with well-developed stick-slip friction without wear on NaCl(001) [42]. A few Langevin simulations were also performed at room temperature in order to complement the previous study of 2D effects [32] which was restricted to scans parallel to [100].

Fig. 6.1 illustrates portions of computed tip trajectories corresponding to three scan directions for $\eta = 5$ (a-c) and $\eta = 1.5$ (d-f) and a given finite initial offset. Starting from the corresponding equilibrium position in the closest-lying minimum of the interaction potential V_{int}, the tip slowly moves along a continuous trajectory until it reaches the boundary of the surrounding stability domain, then suddenly slips into an adjacent minimum. The lateral force $\mathbf{F}_{\text{c}}$ exerted by the spring just before a particular slip is proportional to the corresponding vector depicted as a black arrow in Fig. 6.1. While slipping, the tip avoids the maxima of the potential V_{int}. This leads to a distinct zig-zag trajectory, except along $\langle 110 \rangle$ directions, as shown in Fig. 6.1(a). This zig-zag behavior, which is characteristic of 2D friction, was first inferred by Fujisawa *et al.* from lattice-resolved FFM measurements, most of which were performed along [100] and [010] directions [47,105] on the basal plane of hexagonal crystals (mica, graphite, MoS_2). The simple model which they proposed (tip *stick points* at the centers of adjacent unit cells) appeared to explain their results, but later the same group recognized that the 2D-PT model [112,173]provided a better description of their observations [60]. In the simulations, as a consequence of the separability of $V_{\text{tot}}(x, y; t)$, the tip trajectory is straight in $\langle 110 \rangle$ directions, but coincides with the scan line only if the offset y_0 vanishes. For arbitrary scan directions φ between $\pm 45°$, as shown in Fig. 6.1(b), successive slips along x are interrupted by y slips towards the support path once a certain transverse force is reached. For higher η, y slips merely succeed in maintaining the tip trajectory at a certain average distance from the scan line. This deviation changes sign when the scan direction is reversed. Indeed, between slips during the backward scan, the tip sticks on segments of the quasistatic equilibrium part of the red curve on the other side of the scan line. This causes a hysteresis loop in space, besides the well-known hysteresis in the lateral force, which leads to energy dissipation, i.e. net average friction. Note that the back-bending parts of the red curve lie outside stability domains and are therefore inaccessible. For scans parallel to a symmetry direction, no back bends occur, and backward scan tip trajectories are mirror images of forward ones with respect to the perpendicular symmetry axis. For scans along $\langle 100 \rangle$ directions, as illustrated in Fig. 6.1(c), and noticed by others [47,107,112], each x slip is followed by a y slip of the same magnitude. For smaller values of $\eta > 1$, the overall behavior is similar, but the stability domains are larger, so that the slips become shorter, as illustrated in Figs. 6.1(d-f), and the tip trajectory deviates less from the scan line.

The force measured in conventional FFM is given by the projection of the force $\mathbf{F} = (F_{\text{x}}, F_{\text{y}})$ along the scan direction:

$$F_{\text{scan}} = F_{\text{x}} \cos\varphi + F_{\text{y}} \sin\varphi. \tag{6.5}$$

This quantity is plotted in the top half of Fig. 6.2 for a scan oriented as in Fig. 6.1(b) but with zero initial offset, i.e. starting from a potential minimum. The profile of F_{scan} is aperiodic, but the individual components $F_{\text{x,y}}$ exhibit similar sawtooth patterns with periods $av_{\text{x}}/v, av_{\text{y}}/v$, respectively. Each jump in F_{scan} coincides with a jump in F_x or F_y at the location of the support where an x or y slip occurs. The long-time averages $\langle F_\mathrm{x}\rangle$ and $|\langle F_\mathrm{y}\rangle|$ are therefore equal and the angular dependence of $\langle F_\mathrm{scan}\rangle$ (the *kinetic friction* defined as the average friction force along the scan direction) solely arises from the explicit φ-dependence in Eq. (6.5). The critical value of F_scan corresponding to the position of the *first slip* defines the *static friction* F_stat for a particular initial offset. For the assumed $\eta = 5$, this value is slightly below the first maximum of F_scan but, as shown below, the deviation becomes appreciable if $\eta \to 1$.

For scans between $\langle 110\rangle$ and $\langle 100\rangle$ directions, the values of F_scan at the positions of the following slips define static friction values for different offsets, as can be seen in Fig. 6.1(e). Indeed, points on scan line segments within successively traversed unit cells may be considered as possible offsets for scans started there. However, as seen in Fig. 6.1(b), already for $\eta = 5$ the tip can stick in side minima centered in unit cells which are not traversed by the scan line. According to the physically motivated definition of possible offsets, such metastable locations cannot be considered as commonly realized starting tip positions. A unique offset in each traversed cell can nevertheless be specified as the location where $F_{scan} = 0$. Such locations along the scan line can be found by extrapolating each preceding stick segment down to 0 as approximately indicated by the dotted straight line in Fig. 6.2. For a general scan direction $v_\mathrm{y}/v_\mathrm{x} = \tan\varphi$ is an irrational number, and all possible offset values are therefore sampled along an infinitely long scan line. In the simulations, a sufficiently dense discrete sampling is achieved by scanning over several hundred unit cells. For scan angles approaching $\langle 110\rangle$ or $\langle 100\rangle$ directions, parallel to which the tip trajectories and force variations become periodic, such a dense sampling would require extremely long scans, however.

The preceding discussion implies that $\langle F_\mathrm{scan}\rangle$ *is independent of any initial offset, whereas* F_stat *is not, hence covers a finite range*, except for scans along $\langle 110\rangle$ for which $F_\mathrm{scan} = F_\mathrm{x}$, as illustrated in Fig. 6.3. Together with the analytic expressions derived below these conclusions constitute the two main results of this Chapter.

The curves describing the tip trajectories (Fig. 6.1) and the angle dependence of kinetic and static friction (Fig. 6.3) can be analytically determined. If the scan velocity is sufficiently small (*quasistatic limit*) the tip stays in a slowly evolving local minimum of the potential V_tot during each stick stage, but rapidly slips to an adjacent minimum whenever the local equilibrium becomes marginally stable [48,49]. For the assumed separable potential, the necessary condition for a minimum, $\nabla V_\mathrm{tot} = 0$ as a function of the support displacement $\mathbf{v}t$ leads to decoupled equations for x and y components, namely

$$\begin{aligned} F_\mathrm{x} &= x_0 + v_\mathrm{x}t - x = \eta\sin x \\ F_\mathrm{y} &= y_0 + v_\mathrm{y}t - y = \eta\sin y. \end{aligned} \tag{6.6}$$

In Eq. (6.6) and the following ones reduced units are adopted such that every length must be multiplied by $a/(2\pi)$ and every force by $ka/(2\pi)$. Eliminating t one obtains an analytical expression for the locus of points where the elastic and interaction forces balance, i.e.

$$\frac{y - y_0 + \eta \sin y}{x - x_0 + \eta \sin x} = \frac{v_\mathrm{y}}{v_\mathrm{x}} \equiv \tan \varphi, \tag{6.7}$$

which generalizes to arbitrary offsets the expression used earlier [32]. Those loci are plotted as continuous red curves in Fig. 6.1, whereby only the branch lying near the support path is accessible if the tip dynamics is overdamped or critically damped, as assumed here. The tip equilibrium is stable if the conditions $\lambda_{1,2} > 0$ are satisfied, $\lambda_{1,2}$ being the eigenvalues of the Hessian matrix $\mathcal{H} = \partial^2 V_\mathrm{tot}/\partial x_\mathrm{i} \partial x_\mathrm{j}$, as first emphasized by Gyalog *et al.* [68]. For the separable potential the stability domains form an infinite array of square areas defined by the relations $\cos x > -1/\eta$ and $\cos y > -1/\eta$. These areas surround minima of the potential $V_\mathrm{int}(x, y)$, but merge together and cover the entire *x-y* plane when $\eta \leq 1$. When this *transition to superlubricity* occurs, the above-mentioned locus no longer exhibits back bends and coincides with a unique and reversible tip trajectory which wiggles slightly around the scan line, as suggested by the apparent changes between Figs. 6.1 (a-c) and (d-f). Taking the time derivative of Eq. (6.6), one notices that in the quasistatic approximation the tip velocity is given by

$$\begin{aligned} \dot{x} &= v_\mathrm{x}/(1 + \eta \cos x) \\ \dot{y} &= v_\mathrm{y}/(1 + \eta \cos y) \end{aligned} \tag{6.8}$$

so that its x component appears to diverge when x reaches the stability boundary $x_\mathrm{c} = \arccos(-1/\eta)$, and similarly for y. The quasistatic hypothesis must therefore break down before either boundary is reached. Numerical and analytical computations in the 1D case have shown that at low scan speed $\mathbf{v}$ the tip velocity actually exhibits a peak beyond x_c, which sharpens and moves towards x_c as $v \to 0$ [107,114]. Thus, one can assume that the tip velocity component perpendicular to the stability boundary is much higher than $\mathbf{v}$. As illustrated in Fig. 6.1 by the thin blue lines, the numerical simulations indeed show that the direction of tip motion remains essentially unchanged during slips. If $\eta > 1$ the tip trajectory therefore consists of continuous segments (thick blue points) essentially coinciding with the red curve inside stability domains and of straight segments (thin blue lines) during slips between adjacent domains.

The dependence of the *kinetic friction* on the scan angle follows from the earlier discussion of Fig. 6.2. For symmetry reasons only the range $-45° < \varphi < 45°$ needs to be considered. Due to the absence of cross terms in the equations for F_x and F_y, their long-time average magnitudes are the same and equal to the average in 1D, i.e. $\langle F_\mathrm{x} \rangle = | \langle F_\mathrm{y} \rangle | = g(\eta)$, where the function $g(\eta)$ has previously been computed assuming slips between adjacent stability domains [42]. It can also be approximated by rather accurate asymptotic expansions for small $\eta - 1$ or $1/\eta$ first derived by Helman *et al.* [174]. Thus, the average force acting on the tip apex is always oriented at an angle of $\varphi = 45°$ with respect to the x axis. The kinetic friction measured in FFM is obtained by projecting this force along the scan direction:

$$F_\mathrm{kin} = g(\eta)(\cos \varphi + |\sin \varphi|). \tag{6.9}$$

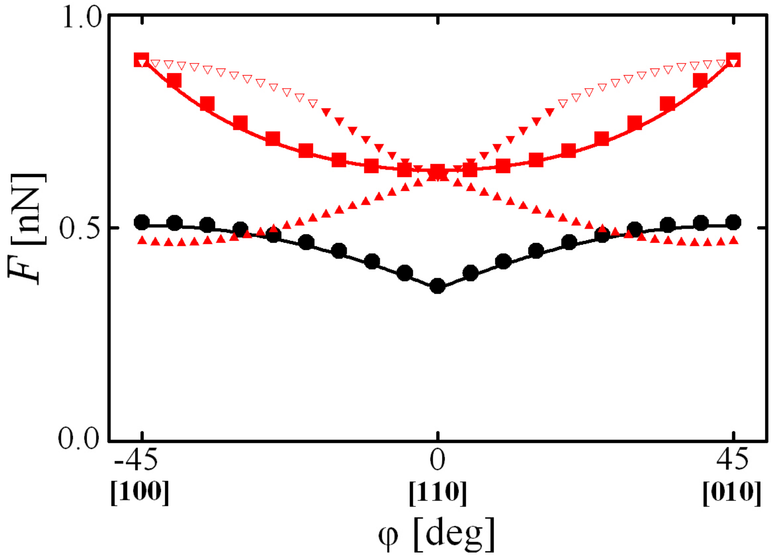

Figure 6.3: Angular dependence of the kinetic friction force $\langle F \rangle$ (black dots) and of the static friction force F_{stat} (red rectangles) for a scan starting at a minimum of the potential V_{int} corresponding to FFM measurements on NaCl(001) for $\eta = 5$. The points obtained from simulations are in good agreement with analytic expression plotted as continuous lines. For finite initial offset, F_{stat} ranges between the red triangles pointing up and down which correspond to calculated minimum and maximum values.

This expression clearly exhibits a cusp at $\varphi = 0$ and, as shown by the continuous black curve in Fig. 6.3, agrees well with points obtained from the simulations. Physically the cusp arises because the tip trajectory suddenly flips to the other side of the support path when φ changes sign.

Next, expressions are derived for the *static friction.* For $-45° < \varphi < 45°$ the first force jump occurs along the x direction when $x = \arccos(-1/\eta)$. Since the first Eq. (6.6) is also satisfied, this jump occurs at the critical time t_{cx} such that $x_0 + v_{\mathrm{x}} t_{\mathrm{cx}} = x_{\mathrm{cs}}(\eta)$,

$$x_{\mathrm{cs}}(\eta) = \sqrt{\eta^2 - 1} + \arccos\left(-1/\eta\right) \tag{6.10}$$

being the x-coordinate of the support when $x = x_{\mathrm{c}}$. The x component of the elastic force acting on the tip is then $F_{\mathrm{cx}} = \sqrt{\eta^2 - 1}$, as in the 1D case [67]. The corresponding y coordinate of the tip satisfies the second Eq. (6.6), which becomes

$$F_{\mathrm{cy}} = \eta \sin y_{\mathrm{c}} = y_0 + v_{\mathrm{y}} t_{\mathrm{cx}} - y_{\mathrm{c}}. \tag{6.11}$$

Substituting the expression for t_{cx} into Eq. (6.11) one obtains a relation which implicitly defines F_{cy} as a function of the scan angle and the initial offset x_0, y_0. A simple expression is obtained in the limit $\eta \gg 1$: then $x_{\mathrm{cs}}(\eta) \simeq \eta$, so that $F_{\mathrm{cy}} \simeq \eta \tan \varphi$, whereas $F_{\mathrm{cx}} \simeq \eta$. In this limit, Eq. (6.5) leads to

$$F_{\mathrm{stat}} = \eta \sqrt{1 + \tan^2 \varphi} = \eta / \cos \varphi, \tag{6.12}$$

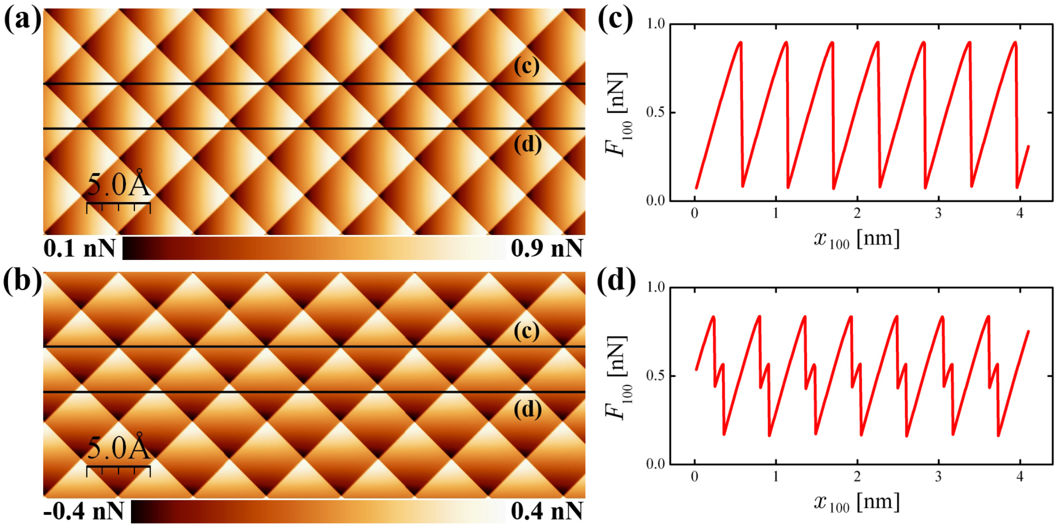

Figure 6.4: Numerically calculated maps for force components (a) parallel and (b) perpendicular to the [100] scan direction when $\eta = 5$. Profiles (c,d) are taken along the scan lines marked (c,d) in map (a) and show that the subsidiary maximum, which appears in general scan lines like (d), disappears for scan lines like (c) which go over corners of the unit cells.

independent of the offset. Although Eq. (6.12) was derived assuming that $\eta \gg 1$, it is in excellent agreement with the values obtained from the simulations performed for $\eta = 5$ if the initial offset is zero. This is shown by the continuous line (red) passing through the squares shown in Fig. 6.3. However, finite offsets lead to a significant spread of realizable F_{stat} values. The maximum and minimum values as a function of φ derived below are indicated by the triangles pointing up and down, respectively. When $\eta \to \infty$ the two limit curves "coalesce" onto the curve described by Eq. (6.12). However, the spread shrinks $\sim 1/\eta$, so that the convergence is quite slow. Eq. (6.12) was stated without proof by Wang et al. [169] and shown to agree with their numerical simulations for a 2D-FK model in the particular case of zero misfit between two identical square arrays. This is not surprising for two reasons: (i) those simulations were performed by directly applying a force to the top array, (ii) before F_{stat} is reached, the lateral springs connecting the particles trapped in adjacent unit cells are not stretched for zero misfit, so that F_{stat} depends only on E_0 and φ.

Analytic expressions for the limiting values $F_{\max}$ and $F_{\min}$ of F_{stat} can be derived by substituting the appropriate values F_{cx} and F_{cy} into Eq. (6.5), which becomes

$$F_{\mathrm{stat}} = \sqrt{\eta^2 - 1}\cos\varphi + \eta \sin y_{\mathrm{c}} \sin\varphi \tag{6.13}$$

where, according to Eq. (6.11), y_{c} satisfies

$$\eta \sin y_{\mathrm{c}} + y_{\mathrm{c}} = y_0 + (x_{\mathrm{cs}} - x_0)\tan\varphi. \tag{6.14}$$

The scan line being specified by

$$y_{\mathrm{s}} = y_0 + (x_{\mathrm{s}} - x_0)\tan\varphi, \tag{6.15}$$

x_0 and y_0 can be replaced by suitable values along the scan line in any traversed unit cell, as stated at the end of the preceding section.

When the support crosses the stability boundary at x_{cs}, the force F_{cy} cannot exceed η. This may occur if $y_{\mathrm{c}} = \pi/2$. Since the right-hand side of Eq. (6.14) increases with y_0 and decreases with x_0, this will happen provided that

$$\tan\varphi > \frac{\eta - \pi/2}{x_{\mathrm{cs}} + \pi}, \tag{6.16}$$

This inequality becomes an equality if in addition $y_0 = -x_0 = \pi$, i.e. if the scan starts at the left corner of a unit cell in Fig. 6.1. This occurs when $\varphi = 19.26°$ for $\eta = 5$, and for $\varphi \to 45°$ if $\eta \to \infty$. If condition (6.16) is satisfied

$$F_{\mathrm{max}} = \sqrt{\eta^2 - 1}\cos\varphi + \eta\sin\varphi, \tag{6.17}$$

which corresponds to the empty triangles pointing down in Fig. 6.3. For smaller angles the maximum value of F_{stat} is reached when $y_0 = -x_0 \to \pi$ and F_{max} is given by Eq. (6.13) together with Eq. (6.14) which becomes

$$\eta\sin y_{\mathrm{c}} + y_{\mathrm{c}} = \pi + (x_{\mathrm{cs}} + \pi)\tan\varphi. \tag{6.18}$$

The corresponding F_{max} values are plotted as full triangles pointing down in Fig. 6.3.

On the other hand, the force F_{cy} cannot be less than $-\eta$. This may occur if $y_{\mathrm{c}} = -\pi/2$. By analogy with the preceding discussion, this will happen provided that

$$\tan\varphi < \frac{-\eta + \pi/2}{x_{\mathrm{cs}} - \pi}. \tag{6.19}$$

If the condition (6.19) is satisfied,

$$F_{\mathrm{min}} = \sqrt{\eta^2 - 1}\cos\varphi - \eta\sin\varphi. \tag{6.20}$$

Otherwise, the minimum value is reached when $x_0 = -y_0 \to \pi$, i.e. if the scan starts at the right corner of a unit cell in Fig. 6.1. F_{min} is then given by Eq. (6.13) together with

$$\eta\sin y_{\mathrm{c}} + y_{\mathrm{c}} = -\pi + (x_{\mathrm{cs}} - \pi)\tan\varphi. \tag{6.21}$$

For $\eta = 5$, condition (6.19) cannot be satisfied, and the F_{min} values corresponding to Eq. (6.21) are plotted as full triangles pointing up in Fig. 6.3.

At first sight it is surprising that F_{max} coincides with the zero offset value of F_{stat} for $\varphi \to \pm 45°$, i.e. for scans along the equivalent $\langle 100\rangle$ and $\langle 010\rangle$ directions. This happens because those directions are singular in several respects. As illustrated in Fig. 6.4, jumps in the lateral force components (a) parallel and (b) orthogonal to the [100] direction generate maps which reflect the underlying surface lattice. Only the parallel component F_{100} is detected in conventional FFM, and the map in Fig. 6.4(a) resembles lattice-resolved maps recorded on flat (001) terraces of alkali halides [42,47,113], apart from streaks near the cell boundaries attributed to instrumental noise and thermally activated stochastic jumps. The profile of F_{100} along scan line (c) which passes right over minima and maxima of V_{int} shown in Fig. 6.4(c) exhibits a simple sawtooth pattern with the period of the standard lattice constant $a_1 = \sqrt{2}a$. The F_{100} peaks of strength $\sqrt{2}\eta$ are close to $F_{\max}$ for $\varphi = \pm 45°$ in Fig. 6.3, as expected for $\eta = 5$, but there is no indication of $F_{\min}$, although the scan line also passes over the left and right corners of the traversed unit cells. However, as first noticed by Hölscher *et al.* on NaF(001) [112], another peak appears in F_{100} [Fig. 6.4(d)] along all scan lines with a finite offset y_{010} precisely where they cross the cell boundaries on the right. This peak disappears as $y_{010} \to 0$, but becomes as high as first peak when $y_{010} = \pi/2$, i.e. halfway between scan lines passing over minima and maxima, thus producing a sawtooth pattern with period $a_1/2$. The evolution of the F_{100} profile is intimately related to subtle changes in zig-zag tip trajectories like that in Fig. 6.1(c). The "stick times" in the cells centered further form the scan line gradually increase until they become equal to those in the other traversed cells for $y_{010} = \pi/2$ [33, 112]. If $0 < y_{010} < -\pi/2$, the zig-zag pattern flips to the other side of the $y_{010} = 0$ scan line, and this discrete change is responsible for the finite slope of F_{stat} as $\varphi \to \pm 45°$ in Fig. 6.3.

At this juncture it is appropriate to re-examine the measurements of Fujisawa *et al.* in the light of subsequent simulations and insights gained in the meantime. Their data on NaF(001), especially those discussed in their review [47], are particularly interesting because they were intentionally recorded using normal forces in the nanonewton range in order to realize an atomic-sized contact. At first sight, it seems gratifying that the magnitude of the observed jumps in the measured deflection signals agrees so well with predictions from their simple "stick-point" model. This is, however, a consequence of the calibration procedure (illustrated in Fig. 4 of their review) and of the essentially linear dependence of the measured F_{scan} in the stick stages. In this case, $k_{\mathrm{exp}} \approx k$ in this notation, so that, e.g., for a zero offset scan along [100], the jump in the deflection signal which accompanies a slip to an adjacent unit cell must be close to the change in the same signal induced by a lateral displacement of the support by one lattice constant. The magnitude of F_{100} is, however, seriously overestimated, if one assumes as Fujisawa *et al.*, that k is determined by the lateral stiffness of the cantilever rather than by that of the contact, which is typically smaller at low normal forces. This became apparent only much later [42].

Additional simulations including thermal fluctuations show that the singularities of zero-offset [100] scans become smeared at RT. Physically this happens because the tip trajectories then consist of noisy stick stages interrupted by x and y slips which occur on *both sides of the scan line* such that the corresponding average proportions gradually change from 1 : 1 to 1 : 0 as the offset is increased along [010].

The [100]-directed zero-offset scans described above are also of particular interest because the corresponding F_{100} profile versus the support displacement $\mathbf{v}t$ exhibits the strongest variation, i.e. the largest signal-to-noise ratio. They have therefore been used to determine the parameters E_0 and k from the measured maximum value $F_{100}^{\max}$ and from the slope k_{exp} of the stick segments [42]. However, this identification assumed that the 1D-PT model can be applied to analyze such scans [42]. The connection between the 1D and 2D-PT models can be made explicit by expressing the interaction potential in terms of the coordinates $x_1 = (x+y)/\sqrt{2}$ and $y_1 = (x-y)/\sqrt{2}$ along the [100] and [010] principal symmetry axes. Recalling that

$a_1 = a\sqrt{2}$, one finds

$$V_{\text{int}} = -E_0 \cos\left(\frac{2\pi x_1}{a_1}\right) \cos\left(\frac{2\pi y_1}{a_1}\right). \tag{6.22}$$

In previous publications which addressed different aspects of the 2D model [32, 33], the factor in front of Eq. (6.22) was instead defined as $E_0/2$. In order to avoid confusion this former E_0 is henceforth denoted as $E_{0,\text{old}}$. For the scans in question $y_1 = 0$, so that

$$V_{\text{int}} = -\frac{E_{0,\text{old}}}{2} \cos\left(\frac{2\pi x_1}{a_1}\right), \tag{6.23}$$

just as in the 1D model.
Note that because $E_{0,\text{old}}/a_1^2 = E_0/a^2$, the parameter η *is the same in both models.* Switching back to real units, in the 1D model [42]

$$F_{100}^{\max} = \pi E_{0,\text{old}}/a_1 = \left(\frac{ka_1}{2\pi}\right)\eta, \tag{6.24}$$

$$k_{\exp} = \frac{k\eta}{1+\eta}. \tag{6.25}$$

In the 2D model, Eqs. (6.5) and (6.6) imply that for the $\varphi = -45°$ zero offset scan $y = -x$, and

$$F_{100} = \frac{F_{\text{x}} - F_{\text{y}}}{\sqrt{2}} = \frac{k}{\sqrt{2}}\frac{\eta}{1+\eta} 2v_{\text{x}}t = \frac{\eta}{1+\eta} kvt \tag{6.26}$$

for small vt, so that Eq. (6.25) is satisfied. Moreover, the maximum value of F_{100} is reached when $x = a/4$; therefore

$$F_{100}^{\max} = \sqrt{2}\left(\frac{ka}{2\pi}\right)\eta, \tag{6.27}$$

which agrees with Eq. (6.24).
The 1D analysis of [100]-directed zero offset scans is therefore justified, at least if E_0 is sufficiently large compared to $k_{\text{B}}T$.
The temperature-dependent reduction in $\langle F_{100}\rangle$ was computed earlier for $E_{0,\text{old}} = 1$, 2 and 4 eV [32] and found to fit well the $(T\ln(T/v))^{2/3}$ dependence predicted by the rate theory of ramped creep [63], except near the superlubric transition. Thus, at RT, $F_{100}^{\max}$ is reduced by factors of 0.50 , 0.68 and 0.81 for $E_0 = 0.5$, 1 and 2 eV, respectively. For the smallest of those values, which corresponds to $\eta = 5$, the computed dependence of $\langle F_{100}\rangle$ during stick stages is essentially linear, as shown in Fig. 6.4(c), so that

$$F_{100}^{\max} \approx \langle F_{100}\rangle + k_{\exp} a_1/2 \tag{6.28}$$

is essentially subject to the same temperature-dependent reduction as $\langle F_{100}\rangle$. The previously mentioned FFM measurements on NaCl(001) extended up to a *nominal* $E_{0,\text{old}}$ slightly above 0.5 eV (obtained from $F_{100}^{\max}$ by applying Eq. (6.24) which is valid for $T \to 0$). In view of the 50 % room temperature reduction in $\langle F_{100}\rangle$,

the *true* $T \to 0$ values of $E_{0,\mathrm{old}}$ and η should be 1.0 eV and 7.9 ± 1.2 (assuming $k \approx 1.3 \pm 0.2$ N/m, according to Fig. 6.3(d) of Ref. [[42]]).
If $\eta \leq \pi$, deviations from Eq. (6.28) become significant even for $T \to 0$. Moreover, according to extensive 1D simulations [117, 118], the temperature-dependent reduction in $\langle F_{100} \rangle$ is stronger in a significantly wider range of $E_0/(k_\mathrm{B}T)$ than predicted by the single-spring model adopted here and in Ref. [[32]]. This extended "thermolubricity" arises in two-spring PT models in which the lateral stiffness and dynamics of the cantilever and tip apex are treated separately. In the range in question, the motion of the cantilever is averaged over rapid thermally activated jumps of the tip apex between two accessible wells of V_tot which become equivalent when $x_\mathrm{s} = a_1/4$. The intervening energy barrier is then

$$\Delta E \approx \frac{3}{2} E_0 \frac{(\eta - 1)^2}{\eta^2} \tag{6.29}$$

to lowest order in an expansion about that support position [118], and thus also depends on E_0 via η and gradually increases above the superlubricity threshold. When the contact stiffness is much smaller than the cantilever stiffness, a rather abrupt crossover is predicted between the "thermolubricity" range and the range where the single-spring model and Eq. (6.28) case become valid [117]. In particular, a further analysis of the room temperature NaCl(001) data [42] showed that "thermolubricity" extends up to $F_{100}^{\max} \approx 0.25$ nN [171], i.e. about midway inside the range covered by the data. Above this value, the *true* E_0 and η can be reliably estimated using the computationally much less expensive one-spring model.
In that range, compared to 1D simulations [63], 2D simulations revealed [32] an additional, nearly constant reduction in $\langle F_{100} \rangle$ by only a factor of 0.9 . This is consistent with the effective 1D character of fluctuations which induce thermally activated slips slightly before the tip reaches the boundary of a stability domain. Indeed, according to multidimensional rate theory [175], such fluctuations preferentially occur along the eigenvector (soft mode) corresponding to the eigenvalue of the Hessian which vanishes at the boundary. The large difference between 1D and 2D simulations claimed in Ref [[107]] arises because the authors defined friction as the average of the magnitude $|\mathbf{F}|$ of the lateral force. The common definition in terms of the projection of $\mathbf{F}$ along the scan direction is however, preferable because this component alone contributes to the work done by the support which is ultimately converted into heat if irreversible slips occur.
The ability of the assumed model potential V_int to describe angle-dependent FFM measurements on (001) surfaces of cubic crystals, in particular alkali halides, can be most straightforwardly tested by comparing the measured ratio $\langle F_{100} \rangle$ / $\langle F_{110} \rangle$ of the kinetic friction along the indicated directions with the prediction of Eq. (6.9), namely $\sqrt{2}$. Using simulations which included thermal effects [32], it was checked that although both $\langle F_{100} \rangle$ and $\langle F_{110} \rangle$ are significantly reduced at RT, their ratio remains close to $\sqrt{2}$. This observation is consistent with the above-mentioned directional character of thermal fluctuations near stability boundaries. Thus, a comparison of the $T \to 0$ prediction with room temperature measurements seems justified, at least in the range where the single-spring model applies.
Namai and Shindo [151] found that the ratio measured on five rocksalt-type crystals increases from about 1.4 for KCl to nearly 2.4 for LiF. They also noticed that

this trend parallels the increase in the ratio r_-/r_+ of the anion and cation radii which changes from 1.35 for KCl to 2.1 for LiF. Their FFM measurements were performed under ambient conditions at a relatively high load of 23 nN, which likely led to a multi-atom contact since the surface lattice could not be imaged. The averages $\langle F_{100}\rangle$ and $\langle F_{110}\rangle$ measured at low relative humidity were, however, constant and thus considered representative. The remarkable agreement between the ratio $\langle F_{100}\rangle / \langle F_{110}\rangle$ predicted by the model potential and the above-mentioned ratio measured on KCl may be fortuitous. Nevertheless the above-mentioned deviation from $\sqrt{2}$ makes physical sense because the curvatures near the saddle points and the minima of $V_{\rm int}$ are expected to increasingly differ for ionic crystals with larger r_-/r_+ ratios. Indeed, in contact measurements on ionic crystals, the modulation of the surface topography at constant normal force, which is simultaneously recorded together with the lateral force $F_{\rm scan}$ in FFM, is mainly determined by the difference between anion and cation radii.

In order to take this difference into account, it is necessary to at least include the next Fourier component of $V_{\rm int}(x,y)$, namely [68],

$$\begin{aligned} -\frac{E_1}{2}\left[\cos\left(\frac{2\pi(x+y)}{a}\right)+\cos\left(\frac{2\pi(x-y)}{a}\right)\right] \\ = -E_1\cos\left(\frac{2\pi x}{a}\right)\cos\left(\frac{2\pi y}{a}\right). \end{aligned} \tag{6.30}$$

When this expression is added to Eq. (6.3), and $E_1/E_0 > 0$, the curvature at the minima is higher than at the maxima, which can therefore be associated with the smaller, recessed cations and the larger, protruding anions, respectively. Because the resulting potential is no longer separable, the stability boundaries become curved [68] and an analytic treatment becomes complicated. Leaving a systematic investigation for the future, note that the present work provides valuable insights into atomic-scale phenomena responsible for the angular dependence of friction forces on a representative class of high-symmetry surfaces, as well as useful benchmark for recognizing deviations from the simple separable 2D-PT model. For instance, E_1 should not only affect the ratio $\langle F_{100}\rangle / \langle F_{110}\rangle$, but also modify the angle and offset dependence of kinetic and static friction. Indeed, a comparison of the tip trajectories in Fig. 6.1(b) with those Fig. 6.1(a) and 6.1(c) shows that for moderate values of η, scans in off-symmetry directions force the tip to explore the profile of $V_{\rm int}(x,y)$ further away from minima and saddle points. Comparison with FFM images measured with the same tip in different directions might thus provide independent estimates of E_1 and, possibly, of higher Fourier components of $V_{\rm int}(x,y)$. The proposed means of characterizing the tip-sample interaction in the contact range is particularly interesting in view of impressive progress in (x,z) or (x,y,z) mapping of the tip-sample interaction in the attractive force range using techniques developed in non-contact atomic force microscopy [176–179].

6.3 Conclusion

The angular dependence of the static and kinetic friction forces acting on a particle pulled by an elastic spring and interacting with a separable model potential with square symmetry is derived and validated by numerical simulations and analytical equations. The simulations provide detailed detailed insights into the atomic-scale origin of the angular dependence. Comparisons with friction force microscopy measurements show that the model is applicable to (001) surfaces of ionic crystals with comparable cation and anion radii. Furthermore, this Chapter provides a useful framework for identifying deviations in the angle dependence which could reveal atomic-scale details of tip-sample interactions in the contact range. Further extensions, including ordered surfaces with different symmetries and more complex unit cells, anisotropic springs, thermal effects and larger contact areas are conceivable. Investigations along those lines would certainly improve the understanding of fundamental friction phenomena on the nanoscale.

Die Wissenschaft fängt eigentlich erst da an interessant zu werden, wo sie aufhört.

Justus von Liebig

Chapter 7

Conclusion and Outlook

7.1 Conclusion

This work on the atomic scale friction using AFM sheds new insight into the field of nano-tribology. The phenomenon of the *stick-slip* has been investigated on the atomic scale for a sharp tip scanning on a flat surface. The ideal instrument to analyse atomic scale stick-slip in this thesis is a home-built FFM, which is operated in UHV and allows very precise and high-quality measurements. The experimental results indicate that the tip apex consists of only a few atoms, allowing nearly atomic resolution in lateral force maps as well as in topography maps. Since the focus is directed to fundamental questions of friction between a single asperity and a flat, the choice of the substrate material is secondary and thus restricted to sample materials which are well known and require a common preparation procedure, such as sodium chloride, potassium bromide, copper and graphite. Compared to more complex surface structures, the mentioned surfaces also comprise the possibility to describe the surface corrugation potential analytically in two dimensions. These corrugation potentials have then been used to study the friction numerically with the Prandtl-Tomlinson model (programmed in C++), which was for the first time extended to two dimensions. This allowed to study not only the stick-slip process as observed in experiments in the lateral force channel, but also to explore the dynamics of the tip apex in a two dimensional fashion. Although the lateral deflection channel in a FFM experiment contains only the torsion of the cantilever, an approach has been accomplished where the horizontal deflection channel is combined with the vertical deflection to reveal the tip trajectory. Merging together the experimental data with the analytical corrugation surface potential indicates that the tip apex preferably resides in minima of the corrugation potential surface, until the pulling force is high enough to overcome the static friction and to induce a slip into an adjacent minima. The dynamics of the tip apex was systematically investigated with numerical simulations using several variable parameters as load, scan direction, strength of actuation and others. The classical Velocity Verlet algorithm was extended to thermal effects, which allowed to approach experimental conditions and analyse the temperature dependence of friction. The calculations have shown that the friction is decreasing at increasing temperature and that the results are in good agreement with literature.

The tip dynamics have been investigated experimentally and numerically for the limit cases, where the average lateral friction force is approaching to zero, i.e. where the friction loop of the forward and backward direction is vanishing. The ultra low friction regime, often referred to *superlubricity*, may be attributed to different physical origins. Experiments on alkali halide and numerical calculations indicated that below a critical threshold of the applied load, the system enters the superlubricity regime (*static superlubricity*), where the normal stick-slip motion goes over into a smooth sliding of the tip on the surface. Another possibility to reduce friction is to mechanically actuate the cantilever in contact at its contact resonance frequency, either the flexural or the torsional contact resonance frequency. Experimental data from literature indicate that the system enters the superlubricity regime (*dynamic superlubricity*) when the flexural actuation reaches a critical threshold. Systematical investigations by means of numerical simulations clarified the origin of the dynamic superlubricity and referred the actuation to a corrugation potential surface that is oscillating and reduces temporarily the energy barriers between adjacent minima. Based on the tip motion, the calculations improved the understanding of the underlying mechanism in dynamic superlubricity. In the case of the torsional mode, it was shown for the first time that torsional actuation of the cantilever reduces friction, and below a critical threshold the system entered again the dynamic superlubricity regime. However, numerical calculations of the friction reduction due to torsional actuation are still missing. The friction reduction due to thermal actuation, i.e. when increasing the temperature, also led to a superlubricity state (*thermolubricity*) if the temperature reaches a critical threshold. Experimentally, the thermolubricity state could never be proved, but was also predicted by numerical calculations. The increased temperature led to thermal jumps of the tip before the system reached the top of the energy barrier, and thus the slip to the adjacent minima was induced earlier compared to low or zero temperature. While the tip apex was pulled by the cantilever over the surface, the tip apex was jumping forward and also backward from potential minima to other minima and thus reduced the kinetic friction force. The detailed numerical calculations improved the understanding of the above-mentioned ultra low friction states, even though only for a very sharp tip scanning on a flat surface.

Analytical formulas have been derived to describe and study the angular dependence of friction on surfaces with square symmetry, and have been validated by numerical simulations. A comparison with FFM experiments from literature showed that the model calculations are applicable to (001) surfaces of ionic crystals with comparable cation and anion radii. The calculations provided a useful framework for identifying deviations in the angular dependence which may reveal atomic scale details of tip-sample interactions in the contact range. The numerical calculation have also been adapted to the hexagonal symmetry of graphite, which demonstrates that the study of angular dependence can be expanded also to more complex surface potentials. A modified version of these numerical simulations for the angular dependence has also been used to investigate the effect of superstructures determined in experiments. Four recent examples of frictional imaging on atomically ordered superstructures were discussed. Two of them, i.e. KBr films on NaCl(001) and graphene on SiC(0001), have been well reproduced by means of the numerical simulations using appropriate combinations of two periodic potentials to describe the tip-surface interaction. The amplitude of the atomic potential was modulated by the superstructure potential in the case of KBr films on NaCl(001), whereas the two potentials were superimposed and rotated in the case of graphene films. The form of the first potential was traced back to the rumpling of the buried KBr/NaCl interfaces, whereas more detailed theoretical investigations should clarify the physical mechanisms responsible for the shape of the graphene superstructure. The experimental and numerical friction maps presented also demonstrated the atomic scale resolution capabilities of FFM.

The friction studies on the atomic scale have been extended by applying a dynamical method, where the first normal and/or the first torsional contact resonance frequency is simultaneously tracked by a phase-locked-loop. This technique is often referred to contact resonance atomic force microscopy (CR-AFM) and exists on large scales, but has now for the first time been applied on the atomic scale. Due to the excellent signal-to-noise ratio of the instrumental setup, small normal excitation amplitudes (in the picometer range) compatible with a linear elastic model of the contact could be used. The variations of the normal contact resonance frequency were compared with the lateral force variations during the atomic stick-slip events. The contact frequency and the deduced normal contact stiffness, which agreed well with the contact stiffness deduced from the slope of the sticking phase, reach maximum values when the contact is not stressed in the lateral direction. A decrease in the normal contact resonance is then followed by a lateral slip of the contact, which may be used as an indicator for predicting a forthcoming slip event even in situations where stick-slip motion is no longer periodic. The contact resonance frequency of the first torsional mode revealed the same behaviour, but with much smaller frequency shifts. The CR-AFM technique also revealed atomic defects, for both the normal and torsional mode, which were not clearly detected in the lateral force or in the vertical deflection. Since a FFM can easily be upgraded to CR-AFM by the integration of only a phase-locked-loop, the combined CR-FFM is a very powerful technique to study friction on the atomic scale together with contact mechanics. The possibility of reducing friction due to mechanical actuation of the contact as described above also allows to perform measurements with reduced plastic deformation, wear or tip change.

To conclude, the work presented within this thesis concerns the modern field of tribology. Many fundamental questions regarding the stick-slip motion and tip dynamics have been studied by means of the combination of FFM experiments and theoretical model calculations. In addition the contact resonance technique has been adapted to the atomic scale for the first time and combined with FFM. This CR-FFM is a potent and precise technique which contains the potential to actively control and measure friction and offers new possibilities in exploring friction on the atomic scale.

7.2 Outlook

The phenomenon of stick-slip has been profoundly investigated on the atomic scale between a tip apex ideally consisting of a few atoms and a flat surface. This model system of a single asperity essentially needs to be extended to a multiple asperity contact, as an intermediate step, to further improve the tribologic behaviour of macroscopic contacts. Thus, the commonly used expression of a bottom-up approach, as often used in physics, biology or nano-sciences, also finds its way into the modern field of tribology. Also the discussion about the energy dissipation is of major importance, and is only marginally studied within this thesis. Many questions arise, i.e. what are the mechanisms causing the energy dissipation and into which form of energy does the dissipated energy transform. This thesis responds to several fundamental questions, but simultaneously poses many new questions, i.e. the issue of energy dissipation in the superlubricity regime or the plastic deformation of the contact region in the sticking and slipping stages.

The effect that the energy dissipation is dependent on the direction was examined for a few materials only. The code of the numerical simulations contains the possibility to be adapted to other surface potentials, and in the new experimental setup, a rotatable sample holder will be integrated which facilitates angular dependence measurements. These studies may then be expanded to more complex materials and surface structures. An interesting area of research are new materials as the molecular crystal compound, which exhibit a different energy dissipation pattern for the forward and backward scan direction. The work about the angular dependence presented in this thesis provides an insight into this field of tribology and at the same time raises new questions and problems.

The contact resonance technique is now adapted to the atomic scale. The simultaneous measurement of the flexural and/or torsional contact resonance frequency with the lateral force leads to the new term Contact Resonance Friction Force Microscopy (CR-FFM). Even though experimental and theoretical results are in good agreement and support an improved understanding, the systematic investigation and application of this technique within this thesis poses various possibilities and many questions. For instance, CR-FFM extended to higher harmonics of the contact resonance frequencies or a combination of different resonance frequencies measured simultaneously, may lead to an advanced sensing of the surface structure or even improve the control of friction. The application of CR-FFM is also promising for more complex surface structures, and includes the capability to identify the chemical composition of the substrate material, which can potentially find its application in material or surface sciences. And the capability of CR-FFM in detecting buried layers or interfaces opens up several possibilities in analysing layered materials, whose properties gains increased attention in industry, for instance in surface coating development or in semiconductor industry.

The control of friction and decrease or avoiding of wear is not only an interesting topic of tribology but also of major importance in many branches in industry. Reducing the wear and abrasion could potentially increase the life time of machines and products, which implies a invaluable economic profit. The work presented in this thesis is limited to a single asperity system on the microscopic scale but represents another step toward an improved understanding of friction reduction and wear. The active reduction of friction as presented on the atomic scale presumably will lead to new difficulties when applying it to macroscopic systems and will also raise many new questions.

Hence, this thesis responds to fundamental questions in tribology on the atomic scale, meliorates the knowledge of contact dynamics in single asperity systems and simultaneously raises many new questions for prospective research.

Eine gute Theorie ist das Praktischste, was es gibt.

Gustav Robert Kirchhoff

Chapter 8

Appendix

The code of the numerical calculations is presented below. The programme is written in C++ using the DevC++ compiler (version 4.9.9.2) and is in principal an extension of the Prandtl-Tomlinson model to two dimensions and the introduction of temperature effects. The integrator of the Langevin equation is a Velocity Verlet algorithm that is extended to temperature effects. Comments are given after // or between /* and */ (blue). For the different sample materials, the surface corrugation potential and its derivatives are changed and also some parameters and output options, whereas the main part of the programme remains identical.

```
/*============================================*/
/*============================================*/
/*============================================*/
//
// Pascal Steiner - 13.09.2010
//
/*============================================*/
/*============================================*/
/*============================================*/
// Libraries:

#include <stdio.h>
#include <cmath>
#include <sys/time.h>

/*============================================*/
/*============================================*/
```

```
/*==========================================*/
// Parameters:

// Number of steps of Ermak algorithm at one support position
#define nstep 1

// Lenght of array "rvec" = 2*nstep
#define length 2

// Side length of the scan area - will be the same length in x- and y-direction
double sidelength;

// Number of points to be written out into the scan file
int resolution;

// Stepsize in y-direction = Sidelength / resolution
double ystep;

// Numerical coefficient in x-direction
double c0a;

// Numerical coefficient in y-direction
double c0b;

// Numerical coefficient in x-direction
double c1a;

// Numerical coefficient in y-direction
double c1b;

// Numerical coefficient in x-direction
double c2a;

// Numerical coefficient in y-direction
double c2b;

// Critical damping constant of the tip in x-direction
double dampca;

// Critical damping constant of the tip in y-direction
double dampcb;

// Damping constant in x-direction in units of the critical damping for calculating numerical coefficient
double dampa;

// Damping constant in y-direction in units of the critical damping for calculat-
```

```
ing numerical coefficient
double dampb;

// Damping rate in x-direction
double gammaa;

// Damping rate in y-direction
double gammab;

// Auxiliary number to calculate noise in x-direction
double aux1a;

// Auxiliary number to calculate noise in y-direction
double aux1b;

// Auxiliary number to calculate noise in x-direction
double aux3a;

// Auxiliary number to calculate noise in y-direction
double aux3b;

// Auxiliary number to calculate noise in x-direction
double aux4a;

// Auxiliary number to calculate noise in y-direction
double aux4b;

// Variance of the position of the noise in x-direction
double corxxa;

// Variance of the position of the noise in y-direction
double corxxb;

// Variance of the velocity of the noise in x-direction
double corvva;

// Variance of the velocity of the noise in x-direction
double corvvb;

// Correlation coefficient*sqrt(corxxa)*sqrt(corvva) in x-direction
double corxva;

// Correlation coefficient*sqrt(corxxa)*sqrt(corvva) in y-direction
double corxvb;

// Corrugation Potential from peak to peak - E0(t) is now a function of time
double E0;
```

```
// Corrugation Potential in [eV], just for printing out into info.dat
double E0eV;

// Condition number that depends on time and modulates E0 - -1 < conod < +1
double cond;

// Normalised amplitude of the corrugated potential caused by the actuation - 0 < alpha < 1
double alpha;

// Normal frequency of the cantilever, that effects the cond
double freq;

// Tip oscillation frequency in x-direction for the calculation of the Conditions 2 and 3
double freq_tipa;

// Tip oscillation frequency in y-direction for the calculation of the Conditions 2 and 3
double freq_tipb;

// Phase of the cos() of the condition number in degree
double phase;

// Phase of the cos() of the condition number in rad
double phaserad;

// Torsional spring constant of the cantilever
double k_clT;

// Spring constant of the Tip in N/m x-direction
double k_tipa;

// Spring constant of the Tip in N/m y-direction
double k_tipb;

// Time step of the simulation
double dt;

// Time
double t;

// Temperature * Boltzmann constant (room temperature simulation)
double temper;
```

```
// Mass of the tip
double m_tip;

// Lattice constant used for the potential (is SQRT(2) smaller than the real lattice constant cc due to the form of the potential)
double aa;

// Real lattice constant [m] - according Ashcroft
double cc;

// Parameter to describe Friction at maximal corrugation potential; if eta > 1, then stick-slip
double eta;

// Scan velocity in x-direction
double veloa;

// Scan velocity in y-direction
double velob;

// Tip velocity in x-direction
double vx;

// Tip velocity in y-direction
double vy;

// Derivative of the potential energy surface in x-direction
double derivpotx = 0.0;

// Derivative of the potential energy surface in y-direction
double derivpoty = 0.0;

// Tip acceleration in x-direction
double ax;

// Tip acceleration in y-direction
double ay;

// Support position in x-direction
double supportx;

// Support position in y-direction
double supporty;

// Start position of support in x-direction
double startx;
```

```
// Start position of support in y-direction
double starty;

// End position of support in x-direction
double endx;

// Tip position in x-direction
double xx;

// Tip position in y-direction
double yy;

// What is the scan direction? 1 = positive x-direction, 0 = negative x-direction
int direction;

// Parameter used for the graphite potential, 0.246 nm is the unit cell parameter
double a1;

// Parameter used for the graphite potential, 0.426 nm is the unit cell parameter
double a2;

// Force acting on tip in x-direction
double forcetot;

// Change in force during scan in x-direction
double forcex;

// Change in force during scan in y-direction
double forcey;

// Noise of position in x-direction
double xnoisea[nstep];

// Noise of velocity in x-direction
double vnoisea[nstep];

// Noise of position in y-direction
double xnoiseb[nstep];

// Noise of velocity in y-direction
double vnoiseb[nstep];

// Counter for printing out data
int ls, ks, is;
```

```
// Counter for function ”scan”
int js;

// Counter
int i, ia;

// Print out data at every #printstep step
double printstep;

// Rounded integer of printstep
int printatstep;

// Definition of idum for function ran2
long idum;

// Definition of seed (initial value for the iteration of ran2)
long seed;

// Declaration of the function ran2
float ran2(long *idum);

// Error Warning Parameter for print out, if conidtions 1 to 3 are not fullfilled
double error1, error2, error3, error4, error5;

// Is the thermal noise on?
char *thermnoise;

// Is the actuation on?
char *actuation;

// Parameter to control the thermal noise: 0 = off and 1 = on
int thermnoisepara;

// Parameter to control the actuation: 0 = off and 1 = on
int actuationpara;

// Potential as a function of x and y, will be written out
double potent;

// Rotation angle in degree, used to determine beta (rad)
double angle;

// Potential for KBr can be rotated around the origin by the angle beta
double beta;

// Used to calculate the potential faster
double fac1, fac2;
```

```
// Used to calculate the force on the rotated potential
double fac3, fac4, fac5, fac6;

// Parameter used to indicate, how far the programme is
double fac7, fac8, fac9, fac10;

// Test variables
double test5,test6,test7;

// Graphite with superstructure
double d1,d2,d3,d4,d5,d6;

// Graphite with superstructure
double d1x,d1y,d2x,d2y;

// Graphite with superstructure
double d3x,d3y,d4x,d4y;

// Graphite with superstructure
double d5x,d5y,d6x,d6y;

// Graphite with superstructure
double double bb,delta,omega;

/*=================================================*/
/*=================================================*/
/*=================================================*/
// Files:

// Parameters of the scan
FILE *info;

// Write out the potential while forward scanning (file to be analysed with WsXm)
FILE *potential;

// Friction force for the forward scan (file to be analysed with WsXm)
FILE *xforce;

// Friction force for the backward scan (file to be analysed with WsXm)
FILE *xforceback;

// File in which any observables can be written out for purpose of control
FILE *control;

// Write out position information of either the tip or the support
FILE *position;
```

```
/*============================================*/
/*============================================*/
/*============================================*/
// Functions:

// Auxiliary parameters for Ermak algorithm
void aux(void);

// Scan function
void scan(void);

// Generates noise for position and velocity in x- and y-direction
void gennoise(void);

/*============================================*/
/*============================================*/
/*============================================*/
// Start of the programme:

int main()
{

/*============================================*/
// Open files:

info = fopen(”info.dat”,”w”);
potential = fopen(”potential.txt”,”w”);
xforce = fopen(”xforce.txt”,”w”);
xforceback = fopen(”xforceback.txt”,”w”);
control = fopen(”control.txt”,”w”);
position = fopen(”position.dat”,”w”);

/*============================================*/
// Writing header of files:

fprintf(xforce,”WSxM file copyright Nanotec Electronica\nWSxM ASCII XYZ file \nX[m]\tY[m]\tZ[N]\n\n”);

fprintf(xforceback,”WSxM file copyright Nanotec Electronica\nWSxM ASCII XYZ file\nX[m]\tY[m]\tZ[N]\n\n”);

fprintf(potential,”WSxM file copyright Nanotec Electronica\nWSxM ASCII XYZ file\nX[m]\tY[m]\tZ[J]\n\n”);

fprintf(control,”WSxM file copyright Nanotec Electronica\nWSxM ASCII XYZ file \nX[m]\tY[m]\tZ[N]\n\n”);
```

```
/*=====================================*/
// Definition and calculation of parameters:

// Parameter to control the thermal noise: 0 = off and 1 = on
thermnoisepara = 1;

// Info: Thermal effects on the cantilever are neglected
// Parameter to control the actuation: 0 = off and 1 = on
actuationpara = 0;

// Side length of the scan area - will be the same length in x- and y-direction
sidelength = 6e-9;

// Number of points to be written out into the scan file (integer!)
resolution = 256;

// Scan velocity in x-direction (support is moved)
veloa = 25.0e-9;

// Time step of the simulation
dt = 1e-7;

// Print out data every ”printstep” steps
printstep = (sidelength / (veloa * dt * resolution));

// Rounded down integer of printstep
printatstep= (int) floor (printstep);

// Step length in y-direction
ystep = sidelength / resolution;

// Spring constant of the tip apex in N/m x-direction (here for graphite)
k_tipa = 4.7;

// Spring constant of the tip apex in N/m y-direction (here for graphite)
k_tipb = 4.7;

// Rotation angle [degree] - used for angle dependence calculations or to reproduce experimental data
angle = 0.0;

// Rotation angle of KBr around the origin [rad]
beta = angle * 2.0 * M_PI / 360.0;

// Rotation angle the superstructure
omega = 30.0 * 2.0 * M_PI / 360.0;
```

```
// Temperature * Boltzmann constant (room temperature simulation)
temper = 298 * 1.38e-23;

// Mass of the tip
m_tip = 1e-12;

// One real lattice constant of graphite (unit cell: 0.246 nm x 0.426 nm)
aa = 0.246e-9;

// Parameter used for the graphite potential, 0.246 nm is the unit cell parameter
a1 = 2.0 * M_PI / 0.246e-9;

// Parameter used for the graphite potential, 0.426 nm is the unit cell parameter
a2 = 2.0 * M_PI / 0.426e-9;

// Alternatively for NaCl: Real lattice constant [m] of NaCl
cc = 0.564e-9;
Alternatively for NaCl: // Lattice constant used for the potential of NaCl, not equal to the real lattice constant aa, due to the form of the potential
aa = cc / sqrt(2.0);

// Periodicity of superstructure on graphite
bb = 1.8e-9;

// Strength of superstructure on graphite
delta = 0.7;

// Friction parameter, determined from experiment
eta = 5;

// Critical damping constant of the tip in x-direction
dampca = 2.0 * sqrt(k_tipa / m_tip);

// Critical damping constant of the tip in y-direction
dampcb = 2.0 * sqrt(k_tipb / m_tip);

// Damping constant in x-direction in units of the critical damping for calculating numerical coefficients
dampa = 10.0 * dampca;

// Damping constant in y-direction in units of the critical damping for calculating numerical coefficients
dampb = 10.0 * dampcb;
```

```
// Damping rate in x-direction
gammaa = dampa / m_tip;

// Damping rate in y-direction
gammab = dampb / m_tip;

// Initial value for the iteration of ran2, determined by system time
seed = time(NULL);

// Enposition of support in x-direction (scan distance in x-direction)
endx = sidelength;

// Initialisation of position in x-direction
supportx = 0.0;

// Initialisation of position in y-direction
supporty = 0.0;

// Start position in x-direction
startx = supportx;

// Start position in y-diretion
starty = supporty;

// Tip position in x-direction
xx = supportx;

// Tip position in y-direction
yy = supporty;

// Initial tip velocity in x-direction
vx = 0.0;

// Initial tip velocity in y-direction
vy = 0.0;

// Initial tip acceleration in x-direction
ax = 0.0;

// Initial tip acceleration in y-direction
ay = 0.0;

// Derivative of the potential energy surface in x-direction
derivpotx = 0.0;

// Derivative of the potential energy surface in y-direction
derivpoty = 0.0;
```

```
// Starting time
t = 0.0;

// Initial force acting on tip in x-direction
forcetot = 0.0;

// Initial change in force during scan in x-direction
forcex = 0.0;

// Initial scan directin is the positive x-direction
direction = 1;

// Initialise noise
for ( ia = 0 ; ia < nstep ; ia ++ )
{
// Initial noise of position in x-direction
xnoisea[ia] = 0.0;
// Initial noise of position in y-direction
xnoiseb[ia] = 0.0;
// Initial noise of velocity in x-direction
vnoisea[ia] = 0.0;
// Initial noise of velocity in y-direction
vnoiseb[ia] = 0.0;
}

// Counter for printing out data in output
ks = 0;

// Counter for printing out data in output
ls = 0;

// Counter for printing out data in output
is = 0;

// Counter for printing out data in output
is = 0;

// Corrugation potential in [J]
E0 = (eta * aa * aa * k_tipa) / (2 * M_PI * M_PI);

// Corrugation potential in [eV]
E0eV = E0 / 1.602176e-19;

// Normalised amplitude of the corrugated potential caused by the actuation: 0
< alpha < 1
alpha = 0.9;
```

```
// Normal frequency of the cantilever, that effects the cond
freq = 2000;

// Phase of cos() of the condition number in [deg] (no influence if actuation is on)
phase = 60.0;

// Phase of cos() of the condition number in [rad] (no influence if actuation is on)
phaserad = phase * 2.0 * M_PI / 360.0;

// Initialisation of the condition number for the modulated potential due to normal actuation of the cantilever
cond = 1.0;

// Tip oscillation frequency in x-direction
freq_tipa =(sqrt(k_tipa / m_tip) / (2.0 * M_PI));

// Tip oscillation frequency in y-direction
freq_tipb =(sqrt(k_tipb / m_tip) / (2.0 * M_PI));

// Initialisation, thermal noise is turned off (do not change!)
thermnoise = ”OFF”;

// Initialisation, actuation is turned off (do not change!)
actuation = ”OFF”;

// Damping constant in x-direction in units of the critical damping for calculating numerical coefficient
fac10 = dampa / dampca;

/*====================================*/
/*====================================*/
/*====================================*/
// Print out warning if the 3 following conditions are not fulfilled:

// Condition 1: The nanotip experiences (”feels”) many times Emin whithin a lattice constant

if ( freq < ( 20.0 * veloa / a1 ) )
{
fprintf(info, ”#### WARNING: The condition 1: freq >> veloa / aa is not fullfilled! #### \n \n”);
error1 = freq / (veloa / aa);
fprintf(info, ”#### WARNING: The condition 1: freq / (veloa / aa) = %f \n \n”, error1);
```

```
}

// Condition 2: An adiabatic approximation, in which inertia and damping of the nanotip are neglected and the forces on the tip are in balance at every instant, leads to this criteria (= adiabatic condition )

if ( freq_tipa < 100.0 * freq )
{
fprintf(info, ”#### WARNING: The condition 2: freq_tipa >> freq is not fullfilled in x-direction! #### \n \n”);
error2 = freq_tipa / freq;
fprintf(info, ”#### WARNING: The condition 2: freq_tipa / freq = %f \n \n”, error2);
}
if ( freq_tipb < 100.0 * freq )
{
fprintf(info, ”#### WARNING: The condition 2: freq_tipb >> freq is not fullfilled in y-direction! #### \n \n”);
error3 = freq_tipb / freq;
fprintf(info, ”#### WARNING: The condition 2: freq_tipb / freq = %f \n \n”, error3);
}

// Condition 3: An adiabatic approximation, in which inertia and damping of the nanotip are neglected and the forces on the tip are in balance at every instant, leads to this criteria ( = adiabatic condition )

if ( ( freq * gammaa ) > ( 1e34 * 4.0 * M_PI * M_PI * freq_tipa * freq_tipa ) )
{
fprintf(info, ”#### WARNING: The condition 3: freq * gammaa << 4 * M_Pi^2 * freq_tipa^2 is not fullfilled for x-direction! #### \n \n”);
error4 = freq * gammaa / 4.0 * M_PI * M_PI * freq_tipa * freq_tipa;
fprintf(info, ”#### WARNING: The condition 3: freq * gammaa / (4 * M_Pi^2 * freq_tipa^2) = %e \n \n”, error4);
}
if ( ( freq * gammaa ) > ( 1e34 * 4.0 * M_PI * M_PI * freq_tipb * freq_tipb ) )
{
fprintf(info, ”#### WARNING: The condition 3: freq * gammaa << 4 * M_Pi^2 * freq_tipb^2 is not fullfilled for y-direction! #### \n \n”);
error5 = freq * gammab / 4.0 * M_PI * M_PI * freq_tipb * freq_tipb;
fprintf(info, ”#### WARNING: The condition 3: freq * gammab / (4 * M_Pi^2 * freq_tipb^2) = %e \n \n”, error5);
}

/*==========================================*/
/*==========================================*/
```

```
/*============================================*/
// Print out parameters into info.dat:

fprintf(info, ”=========> PARAMETERS <========\n \n \n”);
fprintf(info, ”sidelength = %.2e [m]\n \n”, sidelength);
fprintf(info, ”eta = %.2f []\n \n”, eta);
fprintf(info, ”E0 = %.2e [J]\n \n”, E0);
fprintf(info, ”E0eV = %.2f [eV]\n \n”, E0eV);
fprintf(info, ”dt = %.2e [s]\n \n”, dt);
fprintf(info, ”aa = %.2e [m]\n \n”, aa);
fprintf(info, ”bb = %.2e [m]\n \n”, bb);
fprintf(info, ”delta = %.1f []\n \n”, delta);
fprintf(info, ”angle = %.1f [deg]\n \n”, angle);
fprintf(info, ”m_tip = %.2e [kg]\n \n”, m_tip);
fprintf(info, ”alpha = %.2f []\n \n”, alpha);
fprintf(info, ”freq = %.0f [Hz]\n \n”, freq);
fprintf(info, ”k_tipa = %.2f [N/m]\n \n”, k_tipa);
fprintf(info, ”k_tipb = %.2f [N/m]\n \n”, k_tipb);
fprintf(info, ”veloa = %.2e [m/s]\n \n”, veloa);
fprintf(info, ”damp/dampca = %.2f []\n \n”, fac10);
fprintf(info, ”dampca = %.0f [1/s]\n \n”, dampca);
fprintf(info, ”dampcb = %.0f [1/s]\n \n”, dampcb);
fprintf(info, ”dampa = %.0f [1/s]\n \n”, dampa);
fprintf(info, ”dampb = %.0f [1/s]\n \n”, dampb);
fprintf(info, ”seed = %i []\n \n”, seed);
fprintf(info, ”freq_tipa (w) = %.0f [Hz]\n \n”, freq_tipa);
fprintf(info, ”freq_tipb (w) = %.0f [Hz]\n \n”, freq_tipb);
fprintf(info, ”printatstep = %i []\n \n”, printatstep);
fprintf(info, ”ystep = %.2e [m]\n \n”, ystep);
fprintf(info, ”resolution = %i []\n \n”, resolution);

/*============================================*/
/*============================================*/
/*============================================*/
// Parameters for Ermak algorithm are calculated:

aux();

/*============================================*/
/*============================================*/
/*============================================*/
// Initial scan:

//One scan forward is followed by one scan backward to initialise the system
// Counter for printing out data at every #printstep step
ks = 0;
```

```
// Scanning until the sidelength is reached
while ( supportx < endx )
{
// Scanning forward (in positive x-direction)
direction = 1;
scan();
}

// Scanning backward
veloa = - veloa;

// Counter for printing out data at every #printstep step
ks = 0;

// Scanning until the sidelength is reached
while ( supportx > startx )
{
// Scanning backward (in negative x-direction)
direction = 0;
scan();
}

// Velocity is set again to positive to continue scanning in positive x-direction
veloa = - veloa ;

/*==============================================*/
/*==============================================*/
/*==============================================*/
// Begin scanning:

// Scan until the end of the slow scan direction is reached
while ( supporty < sidelength )
{
// Counter for printing out data at every #printstep step
ks = 0;

// Counter for printing out data at every #printstep step
is = 0;

// Scanning until the sidelength is reached
while ( supportx < endx )
{
// Scanning forward (in positive x-direction)
direction = 1;

/*==============================================*/
// Print out forward scan data:
```

```
// Print out data every #printatstep steps
ks+=1;
ls = ks % printatstep;
if ( ls == 1 )
{
// The following fprintf() can be changed to write out any numbers
fprintf(potential, ”%e\t%e\t%e\n”, supportx, supporty, potent);
fprintf(xforce, ”%e\t%e\t%e\n”, supportx, supporty, forcex);
fprintf(control, ”%e%e\t%e\n”, supportx, supporty, vx);
fprintf(position, ”%e\t%e\t%e\t%e\n”, supportx, supporty, xx, yy);
}

// End print out forward scan data
/*==============================================*/

scan()
}


// Inversion of the velocity in x-direction to scan backward
veloa = - veloa ;

/*==============================================*/
// Start with the scan in backward direction:

// Counter for printing out data at every #printstep step
ks = 0;

// Scanning until the sidelength is reached
while ( supportx > startx )
{
// Scanning backward (in negative x-direction)
direction = 0;

/*==============================================*/
// Print out backward scan data:

// Print out data every #printatstep steps
ks+= 1;
ls = ks % printatstep;
if ( ls == 1 )
{
// The following fprintf() can be changed to write out any numbers
fprintf(xforceback, ”%e\t%e\t%e\n”, supportx, supporty, forcex);
}
```

```
// End print out backward scan data
/*=================================================*/

scan();
}

// Velocity is set again to positive to continue scanning in positive x-direction
veloa = - veloa ;

// Move support position one step in y-direction
supporty += ystep;

// Print out to screen, to see the progress of the programme
fac7 = supporty * 1.0e9;
fac8 = sidelength * 1.0e9;
printf(”Scanning Progress: %.2f nm of %.2f nm\n”, fac7, fac8);
}

//End of scan
/*=================================================*/
/*=================================================*/
/*=================================================*/

// Confirm that the programme exits normally
fprintf(info, ”The programme has finished properly.\n\n\n\n”);

// Close Files
fclose (info);
fclose (potential);
fclose (xforce);
fclose (xforceback);
fclose (control);
fclose (position);

// Close Programme
return 0;
}

//End of programme
/*=================================================*/
/*=================================================*/
/*=================================================*/


/*=================================================*/
/*=================================================*/
/*=================================================*/
```

```
// Functions:

void aux(void)
{

c0a = exp(-1.0 * dampa * dt);
c1a = (1 - c0a) / (dampa * dt);
c2a = (1 - c1a) / (dampa * dt);

c0b = exp(-1.0 * dampb * dt);
c1b = (1 - c0b) / (dampb * dt);
c2b = (1 - c1b) / (dampb * dt);

corxxa = dt * dt * temper * (2.0 - ((3.0 - 4.0 * exp(-1.0 * dampa * dt) + exp(-2.0
* dampa * dt)) / (dampa * dt))) / (dampa * dt * m_tip);
corvva = temper * (1.0 - exp(-2.0 * dampa * dt)) / m_tip;
corxva = (dt * temper * (1.0 - exp(-1.0 * dampa * dt)) * (1.0 - exp(-1.0 * dampa *
dt))) / (dampa * dt * m_tip);

corxxb = dt * dt * temper * (2.0 - ((3.0 - 4.0 * exp(-1.0 * dampb * dt) + exp(-2.0
* dampb * dt)) / (dampb * dt))) / (dampb * dt * m_tip);
corvvb = temper * (1.0 - exp(-2.0 * dampb * dt)) / m_tip;
corxvb = (dt * temper * (1.0 - exp(-1.0 * dampb * dt)) * (1.0 - exp(-1.0 * dampb
* dt))) / (dampb * dt * m_tip);

aux1a = sqrt(corxxa);
aux3a = corxva / aux1a;
aux4a = sqrt(corvva - aux3a * aux3a);

aux1b = sqrt(corxxb);
aux3b = corxvb / aux1b;
aux4b = sqrt(corvvb - aux3b * aux3b);

fprintf(info, "=====> COEFFICIENTS <=====\n \n \n");
fprintf(info, "c0a = %f \n", c0a);
fprintf(info, "c1a = %f \n", c1a);
fprintf(info, "c2a = %f \n", c2a);
fprintf(info, "c0b = %f \n", c0b);
fprintf(info, "c1b = %f \n", c1b);
fprintf(info, "c2b = %f \n", c2b);
fprintf(info, "aux1a = %f \n", aux1a);
fprintf(info, "aux3a = %f \n", aux3a);
fprintf(info, "aux4a = %f \n", aux4a);
fprintf(info, "aux1b = %f \n", aux1b);
fprintf(info, "aux3b = %f \n", aux3b);
fprintf(info, "aux4b = %f \n \n \n", aux4b);
}
```

```
/*============================================*/

void scan(void)
{

// If thermal noise is ON, calculate the noise
if ( thermnoisepara == 1 )
{
gennoise();
}

// Move support position in x-direction
supportx += veloa * dt;

for (js = 0 ; js < nstep ; js++)
{
// Actuation is OFF
if ( actuationpara == 0 )
{
cond = 1.0;
}

// Actuation is ON
if ( actuationpara == 1 )
{
cond = ( 1.0 + alpha * cos ( 2.0 * M_PI * freq * t + phaserad ) );
actuation = ”ON”;
}

// Print out, if the Actuation ON or OFF
if ( t == 0 and js == 0 )
{
fprintf(info, ”=======> SYSTEM <=======\n \n \n”);
fprintf(info, ”The ACTUATION is turned %s. \n \n”, actuation);
}

// In the following part the potential, i.e. its derivatives are formulated. Note
that only one of the potentials, either NaCl or graphite may be used. Thus, one of
them has to be excluded when running the programme, and it is possible to change
this part for new potentials.

/*============================================*/
// NaCl (with rotation):

// Calculate Potential
potent = -E0 / 2.0 * cos(2.0 * M_PI / cc * (supportx * cos(beta) - supporty *
```

```
sin(beta))) * cos(2.0 * M_PI / cc * (supportx * sin(beta) + supporty * cos(beta)));

// Calculate Derivativs
d1 = cos(2.0 * M_PI / cc * (xx * cos(beta) - yy * sin(beta)));
d2 = cos(2.0 * M_PI / cc * (xx * sin(beta) + yy * cos(beta)));

d1dx = -2.0 * M_PI / cc * cos(beta) *sin(2.0 * M_PI / cc * (xx * cos(beta) - yy * sin(beta)));
d1dy = 2.0 * M_PI / cc * sin(beta) *sin(2.0 * M_PI / cc * (xx * cos(beta) - yy * sin(beta)));
d2dx = -2.0 * M_PI / cc * sin(beta) *sin(2.0 * M_PI / cc * (xx * sin(beta) + yy * cos(beta)));
d2dy = -2.0 * M_PI / cc * cos(beta) *sin(2.0 * M_PI / cc * (xx * sin(beta) + yy * cos(beta)));

derivpotx = k_tipa * (supportx - xx) + (E0 / 2.0 * cond * (d1dx * d2 + d1 * d2dx));
derivpoty = k_tipb * (supporty - yy) + (E0 / 2.0 * cond * (d1dy * d2 + d1 * d2dy));

/*=======================*/
// Graphite (with rotation of structure (beta) and superstructure (omega)):

// Calculate Potential
potent = -E0 / 4.5 * (2.0 * cos((2.0 * M_PI / aa) * (supportx * cos(beta) - supporty * sin(beta))) * cos((2.0 * M_PI / (aa * sqrt(3))) * (supportx * sin(beta) + supporty * cos(beta))) + cos((4.0 * M_PI / (aa * sqrt(3))) * (supportx * sin(beta) + supporty * cos(beta)))) - E0 / 4.5 * delta * (2.0 * cos((2.0 * M_PI / ) * (supportx * cos(omega) - supporty * sin(omega))) * cos((2.0 * M_PI / (bb * sqrt(3))) * (supportx * sin(omega) + supporty * cos(omega))) + cos((4.0 * M_PI / (bb * sqrt(3))) * (supportx * sin(omega) + supporty * cos(omega))));

// Calculate Derivativs
d1 = 2.0 * cos((2.0 * M_PI / aa) * (xx * cos(beta) - yy * sin(beta)));
d2 = cos((2.0 * M_PI / (aa * sqrt(3))) * (xx * sin(beta) + yy * cos(beta)));
d3 = cos((4.0* M_PI / (aa * sqrt(3))) * (xx * sin(beta) + yy * cos(beta)));
d4 = 2.0 * cos((2.0 * M_PI / bb) * (xx * cos(omega) - yy * sin(omega)));
d5 = cos((2.0 * M_PI / (bb*sqrt(3))) * (xx * sin(omega) + yy * cos(omega)));
d6 = cos((4.0 * M_PI / (bb*sqrt(3))) * (xx * sin(omega) + yy * cos(omega)));

d1x = -2.0 * (2.0 * M_PI / aa) * cos(beta) * sin((2.0 * M_PI / aa) * (xx * cos(beta) - yy * sin(beta)));
d1y = +2.0 * (2.0 * M_PI / aa) * sin(beta) * sin((2.0 * M_PI / aa) * (xx * cos(beta) - yy * sin(beta)));
d2x = -(2.0 * M_PI / (aa*sqrt(3))) * sin(beta) * sin((2.0 * M_PI / (aa*sqrt(3))) * (xx * sin(beta) + yy * cos(beta)));
d2y = -(2.0 * M_PI / (aa*sqrt(3))) * cos(beta) * sin((2.0 * M_PI / (aa*sqrt(3))) * (xx * sin(beta) + yy * cos(beta)));
```

```
d3x = -(4.0 * M_PI / (aa*sqrt(3))) * sin(beta) * sin((4.0 * M_PI / (aa*sqrt(3))) *
(xx * sin(beta) + yy * cos(beta)));
d3y = -(4.0 * M_PI / (aa*sqrt(3))) * cos(beta) * sin((4.0 * M_PI / (aa*sqrt(3))) *
(xx * sin(beta) + yy * cos(beta)));
d4x = -2.0 * (2.0 * M_PI / bb) * cos(omega) * sin((2.0 * M_PI / bb) * (xx *
cos(omega) - yy * sin(omega)));
d4y = +2.0 * (2.0 * M_PI / bb) * sin(omega) * sin((2.0 * M_PI / bb) * (xx *
cos(omega) - yy * sin(omega)));
d5x = -(2.0 * M_PI / (bb*sqrt(3))) * sin(omega) * sin((2.0 * M_PI / (bb*sqrt(3)))
* (xx * sin(omega) + yy * cos(omega)));
d5y = -(2.0 * M_PI / (bb*sqrt(3))) * cos(omega) * sin((2.0 * M_PI / (bb*sqrt(3)))
* (xx * sin(omega) + yy * cos(omega)));
d6x = -(4.0 * M_PI / (bb*sqrt(3))) * sin(omega) * sin((4.0 * M_PI / (bb*sqrt(3)))
* (xx * sin(omega) + yy * cos(omega)));
d6y = -(4.0 * M_PI / (bb*sqrt(3))) * cos(omega) * sin((4.0 * M_PI / (bb*sqrt(3)))
* (xx * sin(omega) + yy * cos(omega)));

derivpotx = k_tipa * (supportx - xx) - (E0 * cond / 4.5 * (d1x * d2 + d1 * d2x +
d3x)) - (E0 * delta / 4.5 * (d4x * d5 + d4 * d5x + d6x));
derivpoty = k_tipa * (supporty - yy) - (E0 * cond / 4.5 * (d1y * d2 + d1 * d2y +
d3y)) - (E0 * delta / 4.5 * (d4y * d5 + d4 * d5y + d6y));

/*=========================================*/
// Integrator of the Langevin Equation:

// Force_tip / Mass_tip = Acceleration_tip in x-direction
ax = derivpotx/m_tip;

// Force_tip / Mass_tip = Acceleration_tip in y-direction
ay = derivpoty/m_tip;

// In the case when thermal noise is ON
if ( thermnoisepara == 1 )
{
thermnoise = ”ON”;

xx += c1a * dt * vx + c2a * dt * dt *ax + xnoisea[js];

yy += c1b * dt * vy + c2b * dt * dt * ay + xnoiseb[js];

vx = c0a * vx + c1a * dt * ax + vnoisea[js];

vy = c0b * vy + c1b * dt * ay + vnoiseb[js];
}

// In the case when thermal noise is OFF
if ( thermnoisepara == 0 )
```

```
{
thermnoise = "OFF";

xx += c1a * dt * vx + c2a * dt * dt * ax;

yy += c1b * dt * vy + c2b * dt * dt * ay;

vx = c0a * vx + c1a * dt * ax;

vy = c0b * vy + c1b * dt * ay;
}

// Is the thermal noise off or on?
if ( t == 0 and js == 0 )
{
fprintf(info, "The THERMAL NOISE is %s. \n \n", thermnoise);
}

// Force acting on the tip in x-direction
forcex = -k_tipa * (supportx - xx);

// Force acting on the tip in y-direction
forcey = -k_tipb * (supporty - yy);

// Total force in scan direction
if ( forcex > 0.0 )
{
// Total friction force
forcetot = -sqrt(forcex * forcex + forcey * forcey);
}

// Total force not in scan direction
if ( forcex < 0.0 )
{
// Total friction force
forcetot = sqrt(forcex * forcex + forcey * forcey);
}

}

// Increase time by timestep dt
t += dt;

}

/*==================================================*/
```

```
void gennoise(void)
{
// Counters
int h,j, hb, jb, hc, hd;

// Array with gaussian distributed random numbers
double gauss[length];
double rvec[length];

// Noise for the x-direction
for (hc=0 ; hc < length ; hc++)
{
rvec[hc] = ran2(&seed);
}

for (h=0 ; h < nstep ; h++ )
{
gauss[2 * h] = sqrt(-2.0 * log(rvec[2 * h])) * cos(2 * M_PI * rvec[2 * h + 1]);
gauss[2 * h + 1] = sqrt(-2.0 * log(rvec[2 * h])) * sin(2 * M_PI * rvec[2 * h + 1]);
}

for (j=0 ; j < nstep ; j++ )
{
xnoisea[j] = aux1a * gauss[2 * j];
vnoisea[j] = aux3a * gauss[2 * j] + aux4a * gauss[2 * j + 1];
}

// Noise for the y-direction
for (hc=0 ; hc < length ; hc++)
{
rvec[hc] = ran2(&seed);
}

for (hb=0 ; hb < nstep ; hb++ )
{
gauss[2 * hb] = sqrt(-2.0 * log(rvec[2 * hb])) * cos(2 * M_PI * rvec[2 * hb + 1]);
gauss[2 * hb + 1] = sqrt(-2.0 * log(rvec[2 * hb])) * sin(2 * M_PI * rvec[2 * hb + 1]);
}

for (jb=0 ; jb < nstep ; jb++ )
{
xnoiseb[jb] = aux1b * gauss[2 * jb];
vnoiseb[jb] = aux3b * gauss[2 * jb] + aux4b * gauss[2 * jb + 1];
}

}
```

```
// The following definitions are used for the random number generator ”ran2”. Source: Numerical Recipes in C: The Art of Scientific Computing, ISBN 0-521-43108-5 by Cambridge University Press (Period: more than 2e18)
#define IM1 2147483563
#define IM2 2147483399
#define AM (1.0/IM1)
#define IMM1 (IM1-1)
#define IA1 40014
#define IA2 40692
#define IQ1 53668
#define IQ2 52774
#define IR1 12211
#define IR2 3791
#define NTAB 32
#define NDIV (1+IMM1/NTAB)
#define EPS 1.2e-7
#define RNMX (1.0-EPS)

float ran2(long *idum)
{
int j;
long k;
static long idum2 = 123456789;
static long iy = 0;
static long iv[NTAB];
float temp;

if (*idum <= 0)
{
if (-(*idum) < 1) *idum = 1;
else *idum = -(*idum);
idum2=(*idum);
for (j = NTAB+7;j> = 0;j–)
{
k = (*idum) / IQ1;
*idum = IA1 * (*idum - k * IQ1) - k * IR1;
if (*idum < 0) *idum += IM1;
if (j < NTAB) iv[j] = *idum;
}
iy = iv[0];
}
k = (*idum) / IQ1;
*idum = IA1 * (*idum - k * IQ1) - k * IR1;
if (*idum < 0) *idum += IM1;
k = idum2 / IQ2;
idum2 = IA2 * (idum2 - k * IQ2) - k * IR2;
if (idum2 < 0) idum2 += IM2;
```

```
j = iy / NDIV;
iy=iv[j]-idum2;
iv[j] = *idum;
if (iy < 1) iy += IMM1;
if ((temp = AM * iy) > RNMX) return RNMX;
else return temp;
}

#undef IM1
#undef IM2
#undef AM
#undef IMM1
#undef IA1
#undef IA2
#undef IQ1
#undef IQ2
#undef IR1
#undef IR2
#undef NTAB
#undef NDIV
#undef EPS
#undef RNMX

//End Functions
/*===============================================*/
/*===============================================*/
/*===============================================*/
```

Acknowledgements

My Ph.D. has been an exciting, very interesting, and challenging experience. By this means, I would like to thank very much all the people who have supported and helped me in any way in achieving my thesis.

First of all, I am very grateful to my Ph.D. mentor Prof. Ernst Meyer for giving me the opportunity to do my Ph.D. thesis in his research group, to participate in several interesting research projects and to attend various international conferences and especially for his great suppport. Also I want to thank him as well as Prof. Enrico Gnecco for accepting to referee my thesis.

A special thank goes to Dr. Enrico Gnecco for his essential and helpful supervision, and his great motivation also in challenging times.

I would like to thank Prof. Alexis Baratoff for his excellent theoretical support, for the interesting discussions and for his big support and advice with his tremendous knowledge, which impressed me over and over again.

I am grateful to Dr. Thilo Glatzel from who I have learned to operate the UHV system and the microscope techniques, and who let me profit from his great competence in experimental physics.

I would like to thank Prof. Christoph Gerber for the useful scientific discussions and the interesting conversations.

It was a pleasure for me to work in Ernst Meyer's group and I would like to thank all the former and current members for all their help and for the friendly and familiar atmosphere, namely to Dr. Sabine Maier, Dr. Enrico Gnecco, Prof. Alexis Baratoff, Dr. Thilo Glatzel, Dr. Bartosz Such, Dr. Anisoara Socoliuc, Dr. Akshata Rao, Raphael Roth, Sascha Koch, Sweetlana Fremy, Dr. Shigeki Kawai, Gregor Fessler, Dr. Marcin Kiesil and Dr. Urs Gysin.

I also would like to thank Germaine Weaver, Astrid Kalt and Barbara Kammermann for the great administration work that they are doing for our group.

Finally, I would like to thank my father and my sister for their continuous support during my studies and my thesis.

For the financial support, I am grateful to acknowledge the Schweizerischer Nationalfonds zur Förderung der wissenschaftlichen Forschung.

Bibliography

[1] G. Schmalz, *Verein Deutscher Ingenieure* , 1461 (1929).

[2] G. Binnig and H. Rohrer, *Helv. Phys. Acta* **55**, 726 (1982).

[3] G. Binnig, H. Rohrer, C. Gerber, and E. Weibel, *Phys. Rev. Lett.* **50**, 120 (1983).

[4] J. Wintterlin, J. Wiechers, H. Brune, T. Gritsch, H. Höfers, and R. J. Behm, *Phys. Rev. Lett.* **62**, 59 (1989).

[5] G. Binnig, C. F. Quate, and C. Gerber, *Phys. Rev. Lett.* **56**, 930 (1986).

[6] G. Binnig, C. Gerber, E. Stoll, T. R. Albrecht, and C. F. Quate, *Surf. Sci.* **189**, 1 (1987).

[7] C. M. Mate, G. M. McClelland, R. Erlandsson, and S. Chiang, *Phys. Rev. Lett.* **59**, 1942 (1987).

[8] G. Meyer and N. M. Amer, *Appl. Phys. Lett.* **56**, 2100 (1990).

[9] Nanosensors$^{\mathrm{TM}}$, *http://www.nanosensors.com.*

[10] T. Trenkler, T. Hantschel, R. Stephenson, P. D. Wolf, W. Vandervorst, L. Hellemans, A. Malave, D. Büchel, E. Oesterschulze, W. Kulisch, P. Niedermann, T. Sulzbach, and O. Ohlsson, *J. Vac. Sci. Technol. B* **18**, 418 (2000).

[11] J. J. Saenz and N. Garcia, *J. Appl. Phys.* **62**, 4293 (1987).

[12] Y. Martin, D. W. Abraham, and H. K. Wickramasinghe, *Appl. Phys. Lett.* **52**, 1103 (1988).

[13] N. Oyabu, O. Custance, I. Yi, Y. Sugawara, and S. Morita, *Phys. Rev. Lett.* **90**, 176102 (2003).

[14] C. M. Mate, M. R. Lorenz, and V. J. Novotry, *J. Chem. Phys.* **90**, 7550 (1989).

[15] Y. Sang, M. Dubé, and M. Grant, *Phys. Rev. E* **77**, 036123 (2008).

[16] D. F. Ogletree, R. W. Carpick, and M. Salmeron, *Rev. Sci. Instr.* **67**, 3298 (1996).

[17] L. Howald, E. Meyer, R. Lüthi, H. Haefke, R. Overney, H. Rudin, and H. J. Gntherodt, *Appl. Phys. Lett.* **63**, 117 (1993).

[18] Omicron GmbH, *http://www.omicron.de.*

[19] B. Such, J. Kolodziej, P. Czuba, P. Piatkowski, P. Struski, F. Krok, and M. Szymonski, *Phys. Rev. Lett.* **85**, 2621 (2000).

[20] J. J. Kolodziej, B. Such, P. Czuba, F. Krok, P. Piatkowski, P. Struski, M. Szymonski, R. Bennewitz, S. Schär, and E. Meyer, *Surf. Sci.* **482-485**, 903 (2001).

[21] R. Bennewitz, S. Schär, V. Barwich, O. Pfeiffer, E. Meyer, F. Krok, B. Such, J. Kolodziej, and M. Szymonski, *Surf. Sci.* **474**, L197 (2001).

[22] G. Meyer and N. M. Amer, *Appl. Phys. Lett.* **53**, 1045 (1988).

[23] SuperlumDiodes Ltd., *http://www.superlumdiodes.com.*

[24] E. R. I. Abraham and E. A. Cornell, *Applied Optics* **37**, 1762 (1998).

[25] M. Nonnenmacher, J. Greschner, O. Wolter, and R. Kassing, *J. Vac. Sci. Technol. B* **9**, 1358 (1991).

[26] E. Meyer, H. J. Hug, and R. Bennewitz, *Scanning Probe Microscopy: The Lab on a Tip*, Springer Verlag, Berlin, Heidelberg, New York, 2004.

[27] D. Sarid, editor, *Scanning Force Microscopy: With Applications to Electric, Magnetic, and Atomic Forces*, Oxford University Press, Oxford, 1994.

[28] E. Meyer, R. M. Overney, K. Dransfeld, and T. Gyalog, *Nanoscience: Friction and Rheology on the Nanometer Scale*, World Scientific Publishing, Singapore, pp. 351, 1998.

[29] U. D. Schwarz, P. Köster, and R. Wiesendanger, *Rev. Sci. Instrum.* **7**, 2560 (1996).

[30] C. Barth, C. Claeys, and C. R. Henry, *Rev. Sci. Instr.* **76**, 083907 (2005).

[31] H. Lüth, editor, *Solid Surfaces, Interfaces and Thin Films*, Springer, Berlin, Heidelberg, New York, 2001.

[32] P. Steiner, R. Roth, E. Gnecco, A. Baratoff, S. Maier, T. Glatzel, and E. Meyer, *Phys. Rev. B* **79**, 045414 (2009).

[33] R. Roth, T. Glatzel, P. Steiner, E. Gnecco, A. Baratoff, and E. Meyer, *Tribol. Lett.* **39**, 6369 (2010).

[34] S. P. Jarvis, A. Oral, T. P. Weihs, and J. B. Pethica, *Rev. Sci. Instrum.* **64**, 3515 (1993).

[35] J. B. Pethica, *Phys. Rev. Lett.* **57**, 3235 (1986).

[36] R. Erlandsson, G. Hadziioannou, C. M. Mate, G. M. McClelland, and S. Chiang, *J. of Chem. Phys.* **89**, 5190 (1988).

[37] M. Dienwiebel, G. S. Verhoeven, N. Pradeep, J. W. M. Frenken, J. A. Heimberg, and H. W. Zandbergen, *Phys. Rev. Lett.* **92**, 126101 (2004).

[38] T. Filleter, W. Paul, and R. Bennewitz, *Phys. Rev. B* **77**, 035430 (2008).

[39] R. Bennewitz, T. Gyalog, M. Guggisberg, M. Bammerlin, E. Meyer, and H. J. Güntherodt, *Phys. Rev. B* **60**, 301 (1999).

[40] J. B. Sokoloff, *Surf. Sci.* **144**, 267 (1984).

[41] M. Hirano, K. Shinjo, R. Kaneko, and Y. Murata, *Phys. Rev. Lett.* **67**, 2642 (1991).

[42] A. Socoliuc, R. Bennewitz, E. Gnecco, and E. Meyer, *Phys. Rev. Lett.* **92**, 134301 (2004).

[43] A. Socoliuc, E. Gnecco, S. Maier, O. Pfeiffer, A. Baratoff, R. Bennewitz, and E. Meyer, *Science* **313**, 207 (2006).

[44] Z. Tshiprut, A. E. Filippov, and M. Urbakh, *Tribol. Int.* **40**, 967 (2007).

[45] E. Gnecco, R. Bennewitz, T. Gyalog, C. Loppacher, M. Bammerlin, E. Meyer, and H. J. Güntherodt, *Phys. Rev. Lett.* **84**, 1172 (2000).

[46] E. Riedo, E. Gnecco, R. Bennewitz, E. Meyer, and H. Brune, *Phys. Rev. Lett.* **91**, 084502 (2003).

[47] S. Morita, S. Fujisawa, and Y. Sugawara, *Surf. Sci. Rep.* **23**, 1 (1996).

[48] L. Prandtl, *Z. Angew. Math. Mech.* **8**, 85 (1928).

[49] G. A. Tomlinson, *Phil. Mag.* **7**, 905 (1929).

[50] I. Szlufarska, M. Chandross, and R. W. Carpick, *J. Phys. D: Appl. Phys.* **41**, 123001 (2008).

[51] G. S. Verhoeven, M. Dienwiebel, and J. W. M. Frenken, *Phys. Rev. B* **70**, 165418 (2004).

[52] A. Filippov, M. Dienwiebel, J. W. M. Frenken, J. Klafter, and M. Urbakh, *Phys. Rev. Lett.* **100**, 046102 (2008).

[53] E. Gnecco, A. Socoliuc, S. Maier, J. Gessler, T. Glatzel, A. Baratoff, and E. Meyer, Nanotechnology **20**, 025501 (2009).

[54] E. Gnecco, A. Socoliuc, and E. Meyer, *Superlubricity*, Elsevier, Amsterdam, 2007.

[55] H. Hölscher, U. Schwarz, and R. Wiesendanger, *Surf. Sci.* **375**, 395 (1997).

[56] H. Hölscher, U. D. Schwarz, O. Zwörner, and R. Wiesendanger, *Z. Phys. B* **104**, 295 (1997).

[57] R. W. Carpick, D. F. Ogletree, and M. Salmeron, *Appl. Phys. Lett.* **70**, 1548 (1997).

[58] S. Krylov, J. Dijksman, W. van Loo, and J. W. Frenken, *Phys. Rev. Lett.* **97**, 166103 (2006).

[59] J. Colchero, E. Meyer, and O. Marti, *Handbook of Micro/Nano Tribology*, CRC Press, Ohio, 1999.

[60] S. Fujisawa, K. Yokoyama, Y. Sugawara, and S. Morita, *Phys. Rev. B* **58**, 4909 (1998).

[61] I. Horcas, R. Fernández, J. M. Gómez-Rodríguez, J. Colchero, J. Gómez-Herrero, and A. M. Baro, *Rev. Sci. Instr.* **78**, 013705 (2007).

[62] P. Langevin, *Comptes rendus hebdomadaires des séances de l' Académie des sciences* **146**, 530 (1908).

[63] Y. Sang, M. Dubé, and M. Grant, *Phys. Rev. Lett.* **87**, 174301 (2001).

[64] P. Reimann and M. Evstigneev, *New J. Phys.* **7**, 25 (2005).

[65] M. P. Allen and D. J. Tildesley, *Computer Simulation of Liquids*, Clarendon, Oxford, 1990.

[66] T. Gyalog and H. Thomas, *Europhys. Lett.* **37**, 195 (1997).

[67] E. Gnecco, R. Bennewitz, T. Gyalog, and E. Meyer, *J. Phys. Condens. Matt.* **13**, 619642 (2001).

[68] T. Gyalog, M. Bammerlin, R. Lüthi, E. Meyer, and H. Thomas, *Europhys. Lett.* **31**, 269 (1995).

[69] C. Fusco and A. Fasolino, *Appl. Phys. Lett.* **84**, 699 (2003).

[70] R. Lüthi, E. Meyer, M. Bammerlin, L. Howald, H. Haefke, T. Lehmann, C. Loppacher, and H. J. Güntherodt, *J. Vac. Sci. Technol. B* **14**, 1280 (1996).

[71] U. Wyder, A. Baratoff, E. Meyer, L. N. Kantorovich, J. David, S. Maier, T. Filleter, and R. Bennewitz, *J. Vac. Sci. Technol. B* **25**, 1547 (2007).

[72] N. Sasaki, K. Kobayashi, and M. Tsukada, *Phys. Rev. B* **54**, 2138 (1996).

[73] M. Dienwiebel, N. Pradeep, G. S. Verhoeven, H. W. Zandbergen, and J. W. M. Frenken, *Surf. Sci.* **576**, 197 (2005).

[74] S. Krylov, K. Jinesh, H. Valk, M. Dienwiebel, and J. W. Frenken, *Phys. Rev. E* **71**, 065101 (2005).

[75] P. Reimann and M. Evstigneev, *New J. Phys.* **7**, 25 (2005).

[76] T. Zykova-Timan, D. Ceresoli, and E. Tosatti, *Nat. Mater.* **6**, 230 (2007).

[77] S. Krylov and J. Frenken, *J. Phys. Condens. Matt.* **20**, 354003 (2008).

[78] S. Medyanik, W. Liu, I. Sung, and R. Carpick, *Phys. Rev. Lett.* **97**, 136106 (2006).

[79] E. Gnecco, R. Bennewitz, and E. Meyer, *Phys. Rev. Lett.* **88**, 215501 (2002).

[80] A. I. Livshits and A. L. Shluger, *Phys. Rev. B* **56**, 12482 (1997).

[81] M. Müser, *Europhys. Lett.* **66**, 97 (2004).

[82] E. Gnecco, S. Maier, and E. Meyer, *J. Phys.: Condens. Matter* **20**, 354004 (2008).

[83] M. Bammerlin, R. Lüthi, E. Meyer, A. Baratoff, J. Lü, M. Guggisberg, C. Loppacher, C. Gerber, and H. J. Güntherodt, *Appl. Phys. A* **66**, 293 (1998).

[84] P. Steiner, R. Roth, E. Gnecco, T. Glatzel, A. Baratoff, and E. Meyer, *Nanotechnology* **20**, 495701 (2009).

[85] A. Socoliuc, E. Gnecco, R. Bennewitz, and E. Meyer, *Phys. Rev. B* **68**, 115416 (2003).

[86] M. Pivetta, F. Patthey, M. Stengel, A. Baldereschi, and W. D. Schneider, *Phys. Rev. B* **72**, 115404 (2005).

[87] J. Repp, G. Meyer, and K. H. Rieder, *Phys. Rev. Lett.* **92**, 036803 (2004).

[88] C. Riedl, U. Starke, J. Bernhardt, M. Franke, and K. Heinz, *Phys. Rev. B* **76**, 245406 (2007).

[89] P. Mallet, F. Varchon, C. Naud, L. Magaud, C. Berger, and J. Y. Veuillen, *Phys. Rev. B* **76**, 041403 (2007).

[90] G. M. Rutter, J. N. Crain, N. P. Guisinger, T. Li, P. N. First, and J. A. Stroscio, *Science* **317**, 219 (2007).

[91] I. Lagadic, R. Clément, O. Kahn, J. Ren, and M. H. Whangbo, *Chem. Mater.* **6**, 1940 (1994).

[92] A. V. Kityk, I. Musevic, G. Slak, and A. F. R. Blinc, *Europhys. Lett.* **36**, 373 (1996).

[93] C. G. Slough, W. W. McNairy, and R. V. Coleman, *Phys. Rev. B* **42**, 9255 (1990).

[94] S. Maier, E. Gnecco, A. Baratoff, R. Bennewitz, and E. Meyer, *Phys. Rev. B* **78**, 045432 (2008).

[95] S. Maier, O. Pfeiffer, T. Glatzel, E. Meyer, T. Filleter, and R. Bennewitz, *Phys. Rev. B* **75**, 195408 (2007).

[96] J. Baker and P. A. Lindgard, *Phys. Rev. B* **60**, 16941 (1999).

[97] T. Filleter, K. V. Emtsev, T. Seyller, and R. Bennewitz, *Appl. Phys. Lett.* **93**, 133117 (2008).

[98] C. Wöll, S. Chiang, R. J. Wilson, and P. H. Lippel, *Phys. Rev. B* **39**, 7988 (1989).

[99] N. N. Gosvami, T. Filleter, P. Egberts, and R. Bennewitz, *Tribol. Lett. (accepted)* (2009).

[100] M. Weiss and F. J. Elmer, *Phys. Rev. B* **53**, 7539 (1996).

[101] K. L. Johnson and J. Woodhouse, *Tribol. Lett.* **5**, 155 (1998).

[102] C. Barth and C. R. Henry, *Phys. Rev. Lett.* **100**, 096101 (2008).

[103] M. Corso, W. Auwrter, M. Muntwiler, A. Tamai, T. Gerber, and J. Osterwalder, *Science* **303**, 217 (2004).

[104] J. Y. Park, D. F. Ogletree, M. Salmeron, R. A. Ribeiro, P. C. Canfeld, C. J. Jenks, and P. A. Thiel, *Science* **309**, 1354 (2005).

[105] S. Fujisawa, Y. Sugawara, S. Ito, S. Mishima, T. Okada, and S. Morita, *Nanotechnology* **4**, 138 (1993).

[106] E. Gnecco and E. Meyer, *Fundamentals of Friction and Wear on the Nanoscale*, Springer Verlag, Berlin, Heidelberg, New York, 2007.

[107] C. Fusco and A. Fasolino, *Phys. Rev. B* **71**, 045413 (2005).

[108] J. Nakamura, S. Wakunami, and A. Natori, *Phys. Rev. B* **72**, 235415 (2005).

[109] Z. Tshiprut, S. Zelner, and M. Urbakh, *Phys. Rev. Lett.* **102**, 136102 (2009).

[110] B. N. J. Persson, *Sliding Friction*, Springer Verlag, Berlin, Heidelberg, New York, 2000.

[111] Y. Mo, K. T. Turner, and I. Szlufarska, *Nature* **457**, 1116 (2009).

[112] H. Hölscher, U. Schwarz, and R. Wiesendanger, *Europhys. Lett.* **36**, 19 (1996).

[113] S. Maier, Y. Sang, T. Filleter, M. Grant, R. Bennewitz, E. Gnecco, and E. Meyer, *Phys. Rev. B* **72**, 245418 (2005).

[114] P. Bilas, L. Romana, F. Bade, K. Delbe, and J. L. Mansot, *Tribol. Lett.* **34**, 41 (2009).

[115] Y. Qi, J. Y. Park, B. L. M. Hendriksen, D. F. Ogletree, and M. Salmeron, *Phys. Rev. B* **77**, 184105 (2008).

[116] M. Reinstädtler, U. Rabe, V. Scherer, U. Hartmann, A. Goldade, B. Bhushan, and W. Arnold, *Appl. Phys. Lett.* **82**, 2604 (2003).

[117] S. Y. Krylov and J. W. M. Frenken, *New J. Phys.* **9**, 398 (2007).

[118] Z. Tshiprut, A. E. Filippov, and M. Urbakh, *J. Phys.: Cond. Mat.* **20**, 354002 (2008).

[119] R. W. Carpick and M. Salmeron, *Chem. Rev.* **97**, 1163 (1997).

[120] B. Bhushan, *Nanotribology and Nanomechanics*, Springer Verlag, Berlin, Heidelberg, New York, 2005.

[121] G. Fessler, I. Zimmermann, P. Steiner, E. Gnecco, T. Glatzel, T. D. Keene, S. Liu, S. Decurtins, and E. Meyer, *submitted to Nano Letters* (2010).

[122] G. Meyer and N. M. Amer, *Appl. Phys. Lett.* **57**, 2089 (1990).

[123] J. A. Ruan and B. Bhushan, *J. Appl. Phys.* **76**, 8117 (1994).

[124] E. Meyer, R. Lüthi, L. Howald, M. Bammerlin, M. Guggisberg, and H. J. Güntherodt, *J. Vac. Sci. Technol. B* **14**, 1285 (1996).

[125] T. Müller, M. Lohrmann, T. Kässer, O. Marti, J. Mlynek, and G. Krausch, *Phys. Rev. Lett.* **79**, 5066 (1997).

[126] H. Hölscher, D. Ebeling, and U. Schwarz, *Phys. Rev. Lett* **101**, 246105 (2008).

[127] R. Lüthi, E. Meyer, H. Haefke, L. Howald, W. Gutmannsbauer, M. Guggisberg, M. Bammerlin, and H. J. Güntherodt, *Surf. Sci.* **338**, 247 (1995).

[128] Z. Tshiprut, A. E. Filippov, and M. Urbakh, *Phys. Rev. Lett.* **95**, 016101 (2005).

[129] D. Tomanek, W. Zhong, and H. Thomas, *Europhys. Lett.* **15**, 887 (1991).

[130] P. Steiner, E. Gnecco, T. Filleter, N. N. Gosvami, S. Maier, E. Meyer, and R. Bennewitz, *Tribol. Lett.* **39**, 321 (2010).

[131] T. R. Albrecht, P. Grütter, D. Horne, and D. Rugar, *J. Appl. Phys.* **69**, 668 (1991).

[132] F. J. Giessibl, *Science* **267**, 68 (1995).

[133] U. Rabe and W. Arnold, *Appl. Phys. Lett.* **64**, 1493 (1994).

[134] K. Yamanaka and H. Ogiso, *Appl. Phys. Lett.* **64**, 178 (1994).

[135] M. Cuberes, H. Assender, G. Briggs, and O. Kolosov, *J. Phys. D: Appl. Phys.* **33**, 2347 (2000).

[136] T. Drobek, R. Stark, and W. Heckl, *Phys. Rev. B* **64**, 045401 (2001).

[137] S. Cantrell, J. Cantrell, and P. Lillehei, *J. of Appl. Phys.* **101**, 114324 (2007).

[138] K. Yamanaka, Y. Maruyama, T. Tsuji, and K. Nakamoto, *Appl. Phys. Lett.* **78**, 1939 (2001).

[139] P. E. Mazeran and J. L. Loubet, *Tribology Letters* **7**, 199 (1999).

[140] E. Dupas, G. Gremaud, A. Kulik, and J. L. Loubet, *Rev. Sci. Instr.* **72**, 3891 (2001).

[141] U. Rabe, M. Kopycinska, S. Hirsekorn, J. M. Saldaña, G. A. Schneider, and W. Arnold, *J. Phys. D: Appl. Phys.* **35**, 2621 (2002).

[142] D. C. Hurley, M. Kopycinska-Müller, A. B. Kos, and R. H. Geiss, *Meas. Sci. Technol.* **16**, 2167 (2005).

[143] D. Passeri, A. Bettucci, M. Germano, M. Rossi, A. Alippi, V. Sessa, A. Fiori, E. Tamburri, and M. L. Terranova, *Appl. Phys. Lett.* **88**, 121910 (2006).

[144] G. Stan and R. Cook, *Nanotechnology* **19**, 235701 (2008).

[145] D. C. Hurley, M. Kopycinska-Müller, and A. B. Kos, *JOM* **59**, 23 (2007).

[146] F. Ohnesorge and G. Binnig, *Science* **260**, 1451 (1993).

[147] U. Rabe, J. Turner, and W. Arnold, *Appl. Phys. A* **66**, 277 (1998).

[148] J. Gao, W. D. Luedtke, and U. Landman, *J. Phys. Chem. B* **102**, 5033 (1998).

[149] B. Luan and M. O. Robbins, *Nature* **435**, 929 (2005).

[150] D. C. Hurley and J. A. Turner, *J. Appl. Phys.* **102**, 033509 (2007).

[151] Y. Namai and H. Shindo, *Jpn. J. Appl. Phys.* **39**, 4497 (2000).

[152] R. Bennewitz, A. S. Foster, L. N. Kantorovich, M. Bammerlin, C. Loppacher, S. Schär, M. Guggisberg, E. Meyer, and A. L. Shluger, *Phys. Rev. B* **62**, 2074 (2000).

[153] U. Rabe, K. Janser, and W. Arnold, *Rev. Sci. Instr.* **67**, 3281 (1996).

[154] U. Rabe, M. Kopycinska, S. Hirsekorn, and W. Arnold, *Ultrasonics* **40**, 49 (2002).

[155] The coefficient B_2 in Ref. [150] needs to be multiplied by a factor 2 .

[156] M. A. Lantz, S. J. O'Shea, A. C. F. Hoole, and M. E. Welland, *Appl. Phys. Lett.* **70**, 970 (1996).

[157] M. Reinstädtler, T. Kasai, U. Rabe, B. Bhushan, and W. Arnold, *J. Phys. D: Appl. Phys.* **38**, 269 (2005).

[158] U. Rabe, *Applied Scanning Probe Methods II*, Springer, Berlin Heidelberg, pp. 37-90, 2006.

[159] U. Rabe, V. Scherer, S. Hirsekorn, and W. Arnold, *J. Vac. Sci. Technol. B* **15**, 1506 (1997).

[160] T. Drobek, R. W. Stark, M. Graber, and W. M. Heckl, *New J. Phys.* **1**, 15.1 (1999).

[161] A. R. Lowry, *Nature* **442**, 802 (2006).

[162] A. Kos and D. Hurley, *Meas. Sci. Technol.* **19**, 015504 (2008).

[163] T. Kawagishi, A. Kato, Y. Hoshi, and H. Kawakatsu, *Ultramicroscopy* **91**, 37 (2002).

[164] F. P. Bowden and C. A. Brookes, *Proc. Roy. Soc. London A* **295**, 244 (1966).

[165] W. Karino and H. Shindo, *Tribology International* **40**, 1568 (2007).

[166] Y. Enomoto and D. Tabor, *Nature* **283**, 51 (1980).

[167] O. M. Braun and A. G. Naumovets, *Surf. Sci. Rep.* **60**, 79 (2006).

[168] G. S. Verhoeven, M. Dienwiebel, and J. W. M. Frenken, *Phys. Rev. B* **70**, 165418 (2004).

[169] C. Wang, W. Duan, X. Hong, and J. Chen, *Appl. Phys. Lett.* **93**, 153116 (2008).

[170] W. L. Wang, S. J. Hu, and R. Clarke, *Phys. Rev. B* **68**, 245401 (2003).

[171] S. Y. Krylov and J. W. M. Frenken, *Phys. Rev. B* **80**, 235435 (2009).

[172] P. Steiner, R. Roth, E. Gnecco, A. Baratoff, and E. Meyer, *Phys. Rev. B* **82**, 205417 (2010).

[173] H. Hölscher, U. D. Schwarz, O. Zwörner, and R. Wiesendanger, *Phys. Rev. B* **57**, 2477 (1998).

[174] J. S. Helman, W. Baltensperger, and J. A. Holyst, *Phys. Rev. B* **49**, 3831 (1994).

[175] G. Vineyard, *J. Phys. Chem. Solids* **3**, 121 (1957).

[176] A. Schirmeisen, D. Weiner, and H. Fuchs, *Phys. Rev. Lett.* **97**, 136101 (2006).

[177] K. Ruschmeier, A. Schirmeisen, and R. Hoffmann, *Phys. Rev. Lett.* **101**, 156102 (2008).

[178] B. J. Albers, T. C. Schwendemann, M. Z. Baykara, N. Pilet, M. Liebmann, E. I. Altman, and U. D. Schwarz, *Nat. Nanotechnology* **4**, 307 (2009).

[179] S. Kawai, T. Glatzel, S. Koch, B. Such, A. Baratoff, and E. Meyer, *Phys. Rev. B* **81**, 085420 (2010).

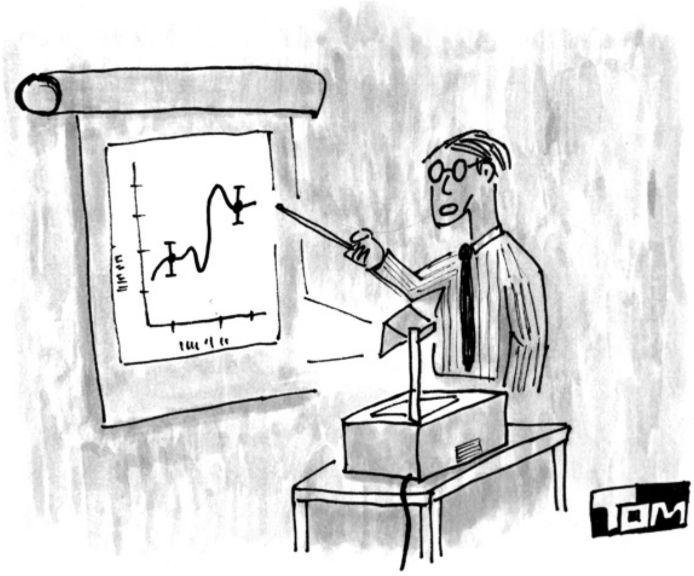

" WE CAN SEE HERE THAT THE AGREEMENT WITH THEORY IS EXCELLENT"

List of Publications

1 Papers

1. **P. Steiner**, R. Roth, E. Gnecco, A. Baratoff, S. Maier, T. Glatzel, and E. Meyer. *Two-dimensional simulation of superlubricity on NaCl and highly oriented pyrolytic graphite.* Physical Review B, Vol. 79 (2009) 045414.
2. **P. Steiner**, R. Roth, E. Gnecco, T. Glatzel, A. Baratoff, and E. Meyer. *Modulation of contact resonance frequency accompanying atomic-scale stick-slip in friction force mircoscopy.* Nanotechnology, Vol. 20 (2009) 495701.
3. R. Roth, T. Glatzel, **P. Steiner**, E. Gnecco, A. Baratoff, and E. Meyer. *Multiple Slips in Atomic-Scale Friction: An Indicator for the Lateral Contact Damping.* Tribology Letters, Vol. 39 (2010) 63-69.
4. **P. Steiner**, R. Roth, E. Gnecco, A. Baratoff, and E. Meyer. *Angular Dependence of Static and Kinetic Friction on Alkali Halide Surfaces.* Physical Review B, Vol. 82 (2010) 205417.
5. **P. Steiner**, E. Gnecco, T. Filleter, N. N. Gosvami, S. Maier, E. Meyer, and R. Bennewitz. *Atomic Friction Investigations on Ordered Superstructures.* Tribology Letters, Vol. 39 (2010) 321-327.
6. **P. Steiner**, E. Gnecco, F. Krok, J. Konior, M. Szymonski, and E. Meyer. *Atomic-scale friction on stepped surfaces of ionic crystals.* Submitted to Physical Review Letters, (2010).
7. G. Fessler, I. Zimmermann, **P. Steiner**, E. Gnecco, T. Glatzel, T. D. Keene, S. Liu, S. Decurtins, and E. Meyer. *Orientation Dependent Molecular Friction on Organic Layer Compound Crystals.* Submitted to Applied Physics Letters, (2010).

2 Talks and Posters

1. **P. Steiner**, S. Maier, E. Gnecco, T. Glatzel, A. Baratoff, and E. Meyer. Oral Presentation: *Dynamic Superlubricity on Insulating and Conductive Surfaces.* Deutsche Physikalische Gesellschaft (DPG) Conference, 26.02.-29.02.2008, Berlin, Germany.

2. **P. Steiner**, S. Maier, E. Gnecco, T. Glatzel, A. Baratoff, and E. Meyer. Poster Presentation: *Dynamic Superlubricity on Insulating and Conductive Surfaces.* Schweizerische Physikalische Gesellschaft (SPS) Conference, 26.03.-27.03.2008, Geneva, Switzerland.

3. **P. Steiner**, S. Maier, E. Gnecco, T. Glatzel, A. Baratoff, and E. Meyer. Poster Presentation: *Dynamic Superlubricity on Insulating and Conductive Surfaces.* National Centres of Competence in Research (NCCR) Workshop, 04.06.-06.06.2008, Davos, Switzerland.

4. **P. Steiner**, R. Roth, E. Gnecco, A. Baratoff, S. Maier, T. Glatzel, and E. Meyer. Poster Presentation: *Two-dimensional Simulation of Superlubricity on NaCl and HOPG.* 428th WE Heraeus Seminar "Physics of Friction", 23.03.-25.03.2009, Bad-Honnef, Germany.

5. F. Krok, M. Goryl, S. R. Saeed, J. Budzioch, M. Szymonski, **P. Steiner**, E. Gnecco, T. Glatzel and E. Meyer. Poster Presentation: *Atomic-scale friction on stepped surfaces of ionic crystals.* Energy Dissipation in Nanocontacts and Molecular Bonds (EDINAM) Conference, 28.09-01.10.2009, Dresden, Germany.

6. **P. Steiner**, R. Roth, E. Gnecco, T. Glatzel, A. Baratoff, and E. Meyer. Oral Presentation: *Contact Resonance Atomic Force Microscopy (CR-AFM) on the Atomic Scale.* International Centre of Theoretical Physics (ICTP) Conference, 19.10.-24.10.2009, Trieste, Italy.

7. G. Fessler, I. Zimmermann, **P. Steiner**,T. Glatzel, E. Gnecco, T. Keene, S. Liu, S. Decurtins, and E. Meyer. Oral Presentation: *Friction Force Microscopy on a Layer Compound with Organic Surface.* Deutsche Physikalische Gesellschaft (DPG) Conference, 21.03-26.03.2010, Regensburg, Germany.

8. G. Fessler, I. Zimmermann, **P. Steiner**,T. Glatzel, E. Gnecco, T. Keene, S. Liu, S. Decurtins, and E. Meyer. Oral Presentation: *Friction Asymmetry on Layer Compound Crystals.* 1st European Nanomanipulation Workshop, 17.05-19.05.2010, Cascais, Portugal.

9. **P. Steiner**, R. Roth, E. Gnecco, A. Baratoff, and E. Meyer. Poster Presentation: *Atomic Scale Contact Resonance Imaging and Friction Anisotropy on Alkali Halides.* National Centres of Competence in Research (NCCR) 9th Site Visit of the Review Panel, 27.04.2010, Basel, Switzerland.

10. A. Baratoff, **P. Steiner**, R. Roth, E. Gnecco, T. Glatzel, and E. Meyer. Poster Presentation: *Novel aspects of atomic-scale friction force microscopy.* Swiss Physical Society Jahrestagung, 21.06.-22.06.2010, Basel, Switzerland.
11. **P. Steiner**, E. Gnecco, A. Baratoff, and E. Meyer. Poster Presentation: *Contact Resonance Atomic Force Microscopy (CR-AFM) as an Imaging Technique on the Nanoscale.* Veeco Conference - Nanoscale VIII, 30.08.-01.09.2010, Basel, Switzerland.
12. **P. Steiner**, F. Krok, E. Gnecco, and E. Meyer. Poster Presentation: *Atomic-Scale Friction on Stepped Surfaces of Ionic Crystals* Friction and Adhesion in Nanomechanical Systems (FANAS) Conference, 25.10.-28.10.2010, Saarbrücken, Germany.
13. E. Gnecco, **P. Steiner**, R. Roth, A. Baratoff, and E. Meyer. Poster Presentation: *Static Friction Anisotropy on Hexagonal, Square and Honeycomb Lattices* Friction and Adhesion in Nanomechanical Systems (FANAS) Conference, 25.10.-28.10.2010, Saarbrücken, Germany.

Curriculum vitæ

Name: Pascal Steiner
Date of Birth: July 25th, 1982
Place of Birth: Bordeaux, France

2007 - 2010	PhD student and teaching assistant in the research group of Prof. E. Meyer, Physics Department, University of Basel
2005 - 2007	Master of Science in Nanosciences, University of Basel Master Thesis: *Rebinding Dynamics in Myoglobin-CO using Reactive Molecular Dynamics and Ab Initio Calculation for the Calculation of the Potential Barrier*
2002 - 2005	Bachelor in Science with Major in Nanosciences, University of Basel
1998 - 2001	Gymnasium in Oberwil (BL)
1994 - 1998	Progymnasium in Therwil (BL)
1990 - 1994	Primary School in Ettingen (BL)
1989 - 1990	Primary School in Riehen (BS)